NOTICE
This report was prepared as an account of work sponsored by the United States Government. Neither the United States nor the United States Department of Energy, nor any of their employees, nor any of their contractors, subcontractors, or their employees, makes any warranty, express or implied, or assumes any legal liability or responsibility for the accuracy, completeness or usefulness of any information, apparatus, product or process disclosed, or represents that its use would not infringe privately owned rights.

TABLE OF CONTENTS

ACKNOWLEDGEMENT..... vii

ABSTRACT..... ix

I. A SURVEY OF METASTABLE RARE GAS INTERACTIONS, AND THE EXPERIMENTAL TECHNIQUES USED IN THEIR INVESTIGATION..... 1

A. Introduction..... 2

B. The Theoretical Picture..... 4

a) Direct E-E Transfer..... 5

b) Chemical Exchange Reactions..... 6

C. Experimental Techniques Used to Investigate Metastable Reactions..... 15

a) Discharge Flow System..... 15

b) Gas Cell Fluorescence..... 16

c) Beam-Gas Experiments..... 16

d) Beam-beam Experiments..... 17

(i) Merging beams..... 17

(ii) Crossed beams..... 18

REFERENCES - CHAPTER I..... 24

TABLES..... 27

FIGURE CAPTIONS..... 30

FIGURES..... 31

II. THE THEORETICAL BASIS FOR OPTICAL POTENTIAL ANALYSIS AND ITS COMPUTATIONAL IMPLEMENTATION..... 38

A. Theoretical and Computational Aspects of Chemi-Ionization 38

B. The Optical Potential and the Resultant Phase Shifts.... 40

C. Cross Section and Phase Shifts..... 53

DISTRIBUTION OF THIS DOCUMENT IS UNLIMITED

D. Actual Procedure of Data Analysis..... 63

E. The Ionic Potential from V and VI..... 65

REFERENCES - CHAPTER II..... 75

APPENDIX

Differential Cross Section Program for Complex Potentials, INELAS. 76

Sample Output from Program INELAS. 106

III. THE INTERACTION OF $He(2^3S)$ + Ar..... 113

A. Introduction..... 113

B. Data Analysis..... 120

C. The Total Ionization Cross Section..... 126

D. Total Elastic Cross Section..... 126

E. The Ionic Potential..... 127

F. Opacities..... 128

G. Sources of Uncertainty..... 129

H. Validity of Semiclassical Approach..... 131

I. Conclusion..... 133

REFERENCES - CHAPTER III..... 134

TABLE..... 136

FIGURE CAPTIONS..... 137

FIGURES..... 139

IV. THE INTERACTIONS OF $He(2^1S)$ + D_2, AND $He(2^3S)$ + D_2..... 153

A. Introduction..... 153

B. Results and Discussion for $He(2^3S)$ + D_2..... 166

C. $He(2^1S)$ + D_2, A Comparison Study..... 168

D. Rate Constants..... 170

E. Branching Ratios of Ionic Products..... 171

F. The Total Ionization and Elastic Cross Section..... 172

G. Opacities and Classical Turning Points..... 173

H. Conclusion..... 174

REFERENCES - CHAPTER IV..... 177

TABLES..... 179

FIGURE CAPTIONS..... 182

FIGURES..... 184

V. THE CONSTRUCTION AND PERFORMANCE CHARACTERISTICS OF A NITROGEN-LASER-PUMPED-DYE LASER SYSTEM..... 202

A. Dye Laser Physics..... 202

B. The Dye Molecule as Laser Medium..... 205

C. The Nitrogen Laser..... 208

D. The Physics of Electrical Discharges as Applied to the Excitation of N_2..... 209

E. E/p and Overvolting..... 212

F. Discharge Uniformity..... 219

G. Details of Construction of a Nitrogen Laser..... 221

a) The Discharge Circuit..... 221

b) The Discharge Tube..... 225

c) The Gas Flow..... 227

d) The Spark Gap..... 227

e) The Power Supply..... 228

f) Energy Storage Capacitor..... 229

g) Performance Characteristics..... 231

H. The Dye Laser Module..... 232

I. A Flashlamp-pumped Dye Laser..... 232

REFERENCES - CHAPTER V..... 235

FIGURE CAPTIONS..... 236

FIGURES..... 237

ACKNOWLEDGEMENT

I take great joy in being able at long last to formally acknowledge that special group of people--my friends--whose help and encouragement have made it possible for me to successfully complete my academic sojourn here at the University of California. My heartfelt thanks go to Prof. Yuan T. Lee whose devotion to the scientific quest is only matched by his genuine concern for the welfare--academic as well as personal--of his students. The openness, and indeed enthusiasm, with which Prof. Lee shares his ideas with his colleagues and students, and the great respect he has for their opinions, these and other attitudes will long remain to be the targets of my emulation. Learning and working under the dedicated tutelage of Prof. Lee is undoubtedly the most treasured experience I will take away from Berkeley. My thanks also goes to Prof. George C. Pimentel with whom I had the privelege of working during the first two years of my graduate studies. His commonsense approach to science had de-mystified for me many-an-otherwise vaguely understood concept. It was also from Prof. Pimentel that I caught the laser-bug.

In preparing this manuscript, I am very fortunate to have the invaluable assistance of Dr. Kosuke Shobatake, Ms. Ann Weightman, and Ms. Antoinette Czerwinski. Dr. Shobatake has written many of the computer programs I used in analysing my scattering data. His unfailing willingness to lend a hand, even at his own inconvenience, is unparalled even among friends. I am most grateful to have his friendship. I am also thankful to Ms. Weightman for consenting to oversee the tedious task of getting this thesis properly typed up. Her efficiency and expertise in these matters have rendered the seemingly horrendous a lot less frightening.

I also wish to thank my colleagues in the molecular beam group at the Lawrence Berkeley Lab. I especially would like to express my gratitude to Dr. Cheuk Y. Ng, Mr. Randy Sparks, Ms. Carol Kahler, and Mr. Chris Becker. Cheuk is the best "big brother" anyone can ever hope for, and I am sure that he is every bit as good a teacher to his students at Iowa State University. Randy, his at times slightly stuffy self-assertiveness aside, is a true friend. I cannot even begin to count the time he helped me with car troubles; he being the undisputed local expert on Toyota's. Among the many other favors he has done me, Randy is also the one who introduced me to the world's greatest pizza. My thanks goes likewise to Carol and Chris who both deserve a medal for putting up with the many-a-dark moods I had when we collaborated on a project. I am also grateful to Dr. James Valentini, Mr. Rick Buss, Mr. Peter Schulz, Mr. Steve Sibener, Dr. Peter Tiedemann, and Ms. Marta Kowalczyk for their friendship.

My deepest thanks are reserved for my parents and my brother Danny. Their boundless love, understanding, and moral support easily transcend whatever oceans and mountains that separate us, and from them I am always able to draw my sustenance and inspirtation. In many ways, they have worked just as hard for this degree as I have, and to them therefore I dedicate this thesis.

THE INTERACTION OF RARE GAS METASTABLE ATOMS

Andrew Zun-Foh Wang

Materials and Molecular Research Division, Lawrence Berkeley Laboratory,
Department of Chemistry; University of California
Berkeley, California 94720

ABSTRACT

The physical and chemical properties of metastable rare gas atoms are discussed and summarized. This is followed by a detailed examination of the various possible pathways whereby the metastable's excess electronic energy can be dissipated. The phenomenon of chemi-ionization is given special emphasis, and a theoretical treatment based on the use of complex (optical) potential is presented. This is followed by a discussion on the unique advantageds offered by elastic differential cross section measurements in the apprehension of the fundamental forces governing the ionization process. The methodology generally adopted to extract information about the interaction potential from scattering data is also systematically outlined. Two widely studied chemi-ionization systems are then closely examined in the light of accurate differential cross section measurements obtained in this work. The first system is $He(2^3S)$ + Ar for which we were able to obtain an interaction potential which is in good harmony with the experimental results of other investigators. The validity of using the first-order semiclassical approximation for the phase shifts calculation in the presence of significant opacities is also discussed. The second reaction studied is He^*+D_2 for which we

have made measurements on both spin states of the metastable Helium. A self-consistent interaction potential is obtained for the triplet system, and reasons are given for not being able to do likewise for the singlet system. The anomalous hump proposed by a number of laboratories is analysed. Total elastic and ionization cross sections as well as rate constants are calculated for the triplet case. Good agreement with experimental data is found.

Finally, the construction and operation of a high power repetitively pulsed nitrogen laser pumped dye laser system is described in great details. Details for the construction and operation of a flashlamp pumped dye laser are likewise given.

Work performed under the auspices of the U. S. Department of Energy.

I. A SURVEY OF METASTABLE RARE GAS INTERACTIONS, AND THE EXPERIMENTAL TECHNIQUES USED IN THEIR INVESTIGATION

A. Introduction

The ground state of all rare gas atoms is $^1S_0$. If a single electron is promoted to the next higher (n, s orbital (thus leaving behind a vacancy in an otherwise filled (n-1) orbital: 1s for He*, 2p→5p for Ne*→Xe*), the atom is said to be in a metastable state. It is to be noted that this is but the lowest of possibly many metastable sates the atom can assume.[1*] It's metastability stems from the rigorous constraints imposed by quantum mechanical selection rules which render dipole coupling to the ground state extremely improbable. In the case of He*, the S→S transition is strictly forbidden; for the heavier atoms, the $\Delta J=0,\pm1$, $J=0\nrightarrow0$ rule is operative. As electric dipole radiation is denied to these excited atoms, they must have recourse to radiative mechanims of much lower probability[2] (such as electric quadrapolar or magnetic dipolar transitions), hence their long radiative lifetime.

As seen in Table I, the newly occupied (n) s orbital is very high above the ground state in energy; the metastable rare gas atom can therefore be regarded as a storehouse of electronic energy. Detailed knowledge of the various pathways whereby this excess energy can be dissipated is in great demand because of its application to atmospheric analysis[3], radiation chemistry[4], the design of more efficient gas lasers[5], as well as the understanding of such important theoretical concepts as direct

---

* Other metastable states arise from having the atom's outermost electron in Rydberg states with large principle quantum number. Although electric dipole transitions are allowed the coupling of the electron and nucleus is so weak that the probability of decay is very small.

and indirect potential curve crossing.[6] But before pursuing this, there are a few physical properties of the metastable state that warrant brief mentioning.

As the electron is farther away from the nucleus, the atom is by definition larger in size. Intuitively, the concomitant greater separation of charges should also result in a greater polarizability for the atom. This intuition is well borne out quantum mechanically where the polarizability of an atom is a measure of the ease with which an applied field can cause two or more of its electronic states to mix, thereby sharing their electronic properties. The extent of mixing is found to be inversely dependent on the energy difference between electronic states. Excited states, being energetically closer to more states, are therefore more polarizable than ground states. (Table II)

The energy required to ionize the metastable rare gas atom is also considerably lower as the electron is already raised high up above the ground state. Thus the ionization of the metastable now becomes a chemically accessible channel. This enables the metastable rare gas to be compared to other ground state atoms also having low ionization potentials, notably the alkali atoms. This comparison is tabulated in Table II. Thus for those reactions which primarily probe or involve the outermost valence electron, metastable atoms and alkali atoms should behave alike, and command comparable total reaction cross sections. This indeed has been verified experimentally.[7]

Metastable atoms are however unique in their excess energy storage. Their vast reservoir of chemical energy enables them to produce endothermic reactions such as dissociation and ionization. The particular reaction

path which a metastable rare gas atom follows depends naturally on the atom or molecule with which it interacts. We can group the various possible channels of energy dissipation into three broad categories (our attention will be confined to those reactions carried out under single collision conditions only):

(a) Direct E-E transfer. This is looked upon here as a resonance or near resonance interaction.* Thus the particle with which the metastable collides must have available energy levels close to that of the metastable. The effect of the energy transfer process is the total quenching of the metastable with simultaneous excitation of its colliding partner. There is generally negligible energy defect in the reaction.

(b) Chemical exchange reaction. This is possible when the colliding partner, of necessity a molecule, has a sufficiently strong electron affinity as compared to the ionization potential of the metastable. The metastable will then be ionized, and the electron it releases is handed over to the electronegative molecule. This newly formed molecular ion is unstable in the electric field of the positive rare gas ion. The inevitable dissociation of the molecular ion gives rise to a neutral and a negatively charged species. The latter will then combine with the rare gas ion to from a new ionic compound which is in general excited.

---

* The more subtle cases involving partial quenching of the metastable will not be considered here.

(c) Chemi-ionization. This happens when the ionization potential of the colliding partner is much lower than the electronic energy of the metastable. The former will then be ionized as the metastable is quenches, and the balance of the energy is carried off by the free electron.

Representative examples of these three classes of reactions, along with their rate constants and cross sections, are listed in Table 3 which provides an overall view of their respective reactivity. A more detailed discussion of each is given in the following section.

B. The Theoretical Picture

While there are a number of ways to qualitatively delineate the various reaction channels opened to the metastable rare gas atom, potential curves by and large afford the most lucid and unifying presentation. The main hindrance to their more widespread use in terms of making quantitative predictions lies unfortunately in their not infrequent unavailability with sufficient accuracy. For any but the simplest systems, attempts to calculate them from first principles are often frustrated by nearly insurmountable computational barriers; unfortunately their abstraction from experimental data is no less a trying undertaking. Yet, notwithstanding this general intractability, the interaction potential remains a very powerful conceptual tool. One finds that in analysing a particular reaction, it is still profitable to assume some reasonable forms for the pertinent potentials, and use these admitted artifacts to describe and understand the reaction mechanism. This is the approach adopted in this section.

(a) Direct E-E Transfer

This process is generally thought of as resulting from a direct crossing between potential surfaces representing the entrance and exit channels. If the crossing probability is P_x, and $P_x \ll 1$, then σ, the total cross section for this resonant energy transfer is experimentally found to be the product of a hard-sphere-like cross section modified by P_x times a Boltzmann factor.[8]

$$\sigma = 2(\pi R_x^2)(P_x) \left[\exp\left(\frac{\Delta E}{kT}\right)\right] \quad ; \quad \Delta E \lesssim 0 \qquad (1)$$

R_x is the crossing radius, and the factor 2 accounts for the two crossing points traversed in a trajectory. The Boltzmann factor arises out of the recognition that ΔE, the energy difference between the initial and final state at infinite separation must be less than zero before the two co-valent curves can cross at reasonable internuclear distances. Thus this is an endothermic reaction.

It should be noted that Eq. (1) is applicable only for fairly small cross sections. It is most valid for those cases where the quenching partner shares resonant energy levels with the metastable atom.[9] As a rough estimate of the range of validity of Eq. (1), let $R_x = 5.5$ Å, $\Delta E = -kT$, then $\sigma = P_x(90)$ Å^2. Since $P_x \simeq 0.1$ or less in general, the quenching cross sections from this model are not likely to exceed 10 Å^2.

For quenching processes with much larger cross sections, the above picture is found to be very inadequate.[10] However, instead of abandoning the use of potential curves all together, one remedy is the introduction of an intermediate charge transfer curve $M^+ - Q^-$ or $M^- - Q^+$. (The choice depends on the nature of the quencher Q, and M represents the metastable.) In this way, the entrance channel first crosses over to the charge transfer curve which then couples it to various exit channels as the charge transfer curve crosses them. The density of exit channels thus linked can be quit high, resulting in a large cross section for the transfer reaction.

Much work remains to be done in this somewhat neglected area of electronic energy transfer before theories and experimental results can become mutually supportive. But more will not be said in this paper about this process as it is beyond the scope of our present investigation. Its brief discussion has been included for the sake of completeness.

(b) Chemical Exchange Reactions

The key factor in this class of reactions is the low ionization potential of the metastable rare gas atom. The latter can therefore interact with the strongly electronegative halogen molecules in a manner similar to Alkali/Halogens reactions. The term "harpooning" has been specifically coined for this type of interaction. Many papers have reviewed this important mechanism.[11] The prime difference between the chemistry of the alkali metals and that of the metastable rare gas, with respect to the halogens, is that in the case of the alkali reactions, only one electronic state can be formed, while several potential product channels can exist for the metastable.

This is best illustrated with the aid of Fig. (1a). In it are drawn representative interaction potential curves for a metastable rare gas atom and a halogen-containing molecule. The metastable atom, M*, is chosen here to have an energy of 11 ev with an ionization potential of 5 ev. RX, the halogen-cotaining molecule, is to have an electron affinity of 2 ev. Phenomenologically, as the two interacting particles approach each other on the M*-RX curve, they will eventually reach a point of sufficient proximity as to allow the valence electron on M* to hop over to RX. Viewing this from RX's perspective, the molecule is suddenly induced to make a transition from the covalent RX potential to the ionic RX potential. If the crossing radius is not too large, and the interaction distance is not changing rapidly, this transition can be regarded as vertical, or Franck-Condon (see Fig. (1b)). The RX^- thus formed is very unstable with respect to the dissociation into $R + X^-$. While the main cause for this instability is the intense positive electric field originating from M^+ (which can exceed 10^9 V/cm when M^+ gets within 7 Å), other factors such as the incipient formation of RX^- in a highly excited vibrational state, or even in a purely repulsive state, can also expedite the dissolution of the molecular ion. This dissociation, as it proceeds in the vicinity of the M^+ ion, encourages the formation of the new ionic species M^+X^-. Thus the electron on M* is identified as the "harpoon" which, when cast towards an unwary RX (assuming that it approaches close enough), grabs hold of the molecule, pulls it apart, and abducts the halogen atom.

One can estimate the radius of crossing by recognising that originally the difference in energy between the M^+ -RX^- and M* -RX potential

curves at infinite internuclear separation is just IP(M*)-EA(RX). IP is the ionization of M*, and EA is the electron affinity of RX. However, as the particles get closer, Coulomb attraction comes into play, and the energy difference between the two potential curves diminishes. There will thus be a radius of interaction, R_c, reached where the Coulomb attraction e^2/R_c totally "absorbs" or counterbalances the initial energy gap. This is just another way of saying that the ionic curve becomes degenerate with (or crosses) the covalent curve at R_c. Thus, (in atomic units)

$$\frac{1}{R_c} = IP(M^*) - EA(RX) \qquad (2)$$

If the ionic curve does not interact with any other curves, then the cross section for the production of M^+X^-, a measurable quantity, should fall in the range of πR_c^2.

It must be emphasized that the validity of Eq. (2) rests on a number of assumptions, and when some of these are not strictly justified (as shown by unreasonable predictions), Eq. (2), as it is often applied to cross section estimates, would have to be amended. For example, if the computed R_c is very small, it is quite conceivable that Pauli repulsion forces or other interactions can become tantamount to the Coulomb attraction at that distance, and the resultant cross section must reflect that. At the other extreme, when the R_c obtained is too large, it is unrealistic to think that the electron can jump that great a distance. Also, Eq. (2)

assumes a flat covalent curve as well as pure Coulombic attraction at large R, these postulates must be critically examined for each case before much confidence can be invested in its quantitative reliability.[12]

As to the actual test of the harpooning model itself, we will discuss later on some preliminary relative cross section measurements on reactions involving heterogeneous halogen molecules with metastable rare gas atom.

(c) Chemi-ionization

So far the types of reactions we have considered involve either direct curve crossing or coupling via an intermediary ionic curve. However, not all quenching processes for the metastable atom follow these pathways. For those events that continue along the M*-A potential curve, where now A is any atom or molecule, several new quenching possibilities will open up as the colliding partners get sufficiently close. Specifically, for systems where E(M*), the energy of the excited atom M, is greater than the ionization potential of A (IP(A)), several different ionization processes can occur. These reactions constitute the focal point of this treatise, and therefore will be examined in great detail.

The processes we will look into are:

$$M^* + A \longrightarrow M + A^+ + e^- \qquad (3a)$$

$$\longrightarrow MA^+ + e^- \qquad (3b)$$

and in the case of A being a diatomic molecule, one can have,

$$M^* + A \longrightarrow M + B^+ + A + e^-$$

$$(M + B + A^+ + e^-) \qquad (3c)$$

$$\longrightarrow MB^+ + A + e^-$$

$$(MA^+ + B + e^-) \qquad (3d)$$

The above are all examples of irreversible energy conversion processes in which the irreversibility is due to the loss of an electron into the continuum.

The potential curves which depict these reactions are shown in Fig. (2a). The entrance channel, i.e. the covalent potential surface M^*-AB-- henceforth designated as V^*, is seen as a discrete state embedded in a continuum of exit channels, the lower bound for which is here designated as V^+. V^+ dissociates to $A + B^+$, and corresponds to the outgoing electron having zero kinetic energy. The continuum merely reflects the fact that the energy of the electron is continuously variable. Thus we have an infinite family of curves of the type $V^+ + \varepsilon$, where ε is the kinetic energy of the electron. This process is therefore analogous to the autoionization of a molecule; the main difference being that the initial

state here is continuous with respect to nuclear motion so that transitions to the continuum are possible at all separations of R, the internuclear distance.

Two implicit assumptions enter into the discussion of these ionization channels, which are just transitions from V^* to V^+. (a) The Born-Oppenheimer approximation holds: electronic and nuclear motions are separable (indeed, this underlines all our discussions using potential curves). (b) The transition between the two potentials, V^* and V^+, are vertical; it is of the Franck-Condon type: relative kinetic energy of the nuclei does not change during the transition. The validity of assumption (b) is demonstrated by the similarity between the relative populations of vibrational states of molecular ions produced via chemi-ionization with those resulting from photoionization.[12] The latter is of course a Franck-Condon process.

We now have the following energy conservation relationships (for a certain internuclear distance R):

(i) from the conservation of energy

$$V^*(R) - V^+(R) = E_{el} \tag{4}$$

where E_{el} is the kinetic energy of the ejected electron.

(ii) Since the orbital angular momentum is, to a good approximation, conserved,

$$E_k(\infty) + V^*(\infty) - V^*(R) = E_k'(\infty,R) + V^+(\infty) - V^+(R) \qquad (5)$$

$E_k(\infty)$ is the relative kinetic energy in the incoming channel, and $E'(\infty,R)$ is the outgoing relative kinetic energy evaluated at R. If we let

$$E_0 = V^*(\infty) - V^+(\infty)$$

then,

$$E_k'(\infty,R) = E_k(\infty) + E_0 - E_{el} \qquad (6)$$

When $E_{el} > E_k(\infty) + E_0$, the reaction products find themselves with negative relative kinetic energy, i.e., truly bound; this corresponds to the case of associative ionization (3b). By contrast, when $E_k(\infty) + E_0 > E_{el}$, the ions formed have enough energy to separate, the Penning ionizaton results (3a). Reactions (3c) and (3d) become likely when the associative ion $(MAB)^+$ is formed in a highly excited vibrational state and is therefore very susceptible to dissociation.

At this point, we hasten to mention that one feature about the potential curves has been omitted in Fig. (2a). It is that the relevant potentials for radial motion are actually V^*, and V^+, plus the centrifugal term $(\hbar^2 l^2/2\mu R^2)$. Fig. (2b) shows the correction. As indicated, the transition at R' leads to a final translational energy which is classically a bound vibrational state of $(MB)^+$, but quantum mechanically, it is metastable and will dissociate to $M + B^+$. So whether this ionization process is considered Penning or associative depends on one's detection scheme. We will henceforth assume that the detection time is slow compared to the characteristic lifetime of the $(MB)^+$ ion, so that a transition at R' is considered as Penning ionization. Everything else in the preceding discussion does not change because only energy differences were involved.

The energetic relations (4) to (6) provide little information on the actual process of electron ejection. Two mechanisms have been proposed for it (see Fig. (2c)). (a) The radiative channel: in the course of the collision, the perturbed metastable emits a photon, $h\nu = E(M^*-M)$, which in turn is absorbed by the target particle B, leading to its ionization.[13,14] (b) This channel is characterised by tunnelling of an electron on B, followed by an Auger emission of the excited electron on M^*.[15] In other words, M^*, in being quenched to its ground state, has effectively yielded its excited electron to the continuum in exchange for one belonging to B. This is in close analogy to the theory of Auger emission of electrons from metal surfaces by metastables as given by Hagstrum.[16]

Mechanism (a) would predict that the singlet state, by virtue of its much shorter radiative lifetime, should yield a much greater ionization cross section than that of the corresponding triplet state. Mechanisms (b), on the other hand, would make no such a priori claim about the relative magnitude of singlet to triplet cross section; it does, however, say that ionization would become very unlikely when the internuclear distance gets large. The experimental results that have accumulated are in general support of mechanism (b)[17], though an enchancement factor can indeed be attributed to mechanism (a).[18]

The final remaining question that needs to be dealt with is the probability of making a transition from V^* to V^+ as a function of R. This is generally described in terms of a transition rate W(R). As suggested earlier, W(R) is defined at each internuclear separation, and does not depend on the state of nuclear motion. Much theoretical effort has been directed towards calculating this important quantity from first principles, but so far without striking success. What is customarily done is to assume a particular functional dependence for W(R), and use that to fit available experimental data. The primary requirement placed on W(R) is that it should be very small at large R, but increasing rapidly towards small R.[19]

The process of chemi-ionization will be extensively discussed in Chapter II.

C. Experimental Techniques Used to Investigate Metastable Reactions

There are a number of experimental methods which are currently employed to study the interactions of metastable rare gas atoms. No attempt will be made here to provide an exhaustive survey. Instead, several principal techniques will be briefly described, and their limitations identified. Attention will then be directed towards the details of the molecular beam apparatus we used in our studies.

(a) Discharge Flow System.

The metastable atoms are generated by flowing the rare gas through a hollow, cold-cathode discharge. The concentration of the metastable is monitored at several positions along the tubular flow reactor by atomic absorption spectroscopy. Quenching rate constants for various reagent gases are determined by adding sufficient amount of the latter (so that concentration of reagent>concentration of metastable) to give pseudo-first-order kinetics for the decay of the metastable atom in the flowing afterglow.[20] Cross sections are then computed by dividing the rate constants obtained by the mean Boltzmann speed which essentially characterizes the temperature of the reaction.[20,21] One notes that the reliability of the quantitative information deriving from a flow-tube set-up hinges, among other things, on the accuracy with which the flow rate can be calibrated. This is a non-trivial undertaking, as it has been shown that the normally assumed simplification--the "plug-flow approximation"--must in many cases be judiciously refined.[22]

For those cases where the quenching of the metastable proceeds via a chemical exchange reaction leading to the formation of an electronically excited product molecule, an additional handle on this process is provided for by the flow-tube apparatus. The chemiluminescence spectra can now be recorded at appropriate points along the tube. Such spectral information greatly aids in the construction of the potentials involved in the reaction.[23,24] However, valuable information on the initial population distribution in the products' energy levels is oftentimes lost as it is difficult to ensure single collision conditions with the pressures of the reagents normally used.

(b) Gas Cell Fluorescence.

The rare gas is premixed with its prospective quencher in a transparent cell, and is raised to its metastable level by either an electron pulse[24] or a resonance lamp.[25] This type of apparatus generally affords only spectral analysis of excited product molecules.

(c) Beam-Gas Experiments.

The metastable atoms are now produced in the form of a beam which is made to intersect a tenuous atmosphere of the quencher molecules. At least two vacuum compartments are required in this set-up. One is for the production of the metastable atoms, and is known as the source chamber. The other is the scattering chamber which is filled initially with the quencher; this is coupled to the source chamber via a small hole through which the metastable beam can enter.[26]

Nearly everything that can be done in a flowing afterglow tube can be likewise carried out in a beam-gas set-up. Indeed, the latter has proven to be more flexible in some ways. The collision energy, for example, can be varied with much greater ease. Also, with fewer critical calibrations involved, more confidence can be invested in the quantitative information that comes out.

(d) Beam-beam Experiments

(i) Merging beams

The application of merging beams to the study of metastable interaction is quite recent.[27] The essential idea to this technique involves two initially ionic beams which are accelerated to high laboratory energies electrostatically; these are subsequently neutralized by passing them through appropriately designed charge-transfer cells. Upon the beams' exit from these cells, whatever residual ions that remain are deflected away by the use of a potential. The now neutral beams are then made to travel in the same direction along a common axis.

Several unique advantages are thus afforded: (a) a wide range of collision energies, spanning from 0.01 ev to 20 ev, can be obtained in a continuous fashion with very little energy spread; (b) the longer interaction length can greatly increase product signal intensities; (c) the collection of various product molecules for total cross section measurements is straightforward, their energy distribution is also easily measured.[28]

(ii) Crossed Beams

This technique should require no elaborate introduction. Its extensive contributions to the understanding of many classes of reactions have been reviewed in a number of articles.[29] Attention here will therefore be devoted to just how our laboratory has applied it to the study of metastable rare gas interactions.

The apparatus to be described is used specifically for those reactions involving chemi-ionization by the metastable atom which, in the following discussion, is taken to be He* unless otherwise stated. An energy level diagram for He is shown in Fig. 3. Our machine allows us to scan the differential cross section for such processes as a function of the collision energy, and also to monitor the relative intensities of the various ions produced. It will be shown in Chapter II that the elastic differential cross sections thus obtained can be very instrumental in the determination of the interaction potential involved.[30]

A schematic diagram of our experimental arrangement is shown in Fig. 4. The metastable atoms are produced by crossing a supersonic He beam with an electron beam perpendicular to it. The electrons are emitted by a filament which is made from a 10 mil thoriated tungsten wire. The filament is normally run at 5-6 amperes. The electrons thus produced are accelerated through a potential of 250 V, and collected by an anode made up of razor blades. These blades are stacked in such a manner as to discourage the electrons which hit them from rebounding. The optimum separation between anode and cathode is found to be about 1/4 inch. When the filament is properly aged, i.e., initially coated

with a layer of carbon, and then heated up under vacuum for about six hours to allow the thorium atoms which have much higher emissivity to come to the surface, the emission current that can be collected is typically 60 mA. For a pressure of 500 torrs of He behind the supersonic nozzle, and after collimating the metastable beam by a slit assembly to give about 1% FWHM, one can obtain 10^{10} metastable atoms/sec. This is measured by the electron current (read directly off a calibrated electrometer) ejected from a Be-Cu target whose relatively high work function makes it an ideal metastable rare gas atom monitor.[31]

In order to compensate for the momentum transfer in the excitation process which causes the direction of the metastable beam to deviate from that of the ground state helium atom beam,** the nozzle, skimmer and filament assembly is mounted on a bulkhead which can then be rotated around the crossing point until the metastable beam registers a maximum intensity as measured by the aforementioned Be-Cu cup. The latter is situated at 0° as shown in Fig. 5.

The metastable atom beam produced under the conditions described above consists of approximately 85% singlets and 15% triplets.[33] These two states of He are quite different in their reactivity, and we therefor must isolate the contribution from each in our cross section measurements. This is accomplished optically by the use of a quenching lamp which effectively gets rid of all the metastable singlets.

** For an excitation of 20 ev, and the electron beam at normal incidence, the ratio of the recoil velocity of the He beam to its initial velocity (10^5 cm/sec) is 0.293.

The pertinent transition is

$$h\nu(2^1P \xrightarrow{2\mu} 2^1S) + He(2^1S) \rightarrow He(2^1P) \rightarrow He(^1S) + h\nu(584\ \text{Å})$$

The corresponding process for the triplet does not occur because the He (2^3S), if excited to the (2^3P) state, returns to the (2^3S) state. This quenching lamp is also mounted on the bulkhead, and is made of pyrex tubing coiled up in the form of a spiral (1.5" ID) covering a linear extent of about 2 inches. 1/6 inch tungsten rods serve as the electrodes which are sealed at the two ends of the tube; adjacent to the electrodes are placed gas inlet and outlet ports. This lamp snugly fits into a copper jacket which is water-cooled; thermal contact is provided for by a special silicon RTV compound. The power to the lamp is afforded by a DC supply capable of delivering up to 200 mA at 3 kV. Normal operation, however, only requires 2000V and 50 mA. A steady continuous flow of fresh helium is maintained in the lamp by means of a small throttled mechanical pump. A spark, delivered via an insulated wire placed just outside of the pyrex tubing, is necessary to get the lamp started. It is also found that the lamp's stability is greatly enhanced when a string of six 10 watts 750 ohms resistors are connected in series to it.

One final note about this beam source is that since the electrons are crossed perpendicular to the beam axis, the velocity distribution of the metastable beam does not differ appreciably from that of the

ground state beam, which has been measured to have a velocity spread of 6-8%.[33]

Secondary beams of Ar and D_2 are similarly produced from a free jet supersonic expansion. Their velocity spreads are also estimated to be 6-8%, and they are collimated to about 2°. The primary and secondary beams are crossed at 90° in a collision chamber, and elastically scattered metastable helium atoms are detected with a rotatable detector. This detector essentially consists of a Be-Cu surface which is oriented to intercept the metastable helium atoms at an incident angle of 45°; a scintillation counter is then used to count the electrons ejected from the Be-Cu surface. In order to maximize the collection efficiency of this scheme, a voltage of -20 kV is applied to the Be-Cu target to give 20 kV electrons to the aluminum coated organic scintillator. The photons thus emitted are counted by a PM tube operated at 1250 V. The subtraction of the background noise is accomplished as follows: the secondary beam is first modulated by a 150 Hz tuning fork chopper located in-between the skimmer-collimator region. This modulation is then synchronized to the gating of a dual scaler into which is fed the PM tube signals after amplification and discrimination. Thus for a particular chosen counting period, which generally ranges from 25 sec to 200 sec, the two channels of the scaler are alternately enabled and disabled many times. Great care is taken to ensure that the total counting time for each channel is the same. The difference in counts between the two channels after the preset time interval has elapsed is then the true signal.

Differential cross sections of mixed metastable helium atoms are first measured with the quenching lamp off, then the scattering of pure

He (2^3S) is measured with the lamp on. The difference between the measurements with the quenching lamp off and on yields the differential cross sections of He(2^1S). Angular distribution measurements are time-normalized by periodically returning the detector to an (arbitrary) angle chosen as reference in order to account for long term drifts in beam intensity as well as detector sensitivity. One contribution to the background signal is the inherent thermal noise in the PM tube, thus provisions are made to allow cooling of the PMT to dry ice temperature. What is done in actuality is to cool a copper disc in contact with the outer jacket of the PM tube with liquid nitrogen, and the final desired operating temperature (which should never be at N_2 temperature) is reached and maintained by the use of heating tapes wrapped around this whole assembly. Thus when it is necessary to cool down the detector in this fashion, care must be taken to ensure that the temperature of the PM tube, as monitored by a thermocouple connected to a chart recorder, only drifts within tolerable limits.

Ions produced by the quenching process are analysed by a quadruple mass spectrometer installed just above the collision center with its axis perpendicular to the plane defined by the cross molecular beams. A repeller plate below the collision center and a three-element focusing lens effectively sends all ions produced in the collision region into the entrance of the mass spectrometer.

Finally, the collision energy can be varied by one of two ways. At the high energy end (above room temperature), the He nozzle is made in the form of an oven, the heating elements for which consist of tantalum

wires threaded through ceramic rods. The wires can be resistively heated by a current, the exact value of which depends on the temperature desired. At the low energy end (below room temperature), provisions are made in the secondary beam source for cryogen cooling of the beam.

REFERENCES - CHAPTER I

1. D. R. Bates, K. L. Bell and A. E. Kingston, Proc. Phys. Soc. 91, 288 (1967).

2. V. Cermak, and Z. Herman. Coll. Czech. Chem. Commun. 29, 953 (1964).

3. A. P. D'Silva, and V. A. Fassel, Anal. Chem. 44, 2115 (1972).

4. G. S. Hurst, and C. E. Klots, Ad. in Radiation Chemistry, edited by M. Burton and J. L. Magee (1973).

5. See for example:

   (a) J. B. Gerardo, and A. W. Johnson, IEEE J. Quan. Electron. QE-9, 748 (1973).

   (b) J. B. Gerardo, and A. W. Johnson, J. Appl. Phys. 44 4120 (1973).

6. D. L. King and D. W. Setser, Ann. Rev. Phys. Chem. 27, 407 (1976).

7. D. H. Winicur, and J. L. Fraites, J. Chem. Phys. 62, 63 (1975).

8. H. Z. Cummings, and H. L. Swinney, Prog. Opt. 8, 133 (1970).

9. L. G. Piper, J. E. Velazco, and D. W. Setser, J. Chem. Phys. 59, 3323 (1973).

10. R. G. Brown, and D. Phillips, J. Chem. Soc. Faraday Trans. 270, 630, (1974).

11. D. R. Herschbach, Advam. Chem. Phys. 10, 319 (1966).

12. W. C. Richardson, D. W. Setser, D. L. Albritton, and A. L. Schmeltekofpf, Chem. Phys. Lett. 12, (1971).

13. K. Katsuura, J. Chem. Phys. 42, 3771 (1965).

14. M. Matsuzawa, and K. Katsuura, J. Chem. Phys. 52, 3001 (1970).

15. H. Hotop, and A. Niehaus. VIth International Conference on the Physics of Electronic and Atomic Collisions, Cambridge, Mass. July 1969, p. 882, The MIT Press, Cambridge, Mass., 1969.

16. H. D. Hagstrom, Phys. Rev. 104, 1516 (1956).

17. H. Hotop and A. Niehaus, Zeit. für Physik. 215, 395 (1968).

18. H. Hotop, and A. Niehuas, Z. Phys. 238, 452 (1970).

19. W. H. Miller, C. A. Slocomb, and H. F. Schaefer, J. Chem. Phys. 56, 1347 (1972).

20. M. I. Golde, B. A. Thrush, Chem. Phys. Lett. 29, 486 (1974).

21. J. Tellingshuisen, J. M. Hoffman, G. C. Tisone, and A. K. Hays, J. Chem. Phys. 64, 2484 (1976).

22. D. H. Stedman and D. W. Setser, Prog. React. Kinetics 6, 194 (1971).

23. L. A. Gundel, D. W. Setser, M. A. A. Clyne, J. A. Coxon, and W. Nip., J. Chem. Phys. 64, 4390 (1976).

24. M. F. Golde, J. Mol. Spectr., 58, 261 (1975).

25. J. E. Velazco and D. W. Setser, Chem. Phys. Lett. 25, 197 (1974).

26. J. L. Gole, D. R. Preuss, and C. L. Chalek, J. Chem. Phys. 66, 548 (1977).

27. R. H. Neynader and G. D. Magnuson, J. Chem. Phys. 61, 749 (1974).

28. R. H. Neynaber and G. D. Magnuson, J. Chem. Phys. 62, 4953 (1975).

29. See for Example. Faraday, Disc. of the Chem. Soc. 55 (1973).

30. (a) Z. F. Wang, A. P. Hickman, K. Shobatake and Y. T. Lee, J. Chem. Phys. 65, 1250(1976).

(b) C. H. Chen, H. Haberland, and Y. T. Lee, J. Chem. Phys. 61, 3095 (1974).

31. D. A. Maclennan, Phys. Rev. 148, 218 (1966).

32. H. Haberland, C. H. Chen, and Y. T. Lee in Atomic Physics, (Plenum, New York 1973), 3, p. 339.

TABLE I

RARE GAS METASTABLES

	X	M	Energy E_M(eV)	Lifetime τ(sec)	$E < E_m$ Desig.	ΔE	R or M	$E > E_m$ Desig.		R or M
He	1^1S_0	2^3S_1	19.82	$4.2\times10^{+3}$	X	19.82	—	2^1S_0	0.79	M
		2^1S_1	20.61	2×10^{-2}	2^3S_1	0.79	M	$2^3P^o_{2,1,0}$	0.30	M
Ne	2^1S_0	$3^3P^o_2$	16.62	>0.8	X	16.62	—	$3^3P^o_1$	0.05	R
		$3^3P^o_0$	16.72	>0.8	$3^3P^o_1$	0.05	R	$3^1P^o_1$	0.12	R
Ar	3^1S_0	$4^3P^o_2$	11.55	>1.3	X	11.55	—	$4^3P^o_1$	0.07	R
		$4^3P^o_0$	11.72	>1.3	$4^3P^o_1$	0.10	R	$4^1P^o_1$	0.10	R
Kr	4^1S_0	$5^3P^o_2$	9.92	>1	X	9.92	—	$5^3P^o_1$	0.12	R
		$5^3P^o_0$	10.56	>1	$5^3P^o_1$	0.53	R	$5^1P^o_1$	0.08	R
Xe	5^1S_0	$6^3P^o_2$	8.32	?	X	8.32	—	$6^3P^o_1$	0.12	R
		$6^3P^o_0$	9.45	?	$6^3P^o_1$	1.01	R	$6^1P^o_1$	0.12	R

$E < E_m$: Desig. -- Nearest Lower-Energy State
ΔE -- Energy Diff. of this State with M
R or M -- Nature of this State
R - Radiative M - Metastable

$E > E_m$: Desig -- Nearest Higher Energy State
ΔE -- Energy Diff. of this State with M
R or M -- Radiative or Metastable

TABLE II

COMPARISON OF METASTABLE RARE GAS WITH ALKALI ANALOGS

	Polarizability (A^3)	Ionization Potential (eV)	Valence Electron	Mass (amu)	Electron Designation
He^* $^1S_0$	65.34	3.97	2s	4.00	$^1S_0$
He^* $^3S_1$	46.6	4.76			$^3S_1$
Li	24.3±0.5	5.39	2s	6.94	$^2S_{1/2}$
Ne^*	27.6 27.6±0.5	4.94	3s	20.2	$^3P_2$
Na	23.6±0.5 24.4±1.7 24.0	5.14	3s	23.0	$^2S_{1/2}$
Ar^*	48.4 47.1±1.0 47.8	4.21	4s	39.9	$^3P_2$
K	45.2±3.2 44.3	4.34	4s	39.1	$^2S_{1/2}$
Kr^*	43.8±1.0 50.6	4.08	5s	83.8	$^3P_2$
Rb	48.7±3.4 48.0	4.18	5s	85.5	$^2S_{1/2}$
Xe^*	62.0±1.2 63.2	3.81	6s	131.3	$^3P_2$
Cs	63.3±4.6 61.5	3.89	6s	132.9	$^2S_{1/2}$

TABLE III

REPRESENTATIVE INTERACTIONS INVOLVING A RARE GAS METASTABLE ATOM AND ANOTHER ATOM OR DIATOMIC MOLECULE.

Chemical System	Rate Constants (300°K) (10^{-11} cm^3 sec^{-1})	Type (See Text)	Cross Section ($Å^2$)
$He(2^3S_1)$ + Ne	6.45	a	4.71
$He(2^1S_0)$ + Ne	0.36	a	0.28
Ar* + Kr	0.62	a	1.3
Ar* + CO	1.4	a	2.3
Ar* + HBr	72	b	150
Xe* + N_2	1.9	a	3.7
Xe* + O_2	22	a	44
Xe* + $C\ell_2$	65	b	176
$He(2^3S_1)$ + H_2	0.92	c	3.9
$He(2^1S_0)$ + H_2	0.73	c	3.2

FIGURE CAPTIONS - CHAPTER I

Fig. 1a Schematic showing entrance and exit channels for reactive quenching (heavy arrow) of M* by a halogen-containing molecule RX.

Fig. 1b Franck-Condon like transition from the covalent RX potential curve to the ionic RX^- potential curve.

Fig. 2a Pertinent potential energy curves for the chemi-ionization process.

Fig. 2b Schematic showing the result of adding the centrifugal term to the potential energy curves.

Fig. 2c Two possible mechanisms for chemi-ionization.

Fig. 3 Energy levels of He.

Fig. 4 Schematic of molecular beam apparatus used in the study of metastable atom reactions.

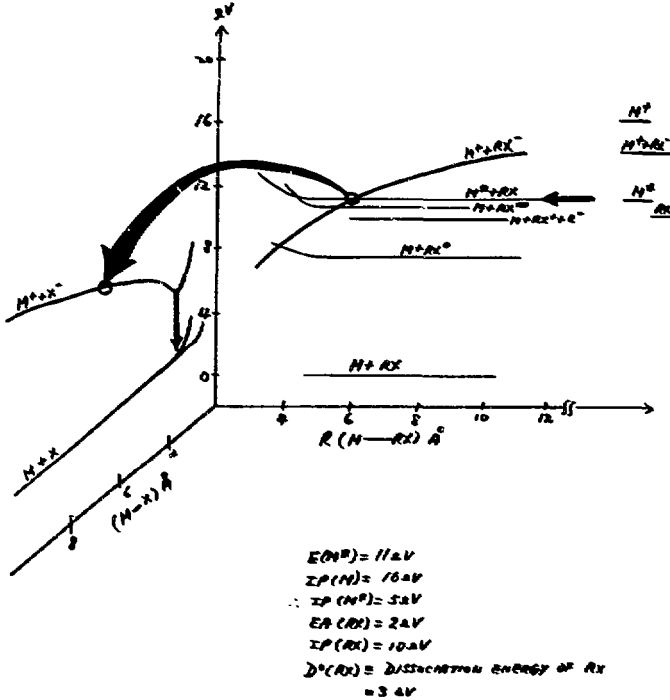

XBL 7710-6773

Fig. 1a

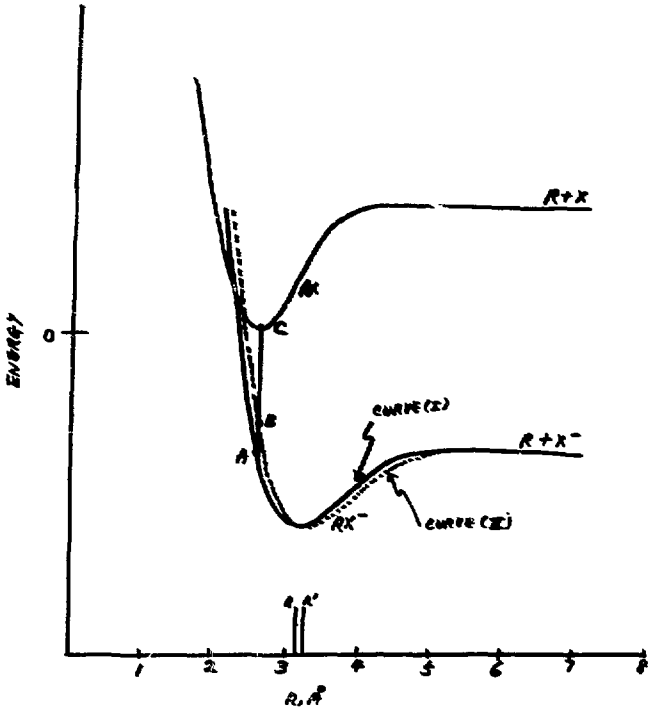

Fig. 1b

XBL 7710-6772

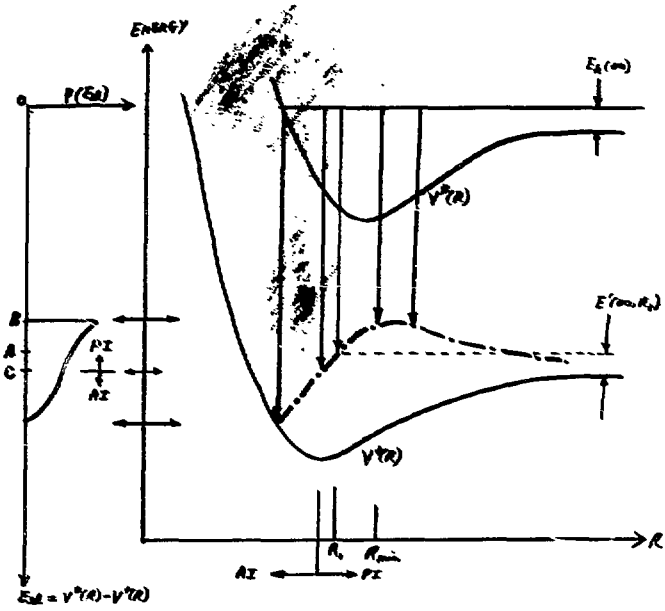

Fig. 2a

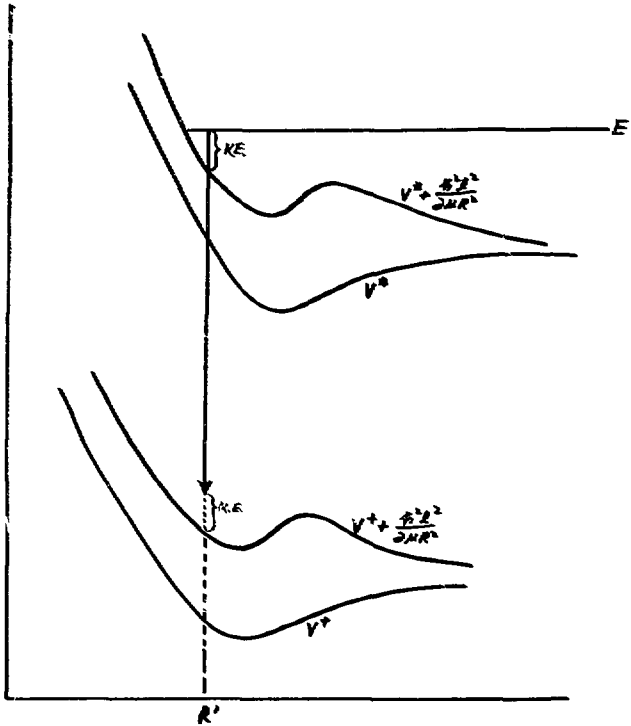

XBL 7710-6771

Fig. 2b

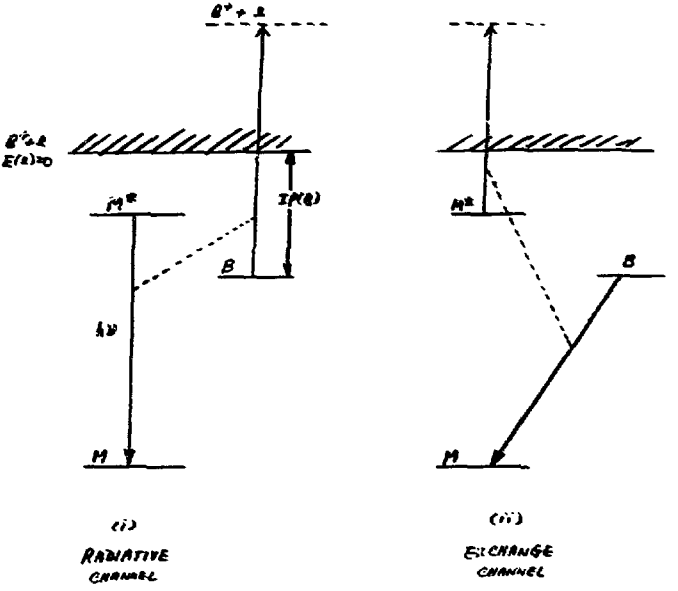

XBL 7710-6755

Fig. 2c

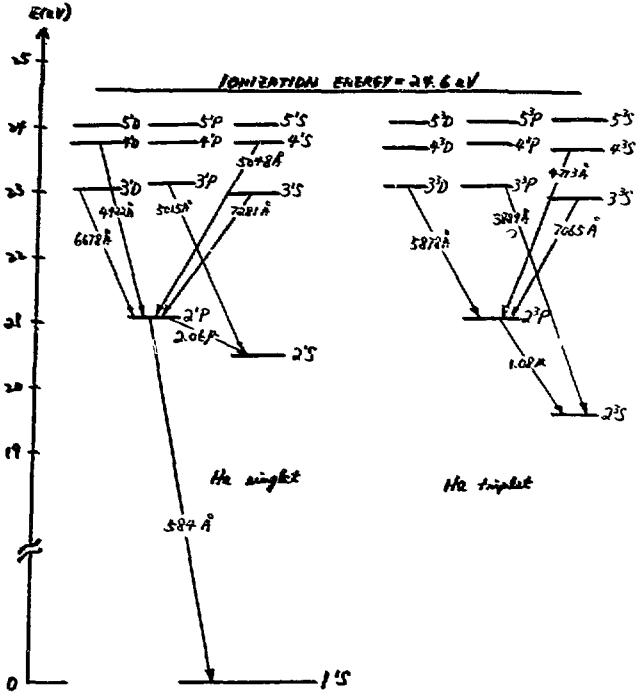

XBL 7710-6777

Fig. 3

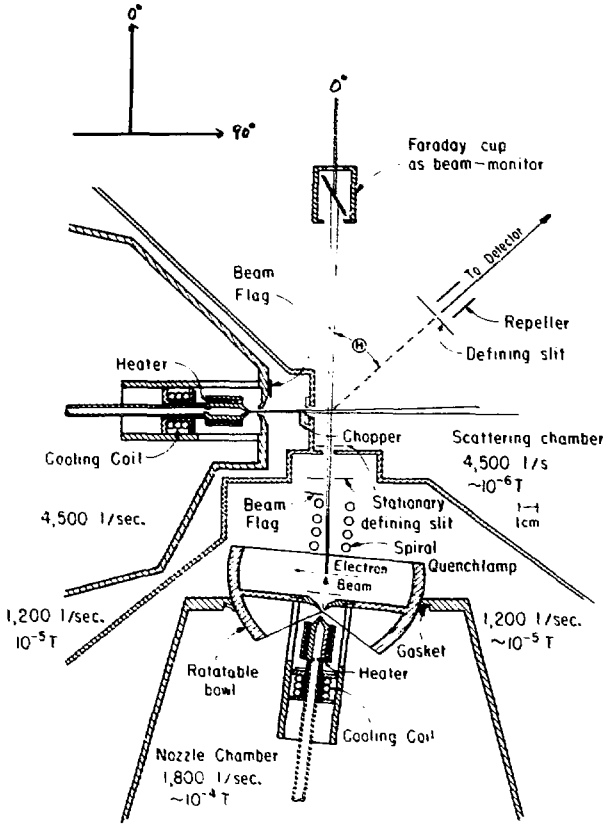

Fig. 4

XBL 7710-6775

II. THE THEORETICAL BASIS FOR OPTICAL POTENTIAL ANALYSIS AND ITS COMPUTATIONAL IMPLEMENTATION

A. Theoretical and Computational Aspects of Chemi-Ionization

The assertion is made in Chapter I that in the case of chemi-ionization by a metastable rare gas atom, three quantities are necessary and sufficient to describe the event. This claim will now be qualified and elaborated on in this chapter. We will show formally that all the available experimental information on this class of reaction can indeed be derived from the three quantities, V^*, V^+ and Γ, which are respectively the covalent interaction potential (the entrance channel), the ionic interaction potential (the exit channel), and the ionization width Γ (the coupling between the two potentials). (Γ is related to the transition rate mentioned in Chapter I by $\Gamma = \hbar W$.) This means that as long as we confine our inquiry to <u>what</u> happens in a chemi-ionization event, V^* V^+ and Γ will prove quite adequate. However, there is a larger and more fundamental question we must ultimately address, namely <u>why</u> the ionization proceeds in a particular manner. This question is generally left begging even after knowledge of a semi-empircal set of V^*, V^+ and Γ is secured. This is due to the fact that we have arbitraribly lumped most of our ignorance about this process into one quantity, namely Γ. Γ, in this sense, is very much like a black box, about which the only thing we can say for certain is that once the interacting system comes into its range of influence, ionization will proceed with a finite probability.

Some progress is currently being made in the direction of clarifying some of the fundamental forces which act to bring about a particular Γ. It has been shown that this classical probability function $\Gamma(R)$ can be expressed in quantum mechanics as being proportional to the square of the

expectation value the coupling function between the two degenerate electronic states V^* and $(V^+ + \varepsilon)$ (ε is the kinetic energy of the free electron). The coupling function is just the operator (H-E), where H is the full electronic Hamiltonian (the Born-Oppenheimer approximation is assumed), and E is the resonance energy measured with respect to V^+. Thus the theoretical probelm is one of configuration interaction between discrete and continuum electronic states of the system, and at the same time the problem of the relation between such a coupled electronic state and the collision. When Γ is framed in this light, it would seem that we are one step closer to discovering what caused Γ; however, we must exercise some caution here, for it remains to be shown that the evaluation of the aforementioned coupling operator (H-E) can be carried out using conceptually meaningful electronic orbitals, and that the various approximations that must be made to render the calculations feasible do not inadvertently fog up the meaning of Γ. There is therefore always the possible pitfall that we are defining one unknown in terms of another, thus augmenting our actual knowledge about the process but little.

On the experimental front, we have at the moment conceded the game at the Γ level. Our measurements cannot probe beyond the effect of Γ on quantities like differential and total cross sections. However, it is our hope that when a sufficient number of these metastable rare gas ionization processes has been studied, and the assortment of Γ's that govern them duly catalogued, the latter will cover a wide enough terrain on which it is more likely to discern possible correlations between chemiionization and fundamental physical properties such as polarizabilities, and electron affinities. In this context, the work we report here represents part of our contribution to this ongoing endeavor.

The present chapter seeks to outline the theoretical basis[1] for our ability to deduce from appropriate experimental data the shape and size of V^* and Γ. These two quantities are now combined in our analysis as one potential defined on the complex plane. Thus we have V^{opt}, better known as the optical potential, to be $V-(i/2)\Gamma$ we have dropped the asterick on V^*). At times for simplicity, we will also let $V_I = (1/2)\Gamma$. The effect of inserting a complex potential into the Schrodinger equation is to cause the wavefunction to take on a complex phase shift. Unlike the theoretician, we will not be particularly concerned about the exact form of this wavefunction since the calculations of our experimental observables do not invoke it. It will instead be emphasized and explicitly shown that the complex phase shifts themselves play a very crucial role in determining the shape of the differential cross section as well as the magnitude of the total cross sections. We will indicate under what circumstances we can hope to unambigously unravel the optical potential V^{opt} from our measurements. And if V^{opt} can be obtained with sufficient accuracy, we will also indicate what additional information one needs to ascertain the last remaining quantity in the trio (V^*,Γ,V^+), i.e.V^+.

Finally, in this chapter we will document and briefly discuss the various computer programs employed in the analysis of our experimental data.

B. The Optical Potential and the Resultant Phase Shifts.

The optical potential, as implied by its name, is analogous to the description of light through matter using a complex index of refraction. In the case of light passing through an absorptive medium, the complex

index of refraction. In the case of light passing through an absorptive medium, the complex index of refraction permits a simultaneous description of both the elastically scattered beam of light (by virtue of the index's real part) as well as possible absorptive phenomena (accounted for by the index's complex component). For the chemically reactive analog, the optical potential (or the effective complex potential) serves to describe both the elastic and reactive scattering of impacting reactants. Thus reaction corresponds to absorption. The virtue of such an approach, whether it is applied to light or to a chemical reaction, is that the optical description can be implemented with equal ease for either the simplest or most complicated situations. The reason for this is that independent of the actual number of degrees of freedom for the experimental system, the optical approach always relies on an effective one-dimensional complex description.** For example, the use of an index of refraction for light passing through matter in no way depends upon the internal complexity of the matter which is absorbing or bending the light rays. The same invariance exists for the optical model of a chemical reaction.

The assumption of a local complex potential underlines all the calculations in this chapter. Its validity will be more critically assessed in Chapter III when we examine the He* + Ar system.

To arrive at expressions for the differential and total cross sections resulting from scattering with a complex potential, our foregoing discussion

---

** We should note that if the optical potential is rigorously defined, it becomes non-local and energy dependent. However, in most cases a local Born-Oppenheimer type approximation should be rather good, because the loss from incoming channel is due to an electronic transition which is very fast compared to the heavy particle motion.

suggests that we should start off by securing a general formula for the complex phase shift, and then try to express it explicitly in terms of V and V_1. While it is possible to derive this by actually solving the Schrodinger equation for the complex potential, it would not be advisable for us here to carry out this cumbersome calculation which in fact has been performed by several people (see for example, Mott and Massey, Goldberger and Watson, Harvey). Qualitative arguments such as the one offered by Schiff enable us to arrive at the desired expression by analogy with the derivation for the WKB phase shift for a strictly real potential V. The Schrodinger equation in this case is

$$\left\{ \frac{d^2}{dR^2} + \frac{2\mu}{\hbar^2} [E-V(R)] - \frac{\ell(\ell+1)}{R^2} \right\} \psi^{\circ}(\ell,R) = 0 \qquad (1)$$

and the corresponding phase shift is then found to be

$$\eta_0(\ell) = \int_{r_c}^{\infty} (x^{\frac{1}{2}}-k)\, dR - kr_c + \tfrac{1}{2}\pi(\ell+\tfrac{1}{2}) \qquad (2)$$

where we have used the notation

$$X(E,\ell,R) = \left(\frac{2\mu}{\hbar^2}\right) [E-V(R)] - \frac{(\ell+\frac{1}{2})^2}{R^2} \qquad (3)$$

and r_c is defined by the relation $x(r_c)=0$. r_c is generally known as the classical turning point, the point where the initial kinetic energy just equals the energy of the effective potential. k is the wave vector with magnitude $\mu v/\hbar$, v being the relative velocity.

The complex phase shift $\eta(\ell)$ is therefore written in an analogous manner as Eq. (2),[2]

$$\eta_\ell = \int_{z_c}^{\infty+i\infty} \left[F(z)^{\frac{1}{2}}-k\right] dz - kz_c + \tfrac{1}{2}\pi(\ell+\tfrac{1}{2}) \qquad (4)$$

where we see that essentially r_c has been replaced by its counterpart on the complex plane z_c, and a complex function F(z) is substituted in place of x(R).

Our main task is to determine z_c, the complex turning point defined by

$$F(z_c) = 0 \qquad (5)$$

But first, F(z) must be determined. The discussion below will follow in part that given by Rosenfeld and Ross.[2] In the complex potential, $V_1=(1/2)\Gamma$ must be greater than zero for absorption of the incident beam. The Schrodinger equation now becomes

$$\left\{ \frac{d^2}{dR^2} + \frac{2\mu}{\hbar^2} [E-(V-iV_1)] - \frac{\ell(\ell+1)}{R^2} \right\} \phi(\ell,R) = 0 \qquad (7)$$

By analogy with Eq. (1), (2), and (4), and extending into the complex plane we see that the complex function F must be

$$F(E,\ell,z) = \frac{2\mu}{\hbar^2} \left[E - V(z) + iV_1(z)\right] - \frac{\ell(\ell+1)}{z^2} \qquad (8)$$

We recognize at this point that as $R\to\infty$, ϕ in Eq. (7) must asymtotically approach the eleastic scattering wave

$$\psi(\ell,R) \underset{R\to\infty}{\propto} \sin[kR-\tfrac{1}{2}\ell\pi + \eta(\ell)] \qquad (9)$$

In other words, as has been implied in our previous discussion, as long as we are far enough from the scattering center, the net effect of whatever potential (complex or otherwise so long as it decays faster than 1/R) that existed there (whose influence can no longer be felt as $R\to\infty$) is to bring about a phase shift in the scattered wave.

examine F(z) more closely, it would be very convenient to first identify its real and imaginary part. We do this by taking the limit as the inelastic processes become negligible, then, Im(F) must go to zero, and Eq. (1) must once more become applicable. Therefore,

$$\mathrm{Re}(F(z)) = x(E,\ell,z) \tag{10}$$

and

$$\mathrm{Im}(F(z)) = \frac{2\mu}{\hbar^2}\, \mathcal{V}_1(E,\ell,z) \equiv y(E,\ell,z) \quad . \tag{11}$$

Now we can rewrite F as

$$F(E,\ell,z) = x(E,\ell,z) + iy\,(E,\ell,z) \tag{12}$$

and recall that at z_c,

$$F(E,\ell,z_c) = 0 \quad .$$

To simplify our calculations, let us expand z_c in terms of r_c.

$$z_c = r_c + z_1 = r_c + r_1 + is_1 \tag{13}$$

Eq. (5) can now be expanded in a Taylor series around r_c, thus

$$F(z_c) = F(r_c) + \left|\frac{dF}{dz}\right|_{r_c} (z_c - r_c)$$

and

$$-F(r_c) = \left(\frac{dF}{dz}\right)_{r_c} (z_c - r_c)$$

Since $x(r_c)=0$, therefore, $F(r_c)=iy(r_c)$, and we obtain

$$-iy_c = \left|\frac{\partial x}{\partial R} + i\frac{\partial y}{\partial R}\right|_{r_c} (r_1 + is_1)$$

$$r_1 + is_1 = -\frac{iy_c\left(\frac{\partial x}{\partial R}\right)_{r_c} + \left(\frac{\partial y}{\partial R}\right)_{r_c} y_c}{\left[\left(\frac{\partial x}{\partial R}\right)^2_{r_c} + \left(\frac{\partial y}{\partial R}\right)^2_{r_c}\right]} \tag{14}$$

Collecting the real and imaginary component separately, we get

$$r_1 = -y_c \left(\frac{\partial y}{\partial R}\right)_c \left[\left(\frac{\partial x}{\partial R}\right)_c^2 + \left(\frac{\partial y}{\partial R}\right)_c^2\right]^{-1} \tag{15}$$

$$s_1 = -y_c \left(\frac{\partial x}{\partial R}\right)_c \left[\left(\frac{\partial x}{\partial R}\right)_c^2 + \left(\frac{\partial y}{\partial R}\right)_c^2\right]^{-1} . \tag{16}$$

The subscript c refers to the value at r_c.

Having found z_c in terms of the functions x and y and their derivatives, and thus indirectly also in terms of V and V_1, we turn again to Eq. (4). We see that the major difficulty with the integration is the non-analyticity of the integrand $(F)^{\frac{1}{2}}$ on the complex plane V. Its multivalueness can be avoided only by taking appropriate branch cuts in the complex plane. Since Eq. (5) has in general more than one root, these branch cuts can be made by just joining these roots together on the complex plane V. This means that if we choose for our z_c that root having the largest $Re(z_c)$, we can safely take the following path of integration which we know will not cross any branch cuts,

$$z_c \longrightarrow r_c + r_1 \longrightarrow r_c \longrightarrow \infty \longrightarrow \infty + i\infty \tag{17}$$

Thus,

$$\eta(\ell) = \int_{z_c}^{r_c+r_1} \{F(z)^{\frac{1}{2}}-k\}dz + \int_{r_c+r_1}^{r_c} \{F(z)^{\frac{1}{2}}-k\}dz + \int_{r_c}^{\infty} \{F(z)^{\frac{1}{2}}-k\}dz$$

$$+ \int_{\infty}^{\infty+j\infty} \{F(z)^{\frac{1}{2}}-k\}dz - kz_c + \tfrac{1}{2}\pi(\ell+\tfrac{1}{2}) \qquad (18)$$

The first two integrals can be solved by expanding F(z) around r_c, for example,

$$\int_{z_c}^{r_c+r_1} \{F(z)^{\frac{1}{2}}-k\}dz = \int_{r_c+r_1+is_1}^{r_c+r_1} \{[x(r_c) + iy(r_c)]^{\frac{1}{2}} - k\}dz$$

$$= (iy_c)^{\frac{1}{2}}(-is_1) + iks_1 + O(z_1^2, y_c^{\frac{1}{2}})$$

The last integral is zero because at $R=\infty$, $(x+iy)^{\frac{1}{2}} - k = 0$. Therefore,

$$\eta(\ell) = \int_{r_c}^{\infty} \{[x(R)+iy(R)]^{\frac{1}{2}}-k\}dR - kr_c + \tfrac{1}{2}\pi(\ell+\tfrac{1}{2}) - (r_1+is_1)(iy_c)^{\frac{1}{2}} + O(z_1^2, y_c^{\frac{1}{2}})$$

(19)

In order to separate out the real and imaginary component of $\eta(\ell)$, we need to work on the bracket within the integral. Using the general definition of a complex number, we can rewrite $(x + iy)$ as

$$(x+iy) = (x^2+y^2)^{\frac{1}{2}} \frac{x}{(x^2+y^2)^{\frac{1}{2}}} + i \frac{y}{(x^2+y^2)^{\frac{1}{2}}}$$

$$= (x^2+y^2)^{\frac{1}{2}} (\cos\theta + i \sin\theta) = (x^2+y^2)^{\frac{1}{2}} e^{i\theta}$$

Thus the expression of interest $(x+iy)^{\frac{1}{2}}$ becomes

$$(x+iy)^{\frac{1}{2}} = (x^2+y^2)^{\frac{1}{4}} e^{i\,\theta/2} = (x^2+y^2)^{\frac{1}{4}} (\cos\theta/2 + i \sin\theta/2)$$

Since

$$\cos\theta/2 = \{\tfrac{1}{2}(1 + \cos\theta)\}^{\frac{1}{2}}$$

$$= \left\{\tfrac{1}{2}\left[1 + \frac{1}{\left(1 + \frac{y^2}{x^2}\right)^{\frac{1}{2}}}\right]\right\}^{\frac{1}{2}}$$

and

$$\sin\theta/2 = \{\tfrac{1}{2}(1-\cos\theta)\}^{\frac{1}{2}}$$

$$= \left\{\tfrac{1}{2}\left[1 - \frac{1}{\left(1 + \frac{y^2}{x^2}\right)^{\frac{1}{2}}}\right]\right\}^{\frac{1}{2}}$$

Therefore

$$(x+iy)^{\frac{1}{2}} = (x^2+y^2)^{\frac{1}{4}} \left\{ \left[\frac{1}{2}\left(1 + \frac{1}{\left(1+\frac{y^2}{x^2}\right)^{\frac{1}{2}}}\right)\right]^{\frac{1}{2}} + i\left[\frac{1}{2}\left(1 - \frac{1}{\left(1+\frac{y^2}{x^2}\right)^{\frac{1}{2}}}\right)\right]^{\frac{1}{2}} \right\}$$

$$= x^{\frac{1}{2}}\left(1+\frac{y^2}{x^2}\right)^{\frac{1}{4}} \left\{ \left[\frac{1}{2}\left(1 + \frac{1}{\left(1+\frac{y^2}{x^2}\right)^{\frac{1}{2}}}\right)\right]^{\frac{1}{2}} + i\left[\frac{1}{2}\left(1 - \frac{1}{\left(1+\frac{y^2}{x^2}\right)^{\frac{1}{2}}}\right)\right]^{\frac{1}{2}} \right\}$$

Let

$$W(E,\ell,R) = \left\{ \frac{1}{2}\left[\left(1+\frac{y^2}{x^2}\right)^{\frac{1}{2}} - 1\right]\right\}^{\frac{1}{2}} \tag{20}$$

using this and Eq. (15) and (16), the real and imaginary part of the complex phase shift can be written as

$$\mathrm{Re}[\eta(\ell)] + \int_{r_c}^{\infty} [x^{\frac{1}{2}}(W^2+1)^{\frac{1}{4}} - k]\, dR - kr_c + \tfrac{1}{2}\pi\,(\ell+\tfrac{1}{2}) \tag{21}$$

$$+2(y_c)^{3/2}\left\{\left(\frac{\partial y}{\partial R} - \frac{\partial x}{\partial R}\right)\left[\left(\frac{\partial x}{\partial R}\right)^2 + \left(\frac{\partial y}{\partial R}\right)^2\right]^{\frac{1}{2}}\right\}_c + \cdots$$

$$\mathrm{Im}[\eta(\ell)] = \int_{r_c}^{\infty} \chi^{\frac{1}{2}} W \, dR + 2(\tfrac{1}{2}y_c)^{3/2} \left\{ \left(\frac{\partial y}{\partial R} + \frac{\partial x}{\partial R}\right) \left[\left(\frac{\partial x}{\partial R}\right)^2 + \left(\frac{\partial y}{\partial R}\right)^2 \right]^{\frac{1}{2}} \right\}_c + \ldots \quad (22)$$

We thus far have yet to impose any assumptions on the relative magnitude of V and V_1. We see from Eq. (20), (21) and (22) that if we assume $V \gg V_1$, then (after some amount of tedious manipulations) we can obtain the familiar first order semi-classical expressions,

$$\mathrm{Re}[\eta(\ell)] = \hbar^{-1} \int_{r_c}^{\infty} \left\{ \left[2\mu(E-V) - \frac{\hbar^2(\ell+\frac{1}{2})^2}{R^2} \right]^{\frac{1}{2}} - k \right\} dR - kr_c + \tfrac{1}{2}\pi(\ell+\tfrac{1}{2}) + \ldots \quad (23)$$

$$\mathrm{Im}[\eta(\ell)] = (\tfrac{1}{2}\mu)^{\frac{1}{2}} \hbar^{-1} \int_{r_c}^{\infty} \frac{V_1 \, dR}{\left\{ E - V - \dfrac{\hbar^2(\ell+\frac{1}{2})^2}{2\mu R^2} \right\}^{\frac{1}{2}}} + \ldots \quad (24)$$

We see that Eq. (23) and (24) are fairly straight forward computationally. Unless otherwise stated, they are therefore used in all our calculations. Their general validity has been discussed and established in several publications[3]; we will deal with this question again when we look into specific chemical systems.

C. Cross Sections and Phase Shifts

Phase shifts by themselves cannot be measured in the laboratory. Their access to the real world can only be gained through a variety of experimental observables in which they play either a direct or indirect role. Since phase shifts contain much valuable information about the nature of the potential which brought them into being, it give special attention to those experimental quantities which provide these phase shifts with the most room to express themselves. Two such quantities are the total and differential cross sections; we will see how they are explicitly related to the phase shifts in this section.

The differential cross section, $\sigma(\Theta)$, for elastic scattering from a single target molecule into an angle Θ is defined as

$$\sigma(\Theta)\, d\omega = \frac{\text{number of particles scattered into solid angle } d\omega \text{ per second}}{\text{incident flux}} \tag{25}$$

where for a spherical potential (for which all the particles that get within the same separation will all scatter to the same angle), the solid angle $d\omega$ is simply $2\pi(\sin\Theta)d\Theta$.

$d\omega$ is also equal to dA/R^2, where R is the distance from the scattering center; Eq. (25) can therefore be written more simply as

$$\sigma(\theta) = \frac{(\text{outward flux})\ (R^2)}{\text{incident flux}} \tag{26}$$

Classically, the flux, or current $\vec{J}$, is related to the particle density ρ by

$$-\frac{\partial\rho}{\partial t} = \nabla \cdot \vec{J} \tag{27}$$

Quantum mechanically, $\rho = |\psi|^2$, and it is related to $\vec{J}$ via the Schrodinger equation for a free particle

$$-\frac{\hbar^2}{2m} \nabla^2\psi = -\frac{\hbar}{i}\frac{\partial\psi}{\partial t} \tag{28}$$

Since

$$\frac{\partial}{\partial t}|\psi|^2 = \psi^* \frac{\partial\psi}{\partial t} + \frac{\partial\psi^*}{\partial t}\psi$$

therefore, substituting from Eq. (28)

$$-\nabla\cdot\vec{J} = -\frac{i\hbar}{2m}\left[\psi^* \nabla\cdot\nabla\psi - \psi\nabla\cdot\nabla\psi^*\right]$$

$$\vec{J} = -\frac{i\hbar}{2m}(\psi^*\nabla\psi - \psi\nabla\psi^*) \tag{29}$$

For the most general case of a spherical wave propagating outward,

$$\psi_{out}(R,\theta,\psi) = e^{ikz} + \frac{f(\theta)}{R} e^{ikR} \; ; \quad k = \frac{mv}{\hbar} \tag{30}$$

Putting (30) into (29) gives

$$\vec{J}_{out} = |f(\theta)|^2 \frac{v}{R^2} \tag{31}$$

We will always, for simplicity, assume a plane wave for the incident beam, thus

$$\psi_{in} = e^{ikz} \tag{32}$$

and the resulting current is

$$\vec{J}_{in} = v \tag{33}$$

The differential cross section from Eq. (26), (31) and (33) becomes,

$$\sigma(\theta) = |f(\theta)|^2 \tag{34}$$

And the total cross section, which is a measure of the probability of particles being scattered from the beam, i.e. of its attenuation, is just the integral of $\sigma(\theta)$.

$$\begin{aligned} \sigma_{tot} &= \int_0^{2\pi}\int_0^{\pi} \sigma(\theta)\, d\theta \sin\theta\, d\phi \\ &= 2\pi \int_0^{\pi} |f(\theta)|^2 \sin\theta\, d\theta \end{aligned} \tag{35}$$

It now remains for us to determine $f(\theta)$, and see how it relates to the phase shifts. To do this, we go back to expression (30) for Ψ, and write $f(\theta)$ as

$$f(\theta) = \frac{R}{e^{ikR}} \left[\lim_{R\to\infty} \psi - e^{ikz}\right] \tag{36}$$

Without belaboring the point, we will just recognize that e^{ikz} can be expanded in terms of the Legendre polynomials $P_\ell(\cos\ )$, thus

$$e^{ikz} = \sum_\ell \frac{(2\ell+1)(i)^\ell}{2ikR}\left[e^{i(kR-\frac{\ell\pi}{2})} - e^{-i(kR-\frac{\ell\pi}{2})}\right] P_\ell(\cos\theta) \tag{37}$$

The first term is Eq. (37) represents a spherical wave propagating outward along R, and the second term a spherical wave propagating inward. By causality, the existence of the scattering center would change only the outgoing wave, and we can express this disturbance by incorporating into the first term of Eq. (37) some function g_ℓ, which depends only on ℓ.

Therefore,

$$\lim_{R\to\infty} \psi(R,\theta,\phi) = \sum_\ell \frac{(2\ell+1)(i)^\ell}{2ikR}\left\{g_\ell\, e^{i(kR-\frac{\ell\pi}{2})} - e^{-i(kR-\frac{\ell\pi}{2})}\right\} P_\ell(\cos\theta) \tag{37a}$$

and from (36)

$$f(\theta) = Re^{-ikR}\sum_\ell \frac{(2\ell+1)(i)^\ell}{2ikR}(g_\ell-1)\, e^{i(kR-\frac{\ell\pi}{2})} P_\ell(\cos\theta) \tag{38}$$

$$= \sum_\ell \frac{(2\ell+1)(i)^\ell}{2ik}(g_\ell-1)(e^{-i\pi/2})^\ell P_\ell = \frac{1}{k}\sum_\ell (2\ell+1)\frac{g_\ell-1}{2i} P_\ell(\cos\theta)$$

It has been argued previously that the only effect a potential at the scattering center has on the outgoing wave at large R is the introduction of a phase shift, we can therefore identify g_l in (38) as

$$g_\ell = e^{2i\eta_\ell} \tag{39}$$

where η_ℓ is our beloved phase shift. The factor 2 in the exponential can be understood by recognizing that since the wave is pulled in by the amount η_ℓ, this would cause the phase difference between the outgoing and incoming wave to be $2\eta_\ell$ differen[illegible] what it would be with no potential present.

Finally, from (34)

$$\sigma(\theta) = \lambda\!\!\!^{-2}\left|\sum_\ell (2\ell+1)\sin\eta_\ell\, e^{i\eta_\ell} P_\ell(\cos\theta)\right|^2; \quad \lambda\!\!\!^{-} = \frac{1}{k} \quad . \tag{40}$$

We shall invest more physical insights into Eq. (40) later on. For now, suffice it to observe that $\sigma(\theta)$ cannot be decomposed into partial waves because of interference between different ℓ values. Such interferences, when visible in an actual differential cross section measurement, constitute a rich source of information about the potential at work. This is in sharp contrast to σ_{tot}, the total cross section as defined in Eq. (35); σ_{tot} has effectively buried this valuable information by

virtue of its integrated nature. As all the interferences have vanished upon integration over the full solid angle, σ_{tot} can be written as a sum over ℓ.

$$\sigma_{tot} = 2\pi\lambda\!\!\!^{-2}\sum_{\ell}(2\ell+1)^2 \sin^2\eta_\ell \int_{-1}^{1}\left[P_\ell(\cos\theta)\right]^2 \sin\theta d\theta$$

$$= 2\pi\lambda\!\!\!^{-2}\sum_{\ell}(2\ell+1)^2\sin^2\eta_\ell \frac{2}{2\ell+1} = 4\pi\lambda\!\!\!^{-2}\sum_{\ell}(2\ell+1)\sin^2\eta_\ell \tag{41}$$

The total cross section is of course the sum of the total elastic cross section plus the total inelastic cross section. Eq. (41) as it stands however gives no clue as to the relative contribution of each. We therefore also desire explicit expressions for the elastic as well as the inelastic cross sections This is accomplished by integrating over the appropriate currents.

For the elastic case, the wave function is just the scattered wave given by Eq. (30); therefore

$$\sigma_{tot}^{ELAS} = \frac{1}{V}\oint\!\!\oint \vec{J}_{sc}\cdot\vec{dS} = \frac{\hbar}{2miV}\iint\left\{\psi_{sc}^{*}\frac{\partial\psi_{sc}}{\partial R} - \frac{i\psi_{sc}^{*}}{\partial R}\psi_{sc}\right\}R^2\, d\Omega \tag{42}$$

where

$$\psi_{sc} = \lim_{R\to\infty}\left[\psi(R)-e^{ikz}\right] = \sum_{\ell}(\partial\ell+1)i^{\ell}\frac{g_{\ell-1}}{2i}\frac{e^{i(kR-\frac{\ell\pi}{2})}}{kR}$$

For inelastic scattering, on the other hand, the cross section depends on the number of particles absorbed from the beam per second, thus

$$\sigma_{TOT}^{INELAS} = \frac{1}{V} N_{abs}$$

where the net inward flux is

$$N_{abs} = -\oiint \vec{J} \cdot \vec{dS} = -\frac{\hbar}{2mi} \iint \left\{ \psi^* \frac{\partial \psi}{\partial R} - \frac{\partial \psi^*}{\partial R} \psi \right\} R^2 d\Omega \tag{43}$$

and ψ is given by Eq. (37a).

Some straight forward algebraic manipulations yield

$$\sigma_{TOT}^{ELAS} = \pi \lambda\!\!\!^{-2} \sum_{\ell} (2\ell+1) |1-g_\ell|^2 \tag{44}$$

$$\sigma_{TOT}^{INELAS} \quad \pi \lambda\!\!\!^{-} \sum_{\ell} (2\ell+1) \{1-|g_\ell|^2\} \tag{45}$$

We are especially interested in σ_{TOT}^{INELAS} which, in terms of the phase shifts, is

$$\sigma_{TOT}^{INELAS} = \pi\lambda\!\!\!^{-2} \sum_{\ell} (2\ell+1) \left\{ 1 - e^{-4\,Im[\eta_\ell]} \right\} \tag{46}$$

Letting

$$P_\ell = 1 - e^{-4\,Im[\eta_\ell]} \tag{47}$$

thus

$$\sigma_{TOT}^{INELAS} = \pi\lambda\!\!\!^{-2} \sum_{\ell} (2\ell+1) P_\ell \tag{48}$$

We see that σ_{TOT}^{INELAS} is now in a form very similar to its classical counterpart. The latter is given as

$$\sigma_{TOT}^{INELAS,CLASS.} = 2\pi \int_0^\infty db\; b\; P_b^c \tag{49}$$

where

$$P_b^c = 1 - e^{-2\int_{R_c} dR \frac{\Gamma(R)}{\hbar V_b(R)}}$$

≡ classical probability of ionization and $V_b(R)$ is the radial velocity defined by

$$V_b(R) = \left\{ \frac{2\left[E - V(R) - \frac{\hbar^2 \ell^2}{2\mu R^2}\right]}{\mu} \right\}^{\frac{1}{2}}$$

We can indeed establish the link between Eq. (48) and (49) by making the usual semiclassical substitutions for ℓ and summation with respect to it.

$$\begin{aligned} \lambda\!\!\!^{-}(\ell+\tfrac{1}{2}) &\longrightarrow b \\ \Sigma_\ell &\longrightarrow \int db \end{aligned} \tag{50}$$

Eq. 48 therefore becomes

$$\sigma_{TOT}^{INELAS} = \pi \lambda\!\!\!^{-2} \int_0^\infty \frac{2b}{\lambda\!\!\!^{-}} \left\{1 - \ell^{-4 I_m[\eta_b]}\right\} db = 2\pi \int_0^\infty b db \left\{1 - \ell^{-4 I_m[\eta_b]}\right\}$$

As a double check, we see that since

$$\mathrm{Im}[\eta_b] = \frac{1}{2}\int_{R_c}^{\infty} dR\, \frac{\Gamma(R)}{\hbar V_b(R)}$$

this can be compared with Eq. (24), and we find

$$\frac{\Gamma}{2} = V_I$$

just as we had defined it to be.

We should note that the semiclassical substitutions Eq. (50) are most valid if there are many partial waves contributing to the scattering and thus to the summation in Eq. (48). In the case of V_I being significant only at small R and has in addition a sharp fall-off, the number of non-zero $\mathrm{Im}(\eta_l)$ would accordingly be quite small, so Eq. (48) must then be used instead of (49).

D. Actual Procedure of Data Analysis

Eq. (40),(44) and (46) constitute the theoretical backbone for the analysis of data that can be obtained from molecular beam scattering experiments. We wish to briefly outline the procedure we follow in arriving at a particular V^{opt} from differential cross section measurements.

We start off by designating the (assumed available) set of experimental differential cross sections as a function of the collision by $\sigma^{exp}(\theta,E)$. To generate the corresponding $\sigma^{theo}(\theta,E)$, we need to have to have the following information on

(i) The conditions of the beams: e.g. are they supersonic? If so, of what Mach number? The temperature of the beams; the width of the beams; the angle at which they cross, etc.

(ii) The sensitivity of the detection system: e.g. what is the angular resolution of the detector as a function of angles (what is the solid angle subtended by the detector slit with respect to the collision center?), etc.

(iii) How should V and V_1 be parameterized: if different functions are used for different parts of the potential, how do we ensure analytic continuity for all the joining points? etc.

(iv) Whereabout does ionization become likely: how far can the influence of V_1 be felt?

Areas (i) and (ii) have been quite extensively discussed in the literature, and therefore need not be dwelled upon here again. Areas (iii) and (iv) are intimately related, and require further discussion.

It must be confessed that one of the major problems one faces in analysing the elastic differential cross section for these metastable rare gass interactions is that it is difficult at times to assess the relative role played by V and V_1 at various angles. Our assumption (and indeed our hope) is that V_1 is small compared to V; moreover, V_1 is very limited in range. We infer this from knowing the total reaction cross section. Thus, in the differential cross section, V would

dominate, or rather predominate, at small angles (which correspond to large impact parameters), and conversely, V_1 at large angles (small impact parameters), and conversely, V_1 at large angles (small impact parameters). Trusting that we are not greatly misguided, we can then assume a sort of lets-kill-two-birds-with-one-stone posture when we analyse our measured $\sigma(\theta,E)$.

In many cases, while we have been fortunate in that the small angles scattering do indeed provide an unobstructed view of V, thus enabling us to extract information about the features of the potential well, as well as its long range part, we would still run into problems when we step into the region of the repulsive wall of V. The reason is that this is where V and V_1 compete for attention, so that if we only have the differential cross section at one energy, we can say very little about the shape of V_1 with confidence. It is only when $\sigma(\theta,E)$ is available for several energies, and we have been able to find a consistent set of V and V_1 which agrees with all of them, that we become more confident of our theoretical model potential. But even then, the best we can say is that the V and V_1 obtained are accurate to the extent that they are preset to assume certain functional forms. In other words, we cannot be sure that if different functions had been assigned to V and V_1, we might not get equally good fits to our data. We will address this question again in Chapter III.

E. The Ionic Potential from V and V_1

We seek to show in this section that if our differential cross section measurements yield a consistent set of V and V_1, then V^+, the ionic potential,

can also be determined if the relative cross sections for associative ionization and Penning ionization are known.

Expressions for associative and Penning ionization cross sections can be obtained using probability arguments along those first propounded by Miller.[4] Thus the probability P(R) of ionization (be it Penning or associative) at a certain distance R along the trajectory takes the following forms:

P(R)dR = (probability that ionization has not taken place up to the point R) (the rate of ionization at R) (time spent in the interval R, R-dR)

We note that the first factor is there because, as pointed out before, ionization is an irreversible process. For this reason, the first factor is also called the survival factor.

Let us now define $P_{PI}^{in}(R)$ and $P_{PI}^{out}(R)$, $P_{AI}^{in}(R)$ and $P_{AI}^{out}(R)$ to be the probability at R that Penning ionization (PI) or associative ionization (AI) takes place when the atoms are approaching or separating from each other. Given the aforementioned basic definition of ionization probability, we can immediately write down the following system of equations:

$$p_{PI}^{in}(R)dR = \left[1 - \int_R^\infty p_{TI}^{in}(R)dR\right] A_{PI}(R)dR$$

$$p_{AI}^{in}(R)dR = \left[1 - \int_R^\infty p_{TI}^{in}(R)dR\right] A_{AI}(R)dR$$

$$p_{PI}^{out}(R)dR = \left[1 - \int_{R_o}^\infty p_{TI}^{in}(R)dR - \int_{R_o}^R p_{TI}^{out}(R)\ dR\right] \times A_{pI}(R)dR \tag{51}$$

$$p_{AI}^{out}(R)dR = \left[1 - \int_{R_o}^\infty p_{TI}^{in}(R)dR - \int_{R_o}^R p_{TI}^{out}(R)\ dR\right] \times A_{AI}(R)dR$$

where

$p_{TI}^{out/in}(R)$ are total probabilities

$$p_{TI}^{out/in} = p_{PI}^{out/in}(R) + p_{AI}^{out/in}(R)$$

$$A_{PI/AI}(R)dR = \left[\frac{\Gamma_{PI/AI}(R)}{\hbar}\right] \left[\frac{dR}{V_b(R)}\right]$$

$\equiv$ (rate of ionization) (time spent in interal R, R+ dR)

R_o is the classical turning point defined by

$$V_b(R_o) = V_o \left[1 - \frac{V(R)}{E_c} - \frac{b^2}{R_o^2}\right]^{\frac{1}{2}} = 0$$

$$E_c = \tfrac{1}{2}\mu V_o^2 \equiv \text{relative kinetic energy}$$

$V(R)$ is the real part of the entrance channel potential.

The above system of equations (51) can be solve by converting them to appropriate differential equations. For example,

$$P_{AI}^{in}(R)dR = \left[1 - \int_R^\infty P_{TI}^{in}\, dR\right] A_{AI}(R)dR \tag{52}$$

$$\therefore \frac{dP^{in}}{dR} = \frac{dA}{dR}\left[1 - \int_R^\infty P_{TI}^{in}\, dR\right] - A\frac{d}{dR}\int_R^\infty P_{TI}^{in}\, dR$$

$$= \frac{dA}{dR}\frac{P^{in}}{A} + P^{in}A$$

$$\therefore \int_R^\infty \frac{1}{P}\frac{dP}{dR} = \int_R^\infty \frac{1}{A}\frac{dA}{dR} + \int_R^\infty A\, dR$$

$$\therefore \ln P^{in}(\infty) - \ln P^{in}(R) = \ln A(\infty) - \ln A(R) + \int_R^\infty A\, dR$$

Since

$$p^{in}(\infty) = A(\infty) = 0$$

$$\therefore \ln \frac{p^{in}(R)}{A(R)} = -\int_R^\infty A dR$$

$$\therefore p^{in}(R) = A^{in}(R) e^{-\int_R^\infty A dr}$$

Going back to equation (52), we see that

$$\int_R^\infty p^{in} dR = 1 - \frac{p^{in}}{A}$$

$$\therefore \int_R^\infty p^{in} dR = 1 - e^{-\int_R^\infty A \, dR}$$

p^{out} likewise can be solved, and we get

$$\frac{dp^{out}}{dR} = \frac{dA}{dR}\left[\frac{p^{out}}{A}\right] - A\,p^{out}$$

$$\therefore \quad \ln \frac{P_{out}(\infty)}{A(\infty)} - \ln \frac{p^{out}(R)}{A(R)} = -\int_R^{\infty} A\,dR$$

$$\therefore \quad \frac{p^{out}(R)}{A(R)} = \frac{p^{out}(\infty)}{A(\infty)}\, e^{\int_R^{\infty} A\,dR} \tag{53}$$

$$\therefore \quad p^{TOT} = p^{out} + p^{in}$$

$$= A(R)\left\{ e^{\int_R^{\infty} A\,dR}\, \frac{P_{out}(\infty)}{A(\infty)} + e^{-\int_R^{\infty} A\,dR} \right\}$$

To determine $\frac{P_{out}(\infty)}{A(\infty)}$, we recognize that

$P_{cut}(\infty) = A(\infty)[1 - \text{prob. of making a transition during the entire collision}]$

$$= A(\infty) \left[1 - \int_{R_0}^{\infty} P_{TOT}\, dR \right]$$

$$= A(\infty)\, e^{-2 \int_{R_0} A\, dR}$$

-- substituting back into Eq. (53), we get

$$P^{TOT} = A(R) e^{-\int_{R_0}^{\infty} A\, dR} \left\{ e^{\int_{R_0}^{R} A\, dR} + e^{-\int_{R_0}^{R} A\, dR} \right\}$$

$$= A(R)\, e^{-\int_{R_0} A dR} \left(2 \cosh \int_{R_0}^{R} A\, dR \right) \tag{54}$$

Finally, from Eq. (54), we can write down the respective total probability for Penning and associative ionization. Thus

$$P_{PI}(R) = A_{PI}(R)\, e^{-\int_{R_0}^{\infty} A_{TI}(R) dR} \left(2 \cosh \int_{R_0}^{R} A_{TI}(R)\, dR \right) \tag{55}$$

$$P_{AI}(R) = A_{AI}(R)e^{-\int_{R_0}^{\infty} A_{TI}(R)dR}\left[2\cosh\int_{R_0}^{R} A_{TI}(R)dR\right] \tag{56}$$

where

$$P_{PI/AZ}(R) = P^{in}_{PI/AI} + P^{out}_{PI/AI}$$

$$A_{TI}(R) = A_{AI}(R) + A_{PI}(R)$$

Using the classical formula for cross section, we then have

$$\sigma_{PI/AI} = 2\pi\int_0^{\infty} b\ db \int_{R_0}^{\infty} P_{PI/AI}(R)\ dR$$

Experimentally of course we can only detect A_{TI}, thus in order to put Eq. (55) and Eq. (56) to use, we need to make the following (reasonable) assumptions:

$$R_0 \leq R \leq R_{AI}\ , \quad A_{PI}(R) = 0, \quad A_{AI}(R) = A_{TI}(R)$$

$$R \geq R_{AI}\ , \quad A_{PI}(R) = A_{TI}(R)\ , \quad A_{Az}(R) = 0$$

The desired cross sections are at last found to be

$$\sigma_{AI}(V) = 4\pi \int_0^\infty bdb\ e^{-\int_{R_0}^{\infty} A_{TI}(R)dR} \sinh \int_{R_0}^{R_{AI}} A_{TI}(R)\ dR$$

$$\sigma_{PI}(V) = 4\pi \int_0^\infty bdb\ e^{-\int_{R_0}^{\infty} A_{TI}(R)dR} \left[\sinh \int_{R_0}^{\infty} A_{TI}(R)dR - \sinh \int_{R_0}^{R_{AI}} A_{TI}(R)\ dR \right]$$

The only remaining unknown is thus R_{AI}. This is where the experimental data came in. What we do is to assume a R_{AI}, calculate σ_{AI} and σ_{PI}, and compare the theoretical ratio of $\frac{\sigma_{AI}}{\sigma_{PI}}$ to its experimental counterpart. This procedure is repeated until a R_{AI} is found such that theory agrees with experiment.

However, we know also from our previous discussion that at R_{AI},

$$E_c = V^*(R_{AI}) - V^*(\infty) - V^+(R_{AI})$$

$$\tfrac{1}{2}\mu V_0^2 = [V^*(R_{AI}) - V^*(\infty)] - V^+(R_{AI})$$

Since we know the potential V^*, we can now determine $V^+(R_{AI})$.

REFERENCES - CHAPTER II

1. See for example:

   (a) A. L. Felter and K. M. Watson in Ad. in Theo. Phys. 1, p. 115 (1965).

   (b) D. A. Micha, in Molecular Scattering Calculations edited by W. H. Miller (1977).

2. J. L. J. Rosenfeld and J. Ross, J. Chem. Phys. 44, 188 (1966).

3. See for example:

   (a) R. Marriot and D. A. Micha, Phys. Rev. 180, 120 (1969).

   (b) R. E. Roberts and J. Ross, J. Chem. Phys. 52, 1464 (1970).

4. W. H. Miller J. Chem. Phys. 52, 3563 (1970).

APPENDIX

Differential cross section program for complex potentials, NELAS.

```
      PROGRAM INELAS(INPUT,OUTPUT,TAPE5=INPUT,TAPE6=OUTPUT,PUNCH,TAPE7=P
     1UNCH,PLOT,TAPE9=PLOT,TAPE10)
C*CCCCCC,M=10,ELASTIC SCATTERING FROM CH TO LA WITH  THE USE OF
C OPTICAL POTENTIAL MODEL.. SECOND MODIFIED VERSION OF FOUR SERIES
C THIS PROGRAM PLOT OUT THE CALCULATED ANG. DISTRIBUTION ON A SEMI-LOG
C PAPER AND CARRY OUT THE LEAST-SQUARE-FIT
C REQUIRES SUBROUTINE PLOTDES AND READ5N
C THIS PROGRAM IS FOR THE DETECTOR FOR MEASURING THE FLUX RATHER T
C THE FLUX DENSITY
C  ELASTIC SCATTERING CM-LAB TRANSFORMATION WITH VELOCITY AND REC.
C  AVERAGING.
      DIMENSION FE(200),FLMPI(200),THL(200),CE(200),SE(200),DI(200),
     1 JACH(200),THLE(200),CTC(200),STC(200),PHE(200),FIM(200),PI(2
     2P(200),A(20),TA(8),HK(8),FA(2)
      REAL JACH,
      COMMON /NUPAR/ FABS(100),CK(100),CV(100),COSTV(100),SINTV(100),
     1 THLC(100),C1(100),C2(100),U(100),U2(100),E(100),NV(2),GB(2),
     2 VPAR(5,2),NUAR,GAMMA,HW(8),G,NUB10
      COMMON /SYSPAR/ EI,AK,AK2,IDENT
      COMMON/DATAST/NREAD,NDATA,CHANG(200),CENT(200),ANG(200),AIN(200)
     1,THLE(200)
      COMMON/CLPLOT/CCDATA(8)
      COMMON/CLFAC/RATIO
      COMMON /PUTCOMS/ CO,ACHUTCE
      COMMON/DEPLET/NUPACAL,NNN,NCAL,LCOM,PARAM(5),ABSUR(2000),OPFUN120
     1U1,PHASE(2000),CLTURN(2000),NNGPIO,MP,SIJK
      COMMON/DERIVK(200,6),NMAX,IN,NS
      LOGICAL NCAL
      DATA EMIN,DXE1,DXE2,DXE3/0.5,0.01,0.02,0.05/
      DATA Y/.01745329/
      AAA=1.66287Z
   99 CONTINUE
      READ(5,1000)
      READ(5,1001) NV(1),NV(2),NGAM,NREAD,GB(1),GB(2),GAMMA,HW(8)
      READ(5,1002) (VPAR(I,1),I=1,5)
      READ(5,1002) (VPAR(I,2),I=1,5)
      VPAR(1,1)=SQRT(2AA/CK(1))*VPAR(1,
      VPAR(1,2)=SQRT(2AA/CK(2))*VPAR(1,2),
      READ(5,1003) DTHL,THLMIN,DTHL
      READ(5,1003) (FP(I),MP(I),I=1,8)
      G=GB(1)*GB(2)
      A=G*GP(1)*GN(2)/G
      NGAMID=NV(1)*NV(2)*NGAM
      NNNIDNNGPIO
C  CALCULATION OF NEWTON DIAGRAM WEIGHTS AND TRANSFORMATION PARAMETERS.
      CALL CHEAT
      ADID=THLMIN
      IF(NREAD.EQ.1) WRITE(7,1000)
      IF(NREAD.GT.0) CALL READIN
   97 CONTINUE
      READ(5,1001) NPAR,IDENT,NUPACAL
      IF(NPAR.LE.0) GO TO 99
  100 CONTINUE
      NPCUT=0
      READ(5,1009) (A(I),I=1,NPAR)
```

```
      IF(A(I)) 599,97,98
   98 CONTINUE
      ACHOICE=A(NPAR)
      WRITE(6,1030)
      WRITE (6,1025)
      WRITE(6,1024)
      WRITE(6,1031)NV(1),NV(2),NGAM,NREAD,GB(1),GB(2),GAMMA,NWSDB
      WRITE(6,1035) (VPAR(I),I=1,5)
      WRITE(6,1036) (VPAR(I),I=1,5)
      WRITE(6,1037)
      WRITE(6,1033) NTHL,THLMIN,DTHL
      WRITE(6,1034)
      WRITE(6,1032) (TR(I),I=1,8),(HR(I),I=1,8)
      WRITE(6,1038) (A(I),I=1,NPAR)
 1000 FORMAT(55H
 1001 FORMAT(4I5,5F10.4)
 1002 FORMAT(8F10.4)
 1031 FORMAT(5X,7F10.3)
 1034 FORMAT(5HO VVA233MVB1X4HGAMVX2HGABX2HGB7X5HGAMMA8X5HNWSDB)
 1035 FORMAT(6HOVAPAR,5F10.4)
 1036 FORMAT(6H VAPAR,5F10.4)
 1037 FORMAT(5HO0THL9XCHTHLMIN0X4HDTHL)
 1038 FORMAT(21HINPUTENTIAL PARAMETERS//(8F10.4/))
 1039 FORMAT(8F10.0)
 1040 FORMAT(16F5.0)
 1041 FORMAT(22H0RESOLUTION PARAMETERS)
 1029 FORMAT(36H0   PROGRAM ECLOP2.(M=10) WAS USED  /)
C  SETUP FOR CROSS SECTION.
      CALL PRECS(NTHL,CTC,D,A,NPAR,PRE,PIM,P1,P2,NPLOT)
      EMP=0.
      MP=0.
      DO 10 JK=1,NGRID
      IF(EMP-E(JK)) 6,7,7
    6 EMP=E(JK)
    7 CONTINUE
      IF(MP-RANG(JK)) 5,10,10
    5 MP=RANG(JK)
      MP=JK
   10 CONTINUE
      AKM=SQRT(20.7481*PMU*EMP)
      AAM=AKM*A(2)
      AKKM=EMP/A(1)
      AOM=0.2945246*GOMAKMP**6/AKKM
      LCOM=AOM/3.0011*P0.2*1
      WRITE(6,1033) AKM,AAM,AKKM,LCOM
 1033 FORMAT(   20HOAKM,AAM,AKKM,LCOM  /3P3E   4.10X,I6/)
C READ IN OPFUN , IF PARAM(1) EQ -1..
      IF(NLPACAL.EQ.0) GO TO 500
   30 READ(5,1002) (PARAM(I),I=1,5)
      IF(PARAM(1).EQ.-100.) GO TO 100
      WRITE(6,1032) (PARAM(I),I=1,5)
 1032 FORMAT(20HOVACITY PARAMETERS  ,6P5F   ,5/)
      IF(PARAM(1).EQ.-1.) READ(6,1001) NN
      IF(PARAM(1).EQ.-1.) READ(6,1031)      FUN(I),I=1,NNN)
  500 CONTINUE
```

```
 1031 FORMAT(1P6E12.3)
      CALL CHECK(IY
      IF(NCALL .EQ.0) CALL PRINT(NC,A12),PARAM)
      THLM=THLM/RY
      DTHL=DTHL/RY
      DO 11 I=1,NTHL
      FL(I)=0.
      THL(I)=THLM+(FLOAT(I)-1)*DTHL
      CT(I)=COS(THL(I))
   11 ST(I)=SIN(THL(I))
C  VELOCITY AVERAGING.
      DO 20 IJK=1,NGRID
      IIJK=IJK
      IJKMP=IJK-MP
      DO 15 I=1,NTHL
      COSA=COS(ABS(THL(I)-THLC(IJK)))
      VL=C(IJK)*COSA+SQRT(U2(IJK)-C2(IJK)*(1.-COSA**2))
      VL2=VL*VL
      UX=VL*CT(I)-CX(IJK)
      UY=VL*ST(I)-CY(IJK)
      CTC(I)=(UX*COSTV(IJK)-UY*SINTV(IJK))/U(IJK)
C  JACOBIAN APPROPRIATE FOR CM FLUX --= LAB * DENS.
      JACOB(I)=2./U(IJK)*VL2/(U2(IJK)+VL2-C2(IJK))*VL
      IF(IJKMP) 15,13,15
   13 STC(I)=ABS(UX*SINTV(IJK)-UY*COSTV(IJK))/U(IJK)
      THC(I)=ATAN2(STC(I),CTC(I))/Y
      STC(I)=STC(I)/JACOB(I)
   15 CONTINUE
      I=F(IJK)
      AKZ=20.748*RMU**1
      AK=SQRT(AKZ)
      CALL CHCSIN(THL,CTC,D,A,NPAR,RHE,FSM,P1,P2,NPLOT)
      DO 16 I=1,NTHL
      FL(IJK)=JACOB(I)*D(I)
      IF(IJKMP) 16,17,16
   17 FLMP(I)=FL(IJK)
   16 FL(I)=FL(I)+FAKG(IJK)*FL(IJK
   20 CONTINUE
      WRITE(6,1020)
 1020 FORMAT(1H0 5X3HTHL0X6HIL,RVATX5HIL,RATX5HIL,VAGXOHIL,NOMOAWTMCW
     1 4XOHISIN,RVA5XTHISIN,RA5XTHISIN,VA4XBHISIN,NOM)
      DO 25 I=1,NTHL
   25 THL(I)=THL(I)/Y
      DTHL=DTHL/Y
C  ANGULAR RESOLUTION AVERAGING AND OUTPUT.
      DO 60 I=1,NTHL
      II=I+1
      HRES=HWRES(THL(I)),TR,HR)
      RW=HRES*HRES-.42
      RW=RW/DTHL
      HR=HR*HR+1
      NMID=NR/2+1
      DTL=RW/FLOAT(NMID)
      TL=THL(I)-RW*DTL
      JJJ=MIN0(2,I)
```

```
      JJ2=MIN(I1,NTHL)
      FLRV=0.
      FLR=0.
      AN=0.
      DO 70 J=1,NR
      IF(N-NMIN) 45,50,55
   45 DO 46 JJ=JJ2,I
      J=I1-JJ
      DT=THL(J)-TL
      IF(DT) 47,47,46
   46 CONTINUE
   47 J1=J+1
   48 DT=DT/(THL(J)-THL(J1))
      FLRVI=FL(J)-(FL(J)-FL(J1))*DT
      FLRI=FLMP(J)-(FLMP(J)-FLMP(J1))*DT
      GO TO 60
   50 FLRVI=FL(1)
      FLRI=FLMP(1)
      GO TO 60
   55 DO 56 JJ=JJ2,NTHL
      J=JJ
      DT=THL(J)-TL
      IF(DT) 56,57,57
   56 CONTINUE
   57 J1=J-1
      GO TO 48
   60 CONTINUE
      TRP=TRAP(THL(I1)-TL,HRES)
      FLRV=FLRV+FLRVI*TRP
      FLR=FLR+FLRI*TRP
      AN=AN+TRP
      .LE.TL*DTL
   70 CONTINUE
      FLRV=FLRV/AN
      CF(I)=FLRV
      FLR=FLR/AN
      FCR=FLOV*STC(I)
      FCR=FLOR*STC(I)
      FCV=FL(I)*STC(I)
      FCM=FLMP(I)*STC(I)
      THLL(I)=FLRV
   80 CONTINUE
      WRITE(6,1026) (THL(I),THLL(I),I=1,NTHL)
 1026 FORMAT(10F9.3,1PE13.4))
      IF(THLL(1).LT.0.) THLL(1)=THLL(2)
      DO 110 I=1,NTHL
      IF(THLL(I).LE.0.) THLL(I)=1.E-9
  110 CONTINUE
      IF(NLOT.GT.0) GO TO 95
C  CALCULATION OF POTENTIAL.
      XX=XMIN
      DX=DXI
      NPT=(1.+XMIN)/DXI+0.4/DX2+1.5/DX3+1.
      WRITE(6,1023)
 1023 FORMAT(10HOPOTENTIAL/18X)HX7X2HV512X1HX8X1HV)
```

```
                 DO 93 I=1,NPT
                 CALL PCT(X,VS,VP)
                 R=A(I)*X
                 V=A(I)*VS
 225             WRITE(6,1024) X,VS,R,V
                 CHAR(I)=R
                 CH(I)=V
            1024 FORMAT(1H2,2(0PF10.3,1PE12.3))
                 IF(X-1.0E-4) 84,81,81
 230         81  IF(X-1.4E-0) 82,83,83
             82  DX=DX2
                 GO TO 84
             83  DX=DX3
             84  X=X+DX
 235         90  CONTINUE
                 NPLOT=NPLOT+5
             95  CONTINUE
                 CALL FLOTDIS(NTHL,ABCD,DTHL,NPT,NPLOT)
 240         1022 FORMAT(1H1)
                 THLMIN=ABCD
                 IF(NPAGAL.GT.0) GO TO 30
                 GO TO 130
             999 CALL CCEND
 245             END
REGISTER ALLOCATION
  3 REGISTERS ASSIGNED OVER THE LOOP BEGINNING AT LINE   152
```

```
      SUBROUTINE PREPW
C  PREPW-)))...,15-3233
C  CALCULATION OF GAUSSIAN QUADRATURE POINTS + WEIGHTS.
      COMMON /QUADX/ X(15),G(15),WW(15),NQ(9)
         WRITE (6,1) (NQ(I),I=1,9)
    1    FORMAT (///X,9(I1 - 9) ##,9I8)
      IF(NQ(9).EQ.0) RETURN
      X(1)=0.
      WW(1)=2
      DO 10 I=2,9
   10 NQ(I)=NQ(I-1)+NQ(I-1)
      PIN=3.1415927/1024.
      DO 20 I=1,15
      ARGP(I)=PI*(I)
      G(I)=COS(ARG)
   20 WW(I)=SIN(ARG)/X(I)**2
      RETURN
      END
```

```
      SUBROUTINE CNEWF
C $-301
C CALCULATION OF NEWTON DIAGRAM WEIGHTS AND TRANSFORMATION PARAMETERS.
C TRAPEZOIDAL RULE USED FOR ALL AVERAGING INTEGRALS.
      DIMENSION VB(100,2),GAM(5),FU(100,2),GM(5),A0(2),A1(2)
      COMMON /NCPAR/ PAD(100),CF(100),CY(100),CLSTV(100),SIGTV(100),
     1 THCC(100),C1(100),C2(100),U(100),U2(100),E(100),NV(2),GB(2),
     2 VPAR(5,2),NGAM,GAMMA,NM=10H,G,N=10
      DATA PI/3.141593/
      G1=GA(1)
      G2=GA(2)
      GFAC=1.195093E-3*G1*G2/G
C CALCULATION OF POINTS AND WEIGHTS FOR?
C ASSUMED TRIANGULAR DIST IN INTERSECTION ANGLE.
      NH=NGAM/2*1
      FNH=NH
      DO 5 K=1,NGAM
      GAM(K)=GAMMA*FLOAT(K-NH)*DIM$DB/FNH
      FG(K)=1.0
    5 IF(NM$DB.NE.0.0) FG(K)=1.0-ABS(GAM(K)-GAMMA)/NM$DB
C CHOICE OF BEAM VEL DIST, DEPENDING ON VALUE OF VPAR25,L??
      DO 33 L=1,2
      NVL=NV(L)
      IF(VPAR(5,L)) 20,15,10
C MAXWELL-BOLTZMANN OF FITTED DIST.
   10 FNH=(2*NVL-3)/5
      DO 12 I=1,NVL
      VB(I,L)=VPAR(1,L)*FLOAT(I)/FNH
   12 FU(I,L)=UDIST(VB(I,L),VPAR(1,L))
      GO TO 33
C SLOTTED DISK VEL SEL DIST.
   15 GMH=VPAR(3,L)-VPAR(2,L)
      DV=1.-VPAR(3,L)
      A0(1)=(1.+VPAR(3,L))/GMB
      A1(1)=-(1.+VPAR(2,L))/GMB
      A0(2)=-DV/GMB
      A1(2)=(1.-VPAR(2,L))/GMB
      DV=2./(DV*FLOAT(NVL-1))
      NM=1./DV+1.
      DV=DV/A0(1)
      DO 17 I=1,NVL
      R=1.+FLOAT(I-NH)*DV
      VB(I,L)=VPAR(1,L)*R
      II=1
      IF(R.GT.1.) II=2
   17 FU(I,L)=A0(II)+A1(II)/R
      GO TO 30
C NOZZLE BEAM DIST.
   20 AL1=VPAR(1,L)/SQRT(1.+(VPAR(2,L)-1.)/2.*VPAR(3,L)**2)
      VF=SQRT(VPAR(2,L)/2.)*VPAR(1,L)
      VPK=(VF+SQRT(VF**2+4.))/2.
      FNOKP=EXP((VPK-VF)**2)/VPK**2
      DV=3.33022/FLOAT(NVL-1)
      NM=NVL/2+1
      DO 22 I=1,NVL
```

```
      R=VK*FLOAT(I-NH)*DY
      VD(I,L)=BL(I)*R
   22 F3(I,L)=FRADRK*R*EXP(-(R-VR)**2)
   30 CONTINUE
      NVA=NV(1)
      NVB=NV(2)
      SUM=0.0
      IJK=0
      DO 4 K=1,NGAM
      UKK=GAM(K)*V
      CG=COS(UKK)
      SG=SIN(UKK)
      DO 4 I=1,NVA
      VI=VD(I,1)
      DO 4 J=1,NVB
      VJ=VD(J,2)
      IJK=IJK+1
      V=SQRT(VI**2+VJ**2-2.*VI*VJ*CG)
      U(IJK)=G2/G*V
      U2(IJK)=U(IJK)**2
      E(IJK)=GFAC*V**2
      FADG(IJK)=V*F0(I,1)*F0(J,2)*FG(K)
      CX(IJK)=(G1*VI+G2*VJ*CG)/G
      CY(IJK)=G2*VJ*SG/G
      CZ(IJK)=CX(IJK)**2+CY(IJK)**2
      CT(IJK)=SQRT(CZ(IJK))
      THLC(IJK)=ATAN(CY(IJK)/CX(IJK))
      COSTV(IJK)=(VI-VJ*CG)/V
      SINTV(IJK)=VJ/V*SG
    4 SUM=SUM+FADG(IJK)
      DO 5 IJK=1,NGRID
    5 FADG(IJK)=FADG(IJK)/SUM
      WRITE(6,1000)
      IJK=0
      DO 6 K=1,NGAM
      DO 6 I=1,NVA
      DO 6 J=1,NVB
      IJK=IJK+1
      THC=THLC(IJK)/Y
      WRITE(6,1001) VB(I,1),FB(I,1),VD(J,2),FB(J,2),GAM(K),FG(K),
     1 FADG(IJK),THC,E(IJK)
    6 CONTINUE
 1000 FORMAT(1H0,5X,4HVAB,8X,2HFAB,8X,2HVB,8X,2HFB,5X,5HGAMMA,8X,2HFG,6X,4HFADG,7X,3HTHC
     1 ,9X,1HE)
 1001 FORMAT(9F10.4)
      RETURN
      END
```

SUMMARY OF CHANGES MADE BY THE OPTIMIZER
  28 HOADS OF INVARIANT RLIST REMOVED FROM THE LOOP STARTING AT LINE 70

REGISTER ALLOCATION
  1 REGISTERS ASSIGNED OVER THE LOOP BEGINNING AT LINE 56

```
      SUBROUTINE ROOTEX (K,B)
C S-027
C  NEWTON METHOD FOR TURNING POINT.
      REAL K,K3Z
      KB2=K*K*B
      TKB2=KB2+KB2
      ITER=0
   10 ITER=
      CALL PUT(K,V,VP)
      K2=K*K
      X=(A-V-KB2/K2)/(TKB2/(X*K2)-VP)
      ITER=ITER+1
      IF(ABS(X-OLD).LE.1.E-6*X) GO TO 20
      IF(ITER.GT.100) GO TO 30
      GO TO 10
   20 RETURN
   30 WRITE(6,101)
  101 FORMAT (20HOITERATION HAS NOT CONVERGED)
      GO TO 20
      END
```

```
      SUBROUTINE PHECS(NTH,CT,P,A,NP,FRE,FIM,P1,P2,NPLOT)
C S-29....PHECS-3
C THIS IS A MODIFIED VERSION OF PHECS-2(S-22)
C  J=KB - PARTIAL WAVE CROSS SECTION.
      DIMENSION P1(260),CT(260),P2(260),P(260),A(20) ,FRE(260),FIM(260),
     XPPF(2000)
      COMMON /QUAD/ F1(512),XQ(512),WQ(512),NQ(9)
      COMMON /SYSPAR/ E,AK,AK2,IDENT
      COMMON /POTCONS/ C6,ACHOICE
      LOGICAL LOOD,NCAL
      REAL KK
      COMMON/DEPLET/NSPACAL,NNN,NCAL,LCOM,PARAM(5),ABSORB(2000),OPFUN(20
     100),PHASE(2000),CLTURN(2000),NGRID,MP,IJK
      PINCPI=3.1415927
C  SET UP PHASE SHIFT QUADRATURE AND POTENTIAL.
         WRITE (6,1) (NQ(I),I=1,9)
    1    FORMAT (//2X,*NQ(I ~ 9) =*,9I8)
      CALL PREPQ
      CALL PREPOT(X,V,VP,A)
      PIE=PINCPI*A(2)/2.
      RETURN
      ENTRY CHCS
      KK=E/A(1)
      AA=AK*A(2)
C  CLEAR ARRAYS
      DO 10 I=1,NTH
      P1(I)=0.
      P2(I)=1.
      FRE(I)=0.
   10 FIM(I)=0.
      AP4=AA*.7853982
      A0=-.2945243*C6*AA**6/KK
      LCO=(A0/.001)**.2+1.
      XC=0.7
      XCC=0.7
      ELCROSS =0.
      RECROSS=0.
C  ANGULAR MOMENTUM LOOP.
      DO 100 L1=1,LCO
      L=L1-1
      FL=L
C  TEST FOR IDENTICAL S70 NUCLEI.
      IF(IDENT) 13,13,12
   12 LOOD=L.GT.2*(L/2)
      IF(LOOD) GO TO 64
   13 B=(FL+.5)/AA
   15 IF(NPLOT.GT.0.AND.NGRID.EQ.1) GO TO 110
      CALL RCOT(XC,KK,B)
      CO=AP4*XC
C  GAUSS-HEHLER QUADRATURE LOOPS.
      IF(B.GE..125) GO TO 35
      Z=B/XC
      ETAMS =AA*(B*ACOS(Z)-XC*SQRT(1.-Z**2))
      ETO=0.
      DO 30 I=1,9
```

```
      NQI=NQ(I)
      JS=512/NQI
      ETA=0.
      DO 20 JJ=1,NQI,2
      J=JS*JJ
      X=XC/XQ(J)
      CALL POT(X,V,VP)
      Z=1.-(B/X)**2
      F1(J)=SQRT(Z)*(SQRT(1.-V/(KK*Z))-1.)*NQ(J)
   20 ETA=ETA+F1(J)+F1(J+JS)
      ETA=2.*CO*ETA/FLOAT(NQI)+ETAHS
      IF(ABS(ETA-ETO).LE.1.E-3) GO TO 60
      ETO=ETA
   30 CONTINUE
      GO TO 60
   35 ETO=0.
      DO 50 I=1,9
      NQI=NQ(I)
      JS=512/NQI
      ETA=0.
      DO 40 JJ=1,NQI,2
      J=JS*JJ
      X=XC/XQ(J)
      CALL POT(X,V,VP)
      ZZ=1.0-V/KK-(B/X)**2
      IF(ABS(ZZ).LT.5.E-7) ZZ=0.
      F1(J)=X*VP*SQRT(ZZ)/(KK-V)*NQ(J)
      ETA=ETA+F1(J)+F1(J+JS)
   40 CONTINUE
      ETA=CO*ETA/FLOAT(NQI)
      IF(ABS(ETA-ETO).LE.1.E-3) GO TO 60
   50 ETO=ETA
   60 CONTINUE
      PHASE(L)=ETA
  110 IF(.NOT.NCAL) GO TO 61
C DEPLETION PROBABILITY CALCULATION LOOP
      B=SQRT(FLOAT(L*L))/AA
      CALL ROOT(XCC,KK,B)
      PAK=PINE*XCC*AK/(2.*E)
      CLTUANI(L)=XCC*A(2)
      IF(PARAM(1).GT.3.)  GO TO 63
C APPROXIMATE CALCULATION OF OPACITY FUNCTION
      CALL POT(XCC,V,VP)
      BETA=(VP-2.* B**2*KK/XCC**3)/(KK*A(2))
      GAMMA=1.
      XYZ=PARAM(2)/BETA
   44 IF(XYZ.LE.2.0) GO TO 42
      XYZ=XYZ-1.
      GAMMA=GAMMA*XYZ/(XYZ+0.5)
      GO TO 44
   42 CONTINUE
      EXPON=AK/(E*BETA)*EXP(-PAKAM(2)*(A(2) *XCC-PARAM(3)))*GAMMAR(.5)*
     1 GAMMA*GAMMAR(XYZ)/GAMMAR(XYZ+0.5)
      EXPON=EXP(-EXPON)
```

```
                OPFUN(L1)=1.-EXPON
                ABSORB(L1)=SQRT(EXPUN)
                GO TO 61
            C NUMERICAL INTEGRATION OF DEPLETION PROBABILITY CALCULATION USING
            C GAUSS-HERMITE QUADRATURE APPROXIMATION
             63 CONTINUE
                BETA=0.
                DO 65 I=1,9
                NOI=N(I)
                JS=512/NOI
                EXPUN=0.
                DO 66 JJ=1,NOI,2
                J=JS*JJ
                X=XCC/XOI(J)
                CALL POT(X,V,VP)
                F1(J)=WO(J)*R(X)              /SQRT(1.-V/KK-B**2/X**2)
             66 EXPON=EXPON+F1(J)+F1(J+JS)
                EXPUN=EXPON*PAR/FLOAT(NOI)
                IF(EXPON.GT.20.) GO TO 68
                IF(I.LE.3) GO TO 67
                IF(EXPON.LT.0.5) GO TO 73
                IF(ABS(BETA-EXPON).LE.1.E-4) GO TO 68
                GO TO 67
             73 IF(ABS(BETA-EXPON)/(EXPON+.003).LE.1.E-3) GO TO 68
             67 BETA=EXPUN
             65 CONTINUE
             68 CONTINUE
                BETA=EXP(-EXPON)
                ABSORB(L1)=BETA
                OPFUN(L1)=1.-BETA**2
             61 CONTINUE
                ETA=PHASE(L1)
                SC=SIN(ETA)
                S2=ABSORB(L1)*(SC*SC-0.5)*0.5
                SC=SC*COS(ETA)*ABSORB(L1)
                WL=(L+L1)*(1+IDENT)
                AECROSS=AECROSS+WL*OPFUN(L1)
                ELCROSS=ELCROSS+WL*(S2**2+SC**2)
                S2=S2*WL
                SC=SC*WL
             64 CONTINUE
            C   RECUR LEGENDRE FUNCTIONS.
                IF(L) 75,75,70
             70 DO 71 I=1,NTH
                PS=P2(I)
                XP=CT(I)*PS
                P2(I)=3S-P1(I)+XP-(XP-P1(I))/FL
             71 P1(I)=PS
             75 CONTINUE
                IF(IDENT) 77,77,76
             76 IF(LODD) GO TO 100
            C   AUGMENT REAL AND IMAGINARY PARTS OF SCATTERING AMPLITUDE.
             77 DO 80 I=1,NTH
                FRE(I)=FRE(I)+SC*P2(I)
             80 FIM(I)=FIM(I)+S2*P2(I)
```

```
      100 CONTINUE
        C CALCULATE DIFFERENTIAL CROSS SECTION.
            DO 111 I=1,NTH
      111 P(I)=(FRE(I)**2+FIM(I)**2)/AK2
            RECROSS=RECROSS*PI4OPI/AK2
            ELCROSS=ELCROSS*PI4OPI/AK2*4.
            WRITE(6,1041) RECROSS,ELCROSS ,E
     1041 FORMAT(38HOREACTIVE AND ELASTIC CROSS SECTION, E  /1P3E13.4)
            NUT=300
            IF(LCOM.LT.NUT) NUT=LCOM
            IF(MP.NE.IJK) RETURN
            IF(NPLOT.GT.0) GO TO  120
            WRITE(6,1042)
     1042 FORMAT(14H0 PHASE SHIFTS  /)
            WRITE(6,1040) (I,PHASE(I),I=1,NUT)
     1040 FORMAT(10(I4,OPF8.3))
      120 CONTINUE
            IF(NCALL.NE.1) WRITE(6,1045) (I,OPFUN(I),CLTURN(I),I=1,NUT)
     1045 FORMAT(5(I4,OPF8.5,F7.3))
            RETURN
            END

REGISTER ALLOCATION
  1 REGISTERS ASSIGNED OVER THE LOOP BEGINNING AT LINE    26
  3 REGISTERS ASSIGNED OVER THE LOOP BEGINNING AT LINE   154
  2 REGISTERS ASSIGNED OVER THE LOOP BEGINNING AT LINE   163
  1 REGISTERS ASSIGNED OVER THE LOOP BEGINNING AT LINE   168
```

```
      FUNCTION PREWR(XC,R,P)
C PREWR-3....(S-053)
      DIMENSION A(9)
      LOGICAL SWITCH
      PREWR=0.7
      IF(A(1).LT.4.) RETURN
      C1=R*A(2)
      C2=A(3)/R
      IF(A(1).EQ.4.) GO TO 10
      IF(A(1).EQ.6.) GO TO 10
      C3=A(4)
      C5=A(5)*P
      SWITCH=.TRUE.
      RETURN
   10 SWITCH =.FALSE.
      RETURN
      ENTRY WR
      X=C1*(XC-C2)
      IF(SWITCH) GO TO 5
      IF(X.GT.30.) GO TO 6
      PREWR=EXP(-X)
      RETURN
    5 C4=C3+C5*XC
      IF(ABS(X).GT.30.) GO TO 1
      PREWR=C4/(1.+EXP(X))
      RETURN
    1 IF(X.GT.0.) GO TO 6
    2 PREWR=C4
      RETURN
    6 PREWR=0.
      RETURN
      END
```

```
      FUNCTION GAMMAR(X)
C S-25
      IF(X.GT.1.) GO TO 2
      Z=X
    1 IF(Z.GT.0.) GO TO 3
      Z=Z+1.
      GO TO 1
    2 Z=X-1.
    3 T1=Z+0.5
      TZG=T1+5.
      T1=TZG**T1
      T1=EXP(-TZG)*T1*2.50662827465
      GAMZ=T1*(1.+  76.18009173/(Z+1.)-86.50532033/(Z+2.)+24.01409822/
     1 (Z+3.)-1.231739516/(Z+4.)+0.120858003E-2/(Z+5.)-0.536382E-5/(Z+6.
     2))
      IF(X.GT.1.) GO TO 5
    4 GAMZ=GAMZ/Z
      ADZ=ABS(Z-X)
      IF(ADZ.LT.0.5) GO TO 5
      Z=Z-1.
      GO TO 4
    5 GAMMAR=GAMZ
      RETURN
      END
```

```
      SUBROUTINE SPLINE(XS,A1,A2,A3,A4,DX)
C S-015
C NEW VERSION OF INTERPOLATION FUNCTIONAL EVALUATION
C THIS PROGRAM SHOULD BE USED WITH  NEW VERSION OF PREPOT SUCH AS S-016
      DIMENSION XS(4)
      A1=XS(1)
      A2=(XS(2)-XS(1))/DX
      A3=(A2-XS(3))/DX
      A4=(XS(4)-A2-A3*DX)/DX**2
      RETURN
      END
```

```
      FUNCTION UDIST(U,PAR)
C S-002
C  PARAMETRIC FORM FOR VELOCITY DISTRIBUTIONS.
      DIMENSION PAR(5)
      R=U/PAR(1)
      IF(R.GT.1.0) GO TO 10
      A=PAR(2)
      B=PAR(3)
   20 ALR=ALOG(R)
      UDIST=EXP(A*(ALR+(1.-EXP(B*ALR)))/B)
      RETURN
   10 A=PAR(4)
      B=PAR(5)
      GO TO 20
      END
```

```
      FUNCTION TRAP(X,H)
C S-005
C  TRAPEZOIDAL RESOLUTION FUNCTION.
      DATA H0/0.42/
      Z=ABS(X)-H0
      IF(Z) 1,1,2
    1 TRAP=1.
      GO TO 4
    2 TRAP=1.-.5*Z/(H-H0)
      IF(TRAP) 3,3,4
    3 TRAP=0.
    4 RETURN
      END
```

```
      FUNCTION HWRES(TH,T,H)
C S-OG4
C  HALF-WIDTH OF EFFECTIVE ANGULAR RESOLUTION.
      DIMENSION T(1),H(1)
      DO 10 I=1,8
      IF(H(I)) 30,30,5
    5 D=TH-T(I)
      IF(D) 20,20,10
   10 CONTINUE
      I=8
   20 HWRES=H(I)+(H(I)-H(I-1))*D/(T(I)-T(I-1))
      RETURN
   30 I=I-1
      END
```

```
      SUBROUTINE READIN
C S-21
C  SUBROUTINE FOR READING IN THE DATA FOR THE ANGULAR DISTRIBUTION
C ANGLES DO NOT HAVE TO BE IN ORDER FOR THE ORIGINAL INPUT FOR WHICH
C NEW DATA SET ARE PNCHED IN (8F10.6) FORMAT WITH NO. OF DATA CARDS
C FOR THE ORIGINAL DATA THE FORMAT IS (2F10.6) THE THE LAST CARD ANG
C SHOULD BE NEGATIVE VALUE
      COMMON/DATAST/NREAD,N,A(260),B(260),C(260),D(260),TH(260)
      COMMON/DATANEG/ALIMIT,WEIGHT
      IF(I.NREAD-1).GE.1) GO TO 100
      I=0
    1 READ(5,1042) ANG,DATAIN
      IF(ANG.LE.0.) GOTO 3
      I=I+1
      A(I)=ANG
      B(I)=DATAIN
      GOTO 1
    3 N=I
      READ (5,1042) ALIMIT,WEIGHT
      DO 20 J=1,N
      ANGMIN=1000.
      DO 50 K=1,N
      IF(A(K).GT. ANGMIN) GOTO 50
      IMIN=K
      ANGMIN=A(K)
   50 CONTINUE
      C(J)=A(IMIN)+DATAIN
      D(J)=B(IMIN)
      A(IMIN)=1000.
   20 CONTINUE
      ANGMIN=1.E+5
      ANGMAX=0.
   70 DO 73 I=1,N
      IF (D(I). GT. ANGMAX) ANGMAX=D(I)
      IF(D(I).LT.ANGMIN) ANGMIN=D(I)
   73 CONTINUE
      DK=INT(ALOG10(ANGMAX))
      FACTOR=10.**DK
   77 DO 80 I=1,N
   80 D(I)=D(I)/FACTOR
      ANGMIN=ANGMIN/FACTOR
      ANGMAX=ANGMAX/FACTOR
      RATIO=ANGMAX/ANGMIN
      IF(RATIO.GT.1.E+5) GO TO 83
      IF(RATIO.LE.1.E+4)GO TO 95
      FACTOR=1./( 10.*SQRT(10. *ANGMIN*ANGMAX))
      GO TO 85
   83 FACTOR=10./ANGMAX
   85 DO 90 I=1,N
   90 D(I)=D(I)*FACTOR
   95 CONTINUE
      WRITE(6,1040) ALIMIT,WEIGHT
      WRITE(6,1042) (C(I),D(I),I=1,N)
      WRITE(7,1042) N
      WRITE(7,1042) (C(I),D(I),I=1,N)
```

```
                WRITE(7,1042) ALIMIT,WEIGHT
                RETURN
            100 READ(5,1041) N
                 READ(5,1042) (C(I),D(I),I=1,N)
                WRITE(6,1042) (C(I),D(I),I=1,N)
                READ(5,1042) ALIMIT,WEIGHT
                WRITE(6,1040) ALIMIT,WEIGHT
           1040 FORMAT (* ALIMIT AND WEIGHT * 2F10.5/)
           1041 FORMAT(6I5)
           1042 FORMAT(4(F10.3,F10.6))
                RETURN
                END
```

```
REGISTER ALLOCATION
  1 REGISTERS ASSIGNED OVER THE LOOP BEGINNING AT LINE     39
  1 REGISTERS ASSIGNED OVER THE LOOP BEGINNING AT LINE     49
```

```
      SUBROUTINE PREPOT(X,V,VP,A)
C   PREPOT.......(S-54)
C    MODIFIED VERSION OF PREPOT.....(S-028)
C    MORSE POTENTIAL WAS ADDED
      COMMON /POTCONS/ C6,ACHOICE
      REAL N1
      DIMENSION A(20),XS(4)
      NCHOICE=IFIX(ACHOICE)
      IF(NCHOICE) 100,200,300
  100 CONTINUE
    2 BT=A(3)
      AH=A(4)
      AL=A(5)
      BTT=BT
       IF (NCHOICE.EQ.-2) BTT=A(13)
    3 ERM6=A(1)*A(2)**6
      C6=-A(6)/ERM6
          IF (NCHOICE.EQ.-3) GO TO 50
      C8=-A(7)/(ERM6*A(2)**2)
      C10=-A(8)/(ERM6*A(2)**4)
      DC6=-6.*C6
      DC8=-8.*C8
      DC10=-10.*C10
      IF(A(9).GT.0.) GO TO 5
    4 X1=0.
      X2=0.
      S1=0.
      SP12=0.
      SPPP12=0.
      IF(A(13).LE.0.)  WRITE(6,1007)
       IF(A(13). GT.0.) WRITE(6,1006)
 1007 FORMAT(25H0 MSV POTENTIAL WAS USED      /)
 1006 FORMAT(27H0 MMSV POTENTIAL WAS USED      /)
      GO TO 9
    5 X1=A(9)
      X2=1.-ALOG(1.+SQRT(1.+A(10)))/BTT
      IF(X2.LE.X1) GOTO 4
      IF(A(13).LE.0.)  WRITE(6,1002)
 1002 FORMAT(30H0ESMSV POTENTIAL WAS USED      /)
      IF(A(13).GT.0.) WRITE(6,1008)
 1008 FORMAT(28H0ESMMSV POTENTIAL WAS USED      /)
      XS(1)=ALOG(AH)+(1.-X1)*AL
      XBASE=EXP((1.-X2) *BTT)
      XS(2)=ALOG(XBASE)+ALOG(XBASE-2.)
      XS(3)=-AL
      XS(4)=-2.*(XBASE-1.)/(XBASE-2.)*BTT
      D21=X2-X1
      CALL SPLINE(XS,S1,SP12,SSPP12,SPPP12,D21)
    9 X3=1.-ALOG(1.-SQRT(1.+A(11)))/BT
      X4=AMAX1(A(12),X3+0.20)
      XS(1)=A(11)
      XBASE=EXP(INT*(1.-X3))
      XS(3)=-2.*BT*XBASE*(XBASE-1.)
      XS(2)=(C6+C8/X4**2+C10/X4**4)/X4**6
```

```
      X5(4)=1DC6*DC8/X4**2+DC10/X4**4)/X4**7
      D43=X4-X3
      CALL SPLINE(X5,S3,SP34,SSPP34,SPPP34,D43)
      WRITE(6,1003) BT,AR,AL,C6,C8,C10,X1,X2,X3,X4,S1,SP12,SPPP12,
     1 SSPP12,S3,SP34,SPPP34,SSPP34
 1000 FORMAT(1P9E13.5)
      RETURN
   50   WRITE (6,1009)
 1009     FORMAT (2X,*   MORSE POTENTIAL WAS USED*)
      RETURN
  200 CONTINUE
      WRITE(6,1003)
 1003 FORMAT(30HJOULSON POTENTIAL WAS USED      /)
C OLSON POTENTIAL
      A0=0.529177
      A1=4./(A(3)*A(1))*627.503
      A2=A(3)/A(4)
      A3=A(3)/A(5)
      C6=-A(6)/(A(2)**6*A(1))
      A4=-A(6)/(A(3)* A0)**6/A(1)
      RATIO=A(2)/(A0*A(3))
      WRITE(6,1001) A1,A2,A3,A4,C6
 1001 FORMAT (35HOPOTENTIAL PARAM.A1, A2,A3,A4,C6   /1P5E20.5/)
      RETURN
  300 CONTINUE
      IF(NCHOICE.EQ.2) GO TO 400
C L-J (N-6) POTENTIAL
      WRITE(6,1004)
 1004 FORMAT(33HOL-J (N-6) POTENTIAL WAS USED  /)
      N1=A(3)-6.
      CN=6./(A(3)-6.)
      C6=-A(3)/(A(3)-6.)
      C8=0.
      C10=0.
      RETURN
  400 CONTINUE
      WRITE(6,1005)
 1005 FORMAT(30HOPOTENTIAL BUCK-PAULY WAS USED /)
      AN1=A(3)-A(4)
      CN1=A(4)/AN1
      CP=-A(3)/AN1
      DCP=CP*A(4)
      N1=A(5)-6.
      CN=6./N1
      C6=-A(5)/N1
      DC6=C6*6.
      A3=A(3)
      A4=A(4)
      RETURN
      ENTRY POT
      IF(NCHOICE)1100,1200,1300
 1100 CONTINUE
      Y=1.-X
         IF (NCHOICE.EQ.-3)  GO TO 18
      IF(Y) 12,11,10
```

```
   11 V=0.
      VP=0.
      RETURN
   10 IF(NCHOICE.GE. -2) GO TO 21
      D2=X-X2
      IF(D2.GE.0.) GO TO 21
      D1=X-X1
      IF(D1.GT.0.) GO TO 17
   16 V=AW*EXP(AL*Y)
      VP=-AL*V
      RETURN
   17 Z=SSPP12+DL*SPPP12
      V=EXP(S1+D1*(SP12+D2*Z))
      VP=(SP12+(D1+D2)*Z+D1*D2*SPPP12)*V
      RETURN
   21 Z=EXP(BTT*Y)
      V=Z*(Z-2.)
      VP=2.*BTT*Z*(1.-Z)
      RETURN
   12 D4=X-X4
      IF(D4.GE.0.) GO TO 20
      IF((X-X3).LE.0.) GO TO 18
      D3=X-X3
   19 Z=SSPP34+D3*SPPP34
      V=S3+D3*(SP34+D4*Z)
      VP=SP34+(D3+D4)*Z+D3*D4*SPPP34
      RETURN
   18 Z=EXP(BT*Y)
      V=Z*(Z-2.)
      VP=BT*(2+Z)*(1.-Z)
      RETURN
   20 XX=X*X
      XXXX=XX*XX
      XXXXXX=XX*XXXX
      V=(C6+C8/XX+C10/XXXX)/XXXXXX
      VP=(DC6+DC8/XX+DC10/XXXX)/(X*XXXXXX)
      RETURN
 1200 CONTINUE
      XX=X
      X=RATIO*XX
      EXPON=EXP(-X)
      EXPON1=EXP(-X*A2)
      EXPON2=EXP(-X*A3)
      PAR=4.*EXPON+4.*EXPON1+EXPON2
      PAR1=4.*EXPON+4.*A2*EXPON1+A3*EXPON2
      X6=X**6
      AXX=(((X*0.2+1.)*0.25*X+1.)*X/3.+1.)**0.5+1.)*X+1.
      V=PAR*A1/X+A4*(1.-EXPON*XXX)/X6
      VP= PAR*A1/X**2-PAR1*A1/X-6.*A4*(1.-EXPON*XXX)/(X6*X)+   A4*EXPON/
     1120./X
      VP=VP*RATIO
      X=XX
      RETURN
 1300 CONTINUE
      IF(NCHOICE.EQ.2) GO TO 1400
```

```
      X6=X**6
      XN1=X**N1
      V=(CN/XN1+C6)/X6
      VP=-6.*CN/(X6*X)*(1.-1./XN1)
      RETURN
 1400 CONTINUE
      IF(X.GT.1.) GO TO 1410
      XM=1./X**A3
      XP=1./X**A4
      V=XM*CN1+XP*CP
      VP=DCP*(XM-XP)/X
      RETURN
 1410 CONTINUE
      X6=(1./X)**6
      XN1=(1./X)**N1
      V=(CN*XN1+C6)*X6
      VP=DC6*(XN1-1.)*X6/X
      RETURN
      END
```

```
      SUBROUTINE OPACITY
C OPACITY-2...(S-052)
      COMMON/DEPLET/NOPACAL,NNN,NCAL,LCOM,PARAM(5),ABSORB(2000),OPFUN(20
     100),PHASE(2),01,CLTURN(2000), NORID,MP,IIJK
      LOGICAL NCAL
      NCAL=.FALSE.
      WRITE(6,1000)
 1000 FORMAT(25H0 OPACITY-2 WAS USED       /)
      IF(NOPACAL.EQ.0) GOTO 10
      IF(PARAM(1))20,30,40
   40 IF(PARAM(1)-2.) 41,50,60
   41 LO=INT(PARAM(3))
      L1=INT(PARAM(4))
      CONST=PARAM(2)
      CONST1=CONST/(PARAM(4)-PARAM(3))
      DO 42 I=1,LCOM
      L=I-1
      IF(L.LE.LO) OPFUN(I)=CONST
      IF(L.GE.L1) OPFUN(I)=0.
      IF(L-LO)*(L-L1).LT.0) OPFUN(I)=CONST1*(PARAM(4)-FLOAT(L))
      ABSORB(I)=SQRT(1.0-OPFUN(I))
   42 CONTINUE
      IF(PARAM(2).EQ.0.) RETURN
      GO TO 80
   50 CONTINUE
      DELTAL=PARAM(4)
      DO 51 I=1,LCOM
      L=I-1
      CONST=PARAM(2)*FLOAT(L)*PARAM(5)
      ABC=(FLOAT(L)-PARAM(3))/DELTAL
      IF(ABS(ABC).LE.20.)GO TO 52
      IF(ABC.GT.0.) OPFUN(I)=0.
      IF(ABC.LT.0.)OPFUN(I)=CONST
      GO TO 53
   52 OPFUN(I)=CONST/(1.+EXP(ABC))
        IF (OPFUN(I).GT.1) OPFUN(I)=1
          IF (OPFUN(I).LT.0) OPFUN(I)=0
   53 ABSORB(I)=SQRT(1.-OPFUN(I))
   51 CONTINUE
        IF((PARAM(2)**2+PARAM(5)**2).EQ.0.) RETURN
      GO TO 80
   60 NCAL=.TRUE.
      RETURN
   10 DO 11 I=1,LCOM
      OPFUN(I)=0.
   11 ABSORB(I)=1.
      RETURN
   20 DO 21 I=1,LCOM
      IF(I.GT.NNN) GO TO 25
      ABSORB(I)=SQRT(1-OPFUN(I))
      GO TO 21
   25 OPFUN(I)=0.
      ABSORB(I)=1.
   21 CONTINUE
      GO TO 80
```

```
   30 LO=INT(PARAM(2))
      DO 31 I=1,LCOM
      L=I-1
      IF(L.LE.LO) GO TO 32
      ABSORB(I)=1.
      OPFUN(I)=0.
      GO TO 31
   32 ABSORB(I)=0.
      OPFUN(I)=1.
   31 CONTINUE
   80 JJ=300
      IF(LCOM.LT.JJ) JJ=LCOM
      WRITE(6,1001)
 1001 FORMAT( 21H0OPACITY FUNCTION      /)
      WRITE(6,1002) (I,OPFUN(I),I=1,JJ)
 1002 FORMAT(10(I5,OPF7.4))
      RETURN
      END
```

REGISTER ALLOCATION
1 REGISTERS ASSIGNED OVER THE LOOP BEGINNING AT LINE 44

```
      SUBROUTINE PLOTDIS(NTHL,THLMIN,DTHL,NPT,NPLOT)
C PLOTDIS-3 ...(S-031)
      DIMENSION SS(260),X(260),Y(260),IFET(8)
      COMMON/CCPGOL/XMIN,XMAX,YMIN,YMAX,CCXMIN,CCXMAX,CCYMIN,CCYMAX
      COMMON/CCFACT/FACTOR
      COMMON/DATAST/NREAD,N,POTX(260),POTY(260),A(260),D(260),TH(260)
       COMMON/DATAWEG /ALIMI,WEIGHT
      CCMMON/DEPLET/NGPAGEL,NNN,NCAL,LCOM,PARAM(5),ABSORB(2000),OPFUN(20
     100),PHASE(2000),CLTUPN(2000),KGRID,MP,IJK
      COMMON/DER/DER(200,6),KMAX,IN,NS
      FACTOR=1.0
      XMIN=0.$ XMAX=90. $ YMIN=-4.$ YMAX=1.
      CCXMIN=0.$CCXMAX=900.$ CCYMIN=50.$ CCYMAX=1050.
      CALL CCGRID(9,2,5,6HNOLBLS,5,10,1)
    1 IF (NREAD. EQ.0) GOTO 300
      DO 2 I=1,N
      X(I)=A(I)
      Y(I)=ALOG10(D(I))
      IF(Y(I).LT.-4.0) Y(I)=-4.
    2 CONTINUE
      CALL CCPLOT(X(1),Y(1),N,6HNOJOIN,71,1)
       ANGMAX=THLMIN+FLOAT(NTHL-1)*DTHL
      ALIMIT=ALIMI
      WRITE(6,1040) ALIMIT,WEIGHT
 1040 FORMAT(1H0,2F10.6/)
    5 DO 10 I=1,N
      IF(A(I).GT. ALIMIT) GOTO 50
      IF(A(I).GT.ANGMAX) GOTO 50
      THETA=(A(I)-THLMIN+DTHL)/DTHL+1.E-5
      JJ=INT(THETA)
      XX=THETA-1.0E-5-FLOAT(JJ)
      IF(ABS(FLOAT(JJ)-THETA).LT.2.E-5) GOTO 20
      IF(JJ.GT.NTHL) GOTO 50
      SS(I)=TH(JJ)+(TH(JJ+1)-TH(JJ))*XX
      GOTO 10
   20 SS(I)=TH(JJ)
   10 CONTINUE
   50 CONTINUE
      NNN=I -1
C CALCULATION OF THE SCALING FACTOR SCALING
      Y1=0.
      Y2=0.
      Y3=0.
      DO 60 I=1,NNN
       SQ=D(I)**WEIGHT
      Y1=Y1+SQ
      Y2=Y2+(D(I)/SS(I))*SQ
      Y3=Y3+(D(I)/SS(I))**2*SQ
   60 CONTINUE
      SCALING=Y3/Y2
      STD=(Y1-Y2**2/Y3)/Y1
      STD=SQRT(STD)
      WRITE(6,1050) SCALING,STD
 1050 FORMAT(1H0,17H SCALING FACTOR =  , 1PE12.4/21H0STANDARD DEVIATION
     1=  ,1PE12.4/)
```

```
      DO 65 I=1,NMN
      ABCD=SCALING*SS(I)
      SS(I)=ALOG10(ABCD/D(I))-1.
      IF(SS(I).GT.1.) SS(I)=1.
      IF(SS(I).LT.-4.) SS(I)=-4.
   65 CONTINUE
      CALL CCPLOT(X(1),SS(1),NMN,6HNOJOIN,45,1)
      DO 70 I=1,NTHL
      X(I)=THLMIN+FLOAT(I-1)*DTHL
      ABCD =ALOG10(TH(I)*SCALING)
      Y(I)=ABCD
      IF(ABCD.GT.1.) Y(I)=1.
      IF(ABCD.LT.-4.) Y(I)=-4.
   70 CONTINUE
      CALL CCPLOT(X(1),Y(1),NTHL,4HJOIN, 1,1)
      GO TO 315
  330 CONTINUE
      ABASE=0.
      DO 305 I=1,NTHL
      IF(TH(I).GT.ABASE) ABASE=TH(I)
  305 CONTINUE
      ABASE=ABASE*0.1
      DO 310 I=1,NTHL
      X(I)=THLMIN+FLOAT(I-1)*DTHL
      XXX=TH(I)/ABASE
      XXX=ALOG10(XXX)
      IF(XXX.LT.-4.) XXX=-4.
      Y(I)=XXX
  310 CONTINUE
      CALL CCPLOT (X(1),Y(1),NTHL,4HJOIN, 1,1)
  315 INPT=0
      DO 320 I=1,NPT
      IF((POTX(I).LE.20.).AND.(POTY(I).LE.50.))GO TO 330
      GO TO 320
  330 INPT=INPT+1
      X(INPT)=POTX(I)*5.
      Y(INPT)=POTY(I)*2.
      IF(Y(INPT).GT.1.) Y(INPT)=1.+ALOG10(Y(INPT))
      Y(INPT)=Y(INPT)-2.
  320 CONTINUE
      INP=INPT
  335 CALL CCPLOT(X(1),Y(1),INP,4HJOIN,1,1)
  350 CALL CENEXT
      RETURN
      END
```

LOAD MAP.
BLOCK ASSIGNMENTS.

BLOCK	ADDRESS	LENGTH	FILE
ACADER$	64352	13	SYSLIB
CCHELP$	64365	165	SYSLIB
CCLBL$	64552	177	SYSLIB
CCLTA$	64751	667	SYSLIB
CCMOVE$	65640	120	SYSLIB
CCNARG$	65760	6	SYSLIB
CCPACK$	65766	77	SYSLIB
CPUSY$	66065	50	SYSLIB
DATE$	66135	17	SYSLIB
ENDFIL$	66154	17	SYSLIB
HOUR$	66173	6	SYSLIB
KODER$	66201	1376	SYSLIB
KRAKER$	67577	1471	SYSLIB
LUCF$	71270	2	SYSLIB
MATHER$	71272	13	SYSLIB
PERMIN$	71305	37	SYSLIB
SIOS	71344	1277	SYSLIB
USERIO	72643	53	SYSLIB
CCFIX$	72716	35	SYSLIB
CCUNPK$	72753	7	SYSLIB
GETBA	72762	17	SYSLIB
MAKEEN$	73001	20	SYSLIB

VA	FA	VB	FB	GAMMA	FG	FABG	THC	E
13.9795	.4957	18.4080	.4949	90.0000	1.0000	.0559	52.9235	1.2801
13.9795	.4957	20.4031	1.0000	90.0000	1.0000	.1209	55.7156	1.4657
13.9795	.4957	22.3983	.4955	90.0000	1.0000	.0640	58.1586	1.6703
19.3643	1.0000	18.4080	.4949	90.0000	1.0000	.1171	50.2902	1.3775
19.3643	1.0000	20.4031	1.0000	90.0000	1.0000	.2521	53.1561	1.5630
19.3643	1.0000	22.3983	.4955	90.0000	1.0000	.1328	55.6846	1.7677
18.7492	.4962	18.4080	.4949	90.0000	1.0000	.0603	47.8435	1.4841
18.7492	.4962	20.4031	1.0000	90.0000	1.0000	.1292	50.7571	1.6696
18.7492	.4962	22.3983	.4955	90.0000	1.0000	.0678	53.3483	1.8742
2.000	3.327362	2.250	2.765668	2.500	2.071095	2.750	1.549173	
3.000	1.158244	3.250	.843335	3.500	.783471	3.750	.642836	
4.000	.613621	4.250	.617021	4.500	.570164	4.750	.537848	
5.000	.507096	5.250	.437522	5.500	.387972	5.750	.305492	
6.000	.267541	6.250	.226725	6.500	.238841	6.750	.234477	
7.000	.226236	7.250	.214585	7.500	.229615	7.750	.191161	
8.000	.184147	8.250	.187456	8.500	.182500	8.750	.164551	
9.000	.153497	9.250	.154348	9.500	.129599	9.750	.104977	
10.000	.140670	10.250	.123401	10.500	.121032	10.750	.111199	
11.000	.115931	11.250	.101135	11.500	.111918	11.750	.110555	
12.000	.096516	12.250	.093541	12.500	.087001	12.750	.085251	
13.000	.097746	13.250	.087700	13.500	.086238	14.000	.069970	
14.500	.082737	15.000	.081903	15.500	.064313	16.000	.066344	
17.000	.059416	18.000	.062647	19.000	.056977	20.000	.054225	
21.000	.046082	22.000	.042550	24.000	.039737	26.000	.039216	
28.000	.032915	30.000	.031254	32.000	.030011	34.000	.023276	
36.000	.023983	38.000	.020673	40.000	.020903	42.000	.021448	
44.000	.015240	46.000	.014545	48.000	.014454	50.000	.015031	
52.000	.013195	54.000	.017235	56.000	.014883	58.000	.009972	
60.000	.012337	64.000	.008574	68.000	.008408			

ALIMIT AND WEIGHT 30.00000 -0.00000

HEIT)*D2,NT

PROGRAM ECLOP2.(M-10) WAS USED

NVA	NVB	NGAM		GA	GB	GAMMA	MNIDR
3	3	1	Z	4.0000	4.0200	90.0000	-0.0000

VAPAR	9.7464	1.6667	10.0000	0.0000	-1.0000
VBPAR	11.1119	1.4100	10.0000	0.0000	-1.0000

NTHL	THLMIN	DTHL
186	2.000	.350

RESOLUTION PARAMETERS

0.0000	3.0000	10.0000	15.0000	25.0000	35.0000	45.0000	90.0000
.4900	.7500	1.4500	1.4500	1.4500	1.5000	1.5000	1.4700

POTENTIAL PARAMETERS

.0350	5.7000	6.3000	-0.3000	-0.0000	1158.0000	3000.0000	-0.0000
-0.0000	-0.0000	-.7500	1.7500	5.7000	-2.0000		

NO(1 - 9) = X X X X X X X X X

NO(1 - 9) = X X X X X X X X X

MMSV POTENTIAL WAS USED

6.30000E+00	-0.	-0.	-9.66698E-01	-7.69227E-02	-0.	0.	0.	1.11002E+00
1.75000E+00	0.	0.	0.	0.	-7.50000E-01	1.11207E+00	2.52218E+00	-3.17501E+00

AKP,AAM,AKKM,LCCM

.6833E+01	.5033E+02	.5355E+02	154

OPACITY PARAMETERS 6.00000 5.29340 3.55340 -0.00000 -0.00000

OPACITY-2 WAS USED

REACTIVE AND ELASTIC CROSS SECTION, E

1.6102E+01	1.4520E+02	1.2801E+00

REACTIVE AND ELASTIC CROSS SECTION, E

1.8406E+01	1.5025E+02	1.4657E+00

REACTIVE AND ELASTIC CROSS SECTION, E

2.0736E+01	1.3167E+02	1.6703E+00

REACTIVE AND ELASTIC CROSS SECTION, E

1.7332E+01	1.4123E+02	1.3775E+00

REACTIVE AND ELASTIC CROSS SECTION, E

1.9544E+01	1.3500E+02	1.5630E+00

PHASE SHIFTS

1	-30.356	2	-28.824	3	-27.331	4	-25.876	5	-24.460	6	-23.083	7	-21.745	8	-20.445	9	-19.185	10	-17.964
11	-16.781	12	-15.638	13	-14.534	14	-13.469	15	-12.445	16	-11.460	17	-10.513	18	-9.609	19	-8.744	20	-7.916
21	-7.133	22	-6.390	23	-5.686	24	-5.023	25	-4.401	26	-3.819	27	-3.278	28	-2.778	29	-2.319	30	-1.899
31	-1.519	32	-1.176	33	-.876	34	-.611	35	-.382	36	-.188	37	-.028	38	.103	39	.205	40	.263

41	.336	42	.372	43	.391	44	.398	45	.393	46	.382	47	.364	48	.343	49	.314	50	.295
51	.273	52	.248	53	.225	54	.204	55	.185	56	.168	57	.151	58	.137	59	.123	60	.113
61	.103	62	.095	63	.081	64	.072	65	.065	66	.059	67	.053	68	.049	69	.044	70	.040
71	.035	72	.032	73	.031	74	.028	75	.027	76	.025	77	.023	78	.022	79	.021	80	.019
81	.018	82	.017	83	.016	84	.015	85	.014	86	.013	87	.013	88	.012	89	.011	90	.011
91	.010	92	.010	93	.009	94	.009	95	.008	96	.008	97	.007	98	.007	99	.007	100	.006
101	.006	102	.006	103	.005	104	.005	105	.005	106	.005	107	.004	108	.004	109	.004	110	.004
111	.004	112	.004	113	.003	114	.003	115	.003	116	.003	117	.003	118	.003	119	.003	120	.002
121	.002	122	.002	123	.002	124	.002	125	.002	126	.002	127	.002	128	.002	129	.002	130	.002
131	.002	132	.002	133	.001	134	.001	135	.001	136	.001	137	.001	138	.001	139	.001	140	.001
141	.001	142	.001	143	.001	144	.001	145	.001	146	.001	147	.001	148	I 149		I 150		I
151	I 152		I 153		I 154		I												

1	.80138	3.651	2	.79995	3.652	3	.79708	3.654	4	.79274	3.657	5	.78688	3.661					
6	.77943	3.666	7	.77033	3.672	8	.75949	3.679	9	.74681	3.687	10	.73220	3.697					
11	.71555	3.707	12	.69679	3.719	13	.67584	3.731	14	.65263	3.745	15	.62714	3.761					
16	.59943	3.777	17	.56945	3.795	18	.53742	3.815	19	.50350	3.836	20	.46794	3.859					
21	.43104	3.883	22	.39321	3.910	23	.35509	3.938	24	.31693	3.969	25	.27937	4.002					
26	.24294	4.037	27	.20624	4.075	28	.17568	4.116	29	.14571	4.160	30	.11866	4.207					
31	.09474	4.256	32	.07646	4.313	33	.05659	4.371	34	.04221	4.435	35	.03088	4.505					
36	.02170	4.575	37	.01491	4.654	38	.00995	4.737	39	.00645	4.826	40	.00405	4.920					
41	.00247	5.019	42	.00147	5.124	43	.00085	5.233	44	.00047	5.345	45	.00024	5.462					
46	.00014	5.581	47	.00007	5.703	48	.00004	5.327	49	.00002	5.952	50	.00001	6.079					
51	.00000	6.206	52	.00000	6.334	53	.00000	6.462	54	.00000	6.587	55	.00000	6.717					
56	.00000	6.844	57	.00000	6.971	58	.00000	7.098	59	.00000	7.225	60	.00000	7.352					
61	.00000	7.478	62	.00000	7.605	63	.00000	7.731	64	.00000	7.857	65	.00000	7.983					
66	.00000	8.108	67	.00000	8.234	68	.00000	8.359	69	.00000	8.485	70	.00000	8.610					
71	.00000	8.735	72	.00000	8.859	73	.00000	8.984	74	.00000	9.109	75	0.00000	9.233					
76	0.00000	9.358	77	0.00000	9.482	78	0.00000	9.606	79	0.00000	9.731	80	0.00000	9.855					
81	0.00000	9.979	82	0.00000	10.103	83	0.00000	10.228	84	0.00000	10.352	85	0.00000	10.476					
86	0.00000	10.603	87	0.00000	10.724	88	0.00000	10.848	89	0.00000	10.973	90	0.00000	11.097					
91	0.00000	11.221	92	0.00000	11.345	93	0.00000	11.469	94	0.00000	11.593	95	0.00000	11.717					
96	0.00000	11.842	97	0.00000	11.966	98	0.00000	12.090	99	0.00000	12.214	100	0.00000	12.338					
101	0.00000	12.462	102	0.00000	12.586	103	0.00000	12.710	104	0.00000	12.834	105	0.00000	12.958					
106	0.00000	13.082	107	0.00000	13.206	108	0.00000	13.330	109	0.00000	13.454	110	0.00000	13.579					
111	0.00000	13.703	112	0.00000	13.827	113	0.00000	13.951	114	0.00000	14.075	115	0.00000	14.199					
116	0.00000	14.323	117	0.00000	14.447	118	0.00000	14.571	119	0.00000	14.695	120	0.00000	14.819					
121	0.00000	14.943	122	0.00000	15.067	123	0.00000	15.191	124	0.00000	15.315	125	0.00000	15.439					
126	0.00000	15.563	127	0.00000	15.687	128	0.00000	15.811	129	0.00000	15.935	130	0.00000	16.059					
131	0.00000	16.183	132	0.00000	16.307	133	0.00000	16.431	134	0.00000	16.555	135	0.00000	16.679					
136	0.00000	16.803	137	0.00000	16.927	138	0.00000	17.051	139	0.00000	17.176	140	0.00000	17.300					
141	0.00000	17.424	142	0.00000	17.548	143	0.00000	17.672	144	0.00000	17.796	145	0.00000	17.335					
146	0.00000	17.455	147	0.00000	17.575	148	I	I	149	I	I	150	I	I					
151	I	I	152	I	I	153	I	I	154	I	I								

REACTIVE AND ELASTIC CROSS SECTION, E
2.1750E+01 1.2918E+02 1.7677E+00

REACTIVE AND ELASTIC CROSS SECTION, E
1.8625E+01 1.3755E+02 1.4841E+00

REACTIVE AND ELASTIC CROSS SECTION, E
2.0729E+01 1.3185E+02 1.6696E+00

REACTIVE AND ELASTIC CROSS SECTION, E
2.2617E+01 1.2656E+02 1.6742E+00

THL	IL,KVA	IL,RA	IL,VA	IL,NOM	THCM	ISIN,KVA	ISIN,RA	ISIN,VA	ISIN,NOM
2.000	3.0491E+03	2.350	1.8010E+03	2.700	9.1085E+02	3.050	5.1843E+02	3.400	3.8744E+02
3.750	3.8111E+02	4.100	3.7433E+02	4.450	5.3173E+02	4.800	2.6562E+02	5.150	2.0950E+02
5.500	1.7256E+02	5.850	1.5183E+02	6.200	1.4027E+02	6.550	1.3317E+02	6.900	1.2444E+02
7.250	1.1591E+02	7.600	1.0573E+02	7.950	9.7261E+01	8.300	9.0711E+01	8.650	8.5307E+01
9.000	8.1118E+01	9.350	7.7473E+01	9.700	7.4121E+01	10.050	7.0740E+01	10.400	6.7428E+01

10.750	6.4247E+01	11.100	6.1377E+01	11.450	5.8862E+01	11.800	5.6613E+01	12.150	5.4511E+01
12.500	5.2489E+01	12.850	5.0551E+01	13.200	4.8733E+01	13.550	4.7008E+01	13.900	4.5314E+01
14.250	4.4063E+01	14.600	4.2722E+01	14.950	4.1424E+01	15.300	4.0142E+01	15.650	3.8900E+01
16.000	3.7740E+01	16.350	3.6615E+01	16.700	3.5547E+01	17.050	3.5030E+01	17.400	3.4155E+01
17.750	3.3329E+01	18.100	3.2527E+01	18.450	3.1763E+01	18.800	3.1024E+01	19.150	3.0325E+01
19.500	2.9641E+01	19.850	2.8982E+01	20.200	2.8346E+01	20.550	2.7734E+01	20.900	2.7146E+01
21.250	2.6579E+01	21.600	2.6032E+01	21.950	2.5504E+01	22.300	2.4993E+01	22.650	2.4496E+01
23.000	2.4016E+01	23.350	2.3546E+01	23.700	2.3089E+01	24.050	2.2644E+01	24.400	2.2211E+01
24.750	2.1789E+01	25.100	2.1379E+01	25.450	2.0980E+01	25.800	2.0594E+01	26.150	2.0219E+01
26.500	1.9854E+01	26.850	1.9500E+01	27.200	1.9155E+01	27.550	1.8814E+01	27.900	1.8491E+01
28.250	1.8172E+01	28.600	1.7860E+01	28.950	1.7554E+01	29.300	1.7255E+01	29.650	1.6962E+01
30.000	1.6674E+01	30.350	1.6399E+01	30.700	1.6117E+01	31.050	1.5847E+01	31.400	1.5581E+01
31.750	1.5321E+01	32.100	1.5065E+01	32.450	1.4814E+01	32.800	1.4568E+01	33.150	1.4327E+01
33.500	1.4090E+01	33.850	1.3858E+01	34.200	1.3631E+01	34.550	1.3408E+01	34.900	1.3188E+01
35.250	1.2974E+01	35.600	1.2763E+01	35.950	1.2556E+01	36.300	1.2353E+01	36.650	1.2153E+01
37.000	1.1957E+01	37.350	1.1764E+01	37.700	1.1574E+01	38.050	1.1387E+01	38.400	1.1203E+01
38.750	1.1022E+01	39.100	1.0844E+01	39.450	1.0667E+01	39.800	1.0493E+01	40.150	1.0321E+01
40.500	1.0151E+01	40.850	9.9805E+00	41.200	9.8220E+00	41.550	9.6626E+00	41.900	9.5044E+00
42.250	9.3540E+00	42.600	9.2046E+00	42.950	9.0577E+00	43.300	8.9135E+00	43.650	8.7715E+00
44.000	8.6310E+00	44.350	8.4919E+00	44.700	8.3542E+00	45.050	8.2177E+00	45.400	8.0830E+00
45.750	7.9506E+00	46.100	7.8205E+00	46.450	7.6932E+00	46.800	7.5686E+00	47.150	7.4464E+00
47.500	7.3268E+00	47.850	7.2095E+00	48.200	7.0945E+00	48.550	6.9815E+00	48.900	6.8706E+00
49.250	6.7613E+00	49.600	6.6532E+00	49.950	6.5463E+00	50.300	6.4403E+00	50.650	6.3352E+00
51.000	6.2315E+00	51.350	6.1295E+00	51.700	6.0295E+00	52.050	5.9315E+00	52.400	5.8355E+00
52.750	5.7417E+00	53.100	5.6500E+00	53.450	5.5606E+00	53.800	5.4731E+00	54.150	5.3874E+00
54.500	5.3031E+00	54.850	5.2201E+00	55.200	5.1381E+00	55.550	5.0570E+00	55.900	4.9767E+00
56.250	4.8973E+00	56.600	4.8188E+00	56.950	4.7416E+00	57.300	4.6661E+00	57.650	4.5922E+00
58.000	4.5202E+00	58.350	4.4500E+00	58.700	4.3817E+00	59.050	4.3155E+00	59.400	4.2509E+00
59.750	4.1877E+00	60.100	4.1255E+00	60.450	4.0638E+00	60.800	4.0026E+00	61.150	3.9420E+00
61.500	3.8821E+00	61.850	3.8230E+00	62.200	3.7646E+00	62.550	3.7078E+00	62.900	3.6523E+00
63.250	3.5985E+00	63.600	3.5465E+00	63.950	3.4960E+00	64.300	3.4467E+00	64.650	3.3988E+00
65.000	3.3499E+00	65.350	3.3008E+00	65.700	3.2502E+00	66.050	3.1975E+00	66.400	3.1422E+00
66.750	3.0845E+00								

POTENTIAL

X	VS	R	V
.500	2.643E+02	2.850	9.250E+00
.510	2.343E+02	2.907	8.194E+00
.520	2.071E+02	2.964	7.248E+00
.530	1.832E+02	3.021	6.411E+00
.540	1.619E+02	3.078	5.666E+00
.550	1.430E+02	3.135	5.006E+00
.560	1.262E+02	3.192	4.419E+00
.570	1.114E+02	3.249	3.898E+00
.580	9.815E+01	3.306	3.435E+00
.590	8.643E+01	3.363	3.025E+00
.600	7.603E+01	3.420	2.661E+00
.610	6.682E+01	3.477	2.339E+00
.620	5.865E+01	3.534	2.053E+00
.630	5.142E+01	3.591	1.800E+00
.640	4.502E+01	3.648	1.576E+00
.650	3.935E+01	3.705	1.377E+00
.660	3.434E+01	3.762	1.202E+00
.670	2.991E+01	3.819	1.047E+00
.680	2.600E+01	3.876	9.102E-01
.690	2.257E+01	3.933	7.894E-01
.700	1.951E+01	3.990	6.829E-01
.710	1.683E+01	4.047	5.894E-01
.720	1.447E+01	4.104	5.065E-01
.730	1.240E+01	4.161	4.338E-01
.740	1.057E+01	4.218	3.700E-01

.760	7.570E+00	4.332	2.650E-01
.770	6.343E+00	4.389	2.220E-01
.780	5.272E+00	4.446	1.845E-01
.790	4.337E+00	4.503	1.515E-01
.800	3.523E+00	4.560	1.233E-01
.810	2.816E+00	4.617	9.857E-02
.820	2.204E+00	4.674	7.713E-02
.830	1.674E+00	4.731	5.868E-02
.840	1.218E+00	4.788	4.263E-02
.850	8.262E-01	4.845	2.892E-02
.860	4.911E-01	4.902	1.719E-02
.870	2.057E-01	4.959	7.199E-03
.880	-3.609E-02	5.016	-1.263E-03
.890	-2.396E-01	5.073	-8.307E-03
.900	-4.098E-01	5.130	-1.434E-02
.910	-5.507E-01	5.187	-1.927E-02
.920	-6.662E-01	5.244	-2.332E-02
.930	-7.596E-01	5.301	-2.659E-02
.940	-8.357E-01	5.358	-2.918E-02
.950	-8.913E-01	5.415	-3.119E-02
.960	-9.344E-01	5.472	-3.270E-02
.970	-9.652E-01	5.529	-3.378E-02
.980	-9.854E-01	5.586	-3.449E-02
.990	-9.966E-01	5.643	-3.488E-02
1.000	-1.000E+00	5.700	-3.500E-02
1.010	-9.963E-01	5.757	-3.487E-02
1.020	-9.860E-01	5.814	-3.451E-02
1.030	-9.703E-01	5.871	-3.396E-02
1.040	-9.504E-01	5.928	-3.326E-02
1.050	-9.270E-01	5.985	-3.244E-02
1.060	-9.009E-01	6.042	-3.154E-02
1.070	-8.726E-01	6.099	-3.055E-02
1.080	-8.433E-01	6.156	-2.951E-02
1.090	-8.127E-01	6.213	-2.844E-02
1.100	-7.815E-01	6.270	-2.735E-02
1.120	-7.190E-01	6.384	-2.517E-02
1.140	-6.596E-01	6.498	-2.309E-02
1.160	-6.042E-01	6.612	-2.115E-02
1.180	-5.522E-01	6.726	-1.933E-02
1.200	-5.035E-01	6.840	-1.762E-02
1.220	-4.581E-01	6.954	-1.603E-02
1.240	-4.159E-01	7.068	-1.456E-02
1.260	-3.768E-01	7.182	-1.319E-02
1.280	-3.406E-01	7.296	-1.192E-02
1.300	-3.071E-01	7.410	-1.075E-02
1.320	-2.764E-01	7.524	-9.673E-03
1.340	-2.482E-01	7.638	-8.687E-03
1.360	-2.224E-01	7.752	-7.785E-03
1.380	-1.990E-01	7.866	-6.965E-03
1.400	-1.778E-01	7.980	-6.222E-03
1.420	-1.586E-01	8.094	-5.552E-03
1.440	-1.414E-01	8.208	-4.950E-03
1.460	-1.260E-01	8.322	-4.412E-03
1.480	-1.124E-01	8.436	-3.934E-03
1.500	-1.003E-01	8.550	-3.511E-03
1.550	-7.634E-02	8.835	-2.672E-03
1.600	-5.765E-02	9.120	-2.088E-03
1.650	-4.837E-02	9.405	-1.693E-03
1.700	-4.060E-02	9.690	-1.421E-03
1.750	-3.446E-02	9.975	-1.206E-03
1.800	-2.906E-02	10.260	-1.017E-03
1.850	-2.462E-02	10.545	-8.618E-04

1.900	-2.046E-02	10.830	-7.335E-04
1.950	-1.791E-02	11.115	-6.270E-04
2.000	-1.537E-02	11.400	-5.381E-04
2.050	-1.324E-02	11.685	-4.636E-04
2.100	-1.145E-02	11.970	-4.008E-04
2.150	-9.935E-03	12.255	-3.477E-04
2.200	-8.649E-03	12.540	-3.027E-04
2.250	-7.552E-03	12.825	-2.643E-04
2.300	-6.615E-03	13.110	-2.315E-04
2.350	-5.810E-03	13.395	-2.034E-04
2.400	-5.118E-03	13.680	-1.791E-04
2.450	-4.520E-03	13.965	-1.582E-04
2.500	-4.002E-03	14.250	-1.401E-04
2.550	-3.552E-03	14.535	-1.243E-04
2.600	-3.150E-03	14.820	-1.106E-04
2.650	-2.817E-03	15.105	-9.860E-05
2.700	-2.517E-03	15.390	-8.811E-05
2.750	-2.254E-03	15.675	-7.889E-05
2.800	-2.022E-03	15.960	-7.078E-05
2.850	-1.818E-03	16.245	-6.363E-05
2.900	-1.637E-03	16.530	-5.730E-05
2.950	-1.477E-03	16.815	-5.170E-05

30.000000 -0.000000

SCALING FACTOR = 1.8513E-03

STANDARD DEVIATION = 1.0736E-01

III. THE INTERACTION OF $He(2^3S)$ + Ar

A. Introduction

The interaction between $He(2^3S)$ + Ar has in recent years established itself as one of the prototype systems for the study of chemi-ionization by a metastable atom. Its principle attractiveness, from a practical standpoint, lies largely in the relative ease and low cost with which the two reactant gases can be obtained. It is coincidentally fortunate that the use of metastable He is uniquely well-suited to Penning ionization studies. The 2^3S state of He has an energy of 19.82 eV above the ground state, thus with the exception of collision partners such as Ne and He which have acceptor levels of comparable energy, $He(2^3S)$ atoms can only be quenched via ionization channels. In other words, the excess electronic energy of the metastable atom is effectively expended in the promotion of an electron belonging to its quenching agent into the continuum.

This important physical process of energy transfer leading to ionization can be studied from a number of perspectives. In any given experiment, only a few facets can be conveniently explored. Emphasis can for example be placed on the He metastable atom itself as in elastic cross section measurements, or on the various ions formed as in ionization cross section measurements, or on the electrons ejected in the ionization process as in Penning electron energy measurements (PEED). For $He(2^3S)$ + Ar, its popularity means that a large body of information exists on all these fronts. Rothe et al.[1], using a beam-gas apparatus, monitored the total cross section of reaction as a function of the relative collision energy. They observed that their measured energy dependence was very similar to that for Li + Ar though the absolute cross section was higher

for He(2^3S) + Ar. The cross section peaks around 1300 m/sec with a value of ~500 A^2. Using a Lennard-Jones potential to fit their data, Rothe et al. deduced a well-depth for the interaction to be 0.11 Kcal/mole located at an inter-nuclear separation of 4.52 A. While such total cross section measurements should be quite sensitive to the real part of the potential V_0, especially in the range of large internuclear distances, they necessarily obscure the effect of the potential's imaginary component v_i as the inelastic processes for which the latter is designed to account have cross sections at least an order of magnitude smaller. Thus it is only be measuring directly the total ionization cross section can v_i be more explicitly revealed. Such a measurement has been undertaken by several laboratories. Illenberger and Niehaus[2], using a crossed-beam time-of-fligh chnique, measured the total ionization cross section in the range of (1-5) x 10^5 cm/sec. Pesnelle et al.[3], employing essentially the same technique, made measurements covering the same range. The results obtained by these two groups are in good agreement at low energies (<300 m/sec), but they deviate rather significantly at higher energies. Both groups, in fitting their data, assumed for their covalent interaction potential that proposed by Olson[4], and obtained the corresponding best-fit V_i. An exponential function is used to represent the ionization width in both cases. Illenberger and Niehaus's V_i has a steeper slope than that of Pesnelle's et al.; this is necessary to simulate the relatively early onset of saturation observed by the former group at high energies.

Many other groups have also measured the absolute total ionization cross section.[12] However, the general utility of their measurements,

in terms of providing information on the nature of the interaction potential involved, is severely limited by the fact that these measurements are only made at one or two energies. Nonetheless, they can serve as calibration points in certain instances.

Penning electron energy spectra for $He(2^3S)$ + Ar have been obtained by Hotop and Niehaus at several energies (30 meV, 95 meV and 125 meV).[5] Peculiarities in such spectra are closely related to V^* ($V^* = V_0 + iV_i$) the entrance channel potential, as well as V^+, the exit channel potential. Moreover, PEED can in principle provide a direct measurement of the branching ratio of associative to Penning ionization (provided that R_{AI}, the distance of internuclear separation below which associative ionization predominates, is known). If given in high enough resolution, PEED also reflects directly the population of different electronic and vibrational states in the Penning ion.

For $He(2^3S)$ + Ar, the less easily accessible angular distribution of Penning electrons has also been obtained by Hotop and Niehaus.[6] There is a two-fold purpose to making such a measurement. They are: (a) to detect any anisotropy in the imaginary part of the potential which is generally assumed to be isotropic; (b) to eliminate uncertainties regarding the evaluation of the shapes of the Penning electron spectra obtained at one fixed angle. In the case of $He(2^3S)$ + Ar, Hotop and Neihaus observed an enhancement of electrons in the direction of the He atom. They attributed this phenomenon to the dominance of an electron exchange mechanism in the ionization process.

Finally, Moseley et al., using an optical technique to monitor the attenuation of a $He(2^3S)$ beam as a function of target gas pressure and

beam pathlength, obtained absolute cross section for the quenching process in the range of 150-1600 eV. Their data showed the not unexpected inverse energy dependence since at such high energies, the classical turning point is essentially constant with respect to energy, thus the probability of ionization should be proportional to the amount of time the particles are in close contact with each other, and hence inversely proportional to the relative velocity of collision. Mosely et al. however did not go low enough in energy to pin down where exactly does the maximum in the ionization cross section occur.

This maximum is predicted by Olson[4] in his theoretical calculation to occur around 10 eV. The functional dependence of the interacion potential V_0 adopted by Olson was chosen so that V_0 possessed a realistic shielded Coulomb form at small separations, and the correct $-(C_{ab}/R^6)$ dependence at large separations. The C_{ab} coefficients are taken from the work of Bell, Dalgarno and Kingston.[6] Olson's potential is parametrized to agree with the glory-scattering results of Rothe et al. which, as suggested earlier, provides a determination of the product of the minimum of the potential and its location, i.e. $\in R_m$. For his ionization width, Olson used the exponential form exp(-R/B), and normalized it to the thermal energy results of Sholette and Muschlitz who obtained 7.6 A^2 for the ionization cross section.[7] The simple one-parameter form for the width was necessitated by the lack of accurate measurements of the ionization cross section over a wide range of energies at that time, so that it would be inappropriate if not indeed innocuous to introduce additional adjustable parameters just for the sake of fitting the total cross section data. Using his potential, Olson was able to reproduce the

high energy cross section data to within 20%. However, this potential, as we shall see later, fails to harmonize with the more sensitive differential cross section data.

Hickman and Morgner[8] undertook to calculate the elastic scattering cross section, the differential cross section as well as the total ionization cross section for $He(2^3S)$ + Ar using the quantum mechanical counterpart of Miller's semi-classical theory.[9] Complex phase shifts were determined by exact numerical solution of the radial Schroedinger equation with a complex potential. The complex potential is of the form $V_0-i(\Gamma/2)$, where V_0, the real component, is an MSV potential with its parameters adjusted to fit the differential cross section data of Brutschy, Haberland and Schmidt[10] at one energy (the fit is however fairly poor in the small angle region). Γ, the coupling width, is taken to be of the form $A\exp(-BR)$, and the total ionization cross section measurements of Illenberger and Niehaus[2] is used to determine the parameters A and B. With their optimum complex potential, Hickman and Morgner also secured V^+, the ionic potential, by fitting a Morse form for the potential to the energy-dependent associative ionization cross section as obtained by Pesnelle et al. and also by Gerard and Hotop.[11] Equipped thus with the three basic quantities, V, Γ, and V^+, which are necessary to phenomenologically describe the Penning ionization process, Hickman and Morgner proceeded further to calculate other experimental observables such as the Penning electron energy distribution, and the angular distribution of Ar^+ ions in the center of mass frame. Hickman and Morgner's thoroughness is however overshadowed by the fact that they had started

out with a complex potential which did not fully concur with the differential cross section measurements, and this inaccuracy necessarily propagated through all their other calculations.

We see from the above discussion and summary of available experimental information on He(2^3S) + Ar that while a number of potentials can indeed be found to fit such data as total elastic cross section and total ionization cross section, these potentials need not be compliant with the more stringent (thus discriminating) differential cross section. From Eq. (40) in Chapter II, we note that the differential cross section, by virtue of its unaveraged nature, retains valuable information about the interferences between contributing partial waves in the scattering event. Such interferences, when resolved in an experimental measurement, impose severe constraints on many of the important features of the interaction potential involved. Therefore, in order for a proposed potential to be acceptable, it must, as a necessary, though not sufficient condition, reproduce the differential cross section data.

With that in mind, we have carried out differential cross section measurements for He(2^3S) + Ar at two energies: 65 meV and 135 meV. At the lower collision energy, undulations in the small angle region are quite well resolved. The system He(2^3S) + Ar is in many ways very well-suited to beam studies as ionization is known to take place at very small impact parameters only. This enables us to regard the differential cross section as being composed of two regions, one in which the influence of the absorptive component of the potential V_i is negligible, and the other where V_i plays a major role. The first region is then comprised primarily of those scattering events which stem from large impact parameters; as the

particles are only mildly perturbed in their trajectory in this case, the angle of scattering is relatively small. The second region, by contrast, involves the participation of small impact parameters which in all probability result in large angle scattering. Our assertion that this latter region is quite sensitive to V_i is equivalent to saying that V_i is highly localized in interaction space, and therefore can be sampled only when the particles come in fairly close contact with each other.

The following procedure with which to analyse our differential cross section data therefore suggests itself. From the small angle region of our measurements, we can extract information about the real part of the potential around and outside of the well vicinity. Obtaining this, we can then proceed to represent the imaginary part of the potential by a suitable functional form whose parameters are now adjusted to fit the large angle data. The potential we have so derived agrees very well with the total ionization cross section data of Illenberger and Niehaus[2] as well as the total elastic cross section measurements of Rothe and Neynaber.[1] As mentioned previously, Brutschy et al. have also recently scanned the differential cross section for $He(2^3S) + Ar$;[10] their data covered a much wider energy range than ours; gratifyingly, their proposed potential is substantially in harmony with what we have found.

In our analysis of the scattering data, we have, for ease and speed of computation, used the first order semiclassical approximation as derived in Chapter II to calculate the real and imaginary part of the phase shift. While this approximation has been adopted in most previously reported work using an optical potential, we recognize that its validity rests on the assumption that the imaginary part of the potential V_i acts

only as a perturbation on the real part V_0. That is $V_i << V_0$. This criterion, for a particular V_i, is of course more true for certain collision energies than others (specifically, for lower collision energies). But even for one fixed energy, it is important to determine the maximum bound for V_i, relative to V_0, below which this approximation for the phase shifts holds. To this end, we have varied our best fit V_i to monitor changes in the small angle region of the differential cross section. We know that as long as the range of V_i is not significantly altered, there should not be any major variations in the differential cross section at small angles. If such is found not to be the case, then we must obviously have over-extended the capability of our approximation. This being so, we would then have to either include higher order terms in the Taylor expansion of the phase shifts (see Eq.(23) and (24) in Chapter II), or even forego this approximation scheme all together. The exact quantum mechanical calculations would then have to be carried out. We have accordingly also made comparisons between the semiclassical phase shifts and their quantum mechanical counterparts as V_i is changed by several orders of magnitude.

B. Data Analysis

The measured differential cross section for He(2^3S) + Ar at 65 and 132 meV are shown in Fig. 1a and 1b. A MMSV (Morse-Morse-Spline-Van der Waals) potential was used to fit the data. This form for the potential affords much more flexibility than the conventional single Morse form. The innter Morse function in an MMSV potential can be varied

independently of its outer counterpart, thus permitting greater control over the slope of the repulsive wall. The potential in reduced unitless parameters is written as

$$f(x) = \exp[-2\beta_1(x-1)] - 2\exp[-\beta_1(x-1)] \qquad x_1 < x \leqslant 1$$

$$f(x) = \exp[-2\beta_2(x-1)] - 2\exp[-\beta_2(x-1)] \qquad 1 < x \leqslant x_2$$

$$f(x) = b_1 + (x-x_2)\left\{b_2 + (x-x_3)\left[b_3 + (x-x_2)b_4\right]\right\} \qquad x_2 < x \leqslant x_3$$

$$f(x) = -c_6x^{-6} - c_8x^{-8} \qquad x_3 < x \leqslant \infty$$

where

$$f(x) = \frac{V(r)}{\epsilon} \; ; \quad x = \frac{r}{r_m} \; ; \quad c_n = \frac{C_n}{\epsilon r_m^n} \qquad (1b)$$

The values for the various parameters defining our best-fit potential are tabulated in Table I. C_6 and C_8 constants are taken from the recent calculations performed by Proctor and Stwalley.[13] The MMSV potential we obtained is plotted in Fig. 2, with the dotted portion of the curve indicating the region not sampled in our experiment.*

Other forms for the potential such as a simple MSV[14], and the analytic potential proposed by Olson[4] were also tried. They however failed to yield very good agreement with the small angle scattering data; this can be seen in Fig. 3. As we again argue later, discrepancies in this region of the differential cross section cannot be compensated for by adjusting the imaginary part of the potential.

In the framework of semiclassical analysis, V_i, the complex component of the optical potential, plays no role in the trajectory of the particle. This is so because the real part of the phase shift depends solely on V_o. V_i exerts its weight only in the imaginary component of the phase shift. We recall from Chapter II that the complex phase shift is approximated by

$$\mathrm{Re}[\eta(\ell)] = \hbar^{-1}\int_{R_c}^{\infty}\left\{\left[2\mu(E-V_o)-\frac{\hbar^2(\ell+\frac{1}{2})^2}{R^2}\right]^{\frac{1}{2}} - k\right\} dR - kR_c + \tfrac{1}{2}\pi(\ell+\tfrac{1}{2})$$

$$\mathrm{Im}[\eta(\ell)] = \hbar^{-1}\int_{R_c}^{\infty}(\tfrac{1}{2}\mu)^{\frac{1}{2}}\frac{V_i\,dR}{\left[E-V_o-\frac{\hbar^2(\ell+\frac{1}{2})^2}{2\mu R^2}\right]^{\frac{1}{2}}} \qquad (1)$$

* While this MMSV potential has about the same well depth as compared to the MSV potential previously reported by our group,[15] the location of its minimum has been shifted out. The slope of its repulsive wall is also less steep than before. It should be noted that the very recent calculations by Nakamura on He(2^3S) + Ar was based on our old MSV potential.[15]

where R_c is the distance of closest approach, and is the largest root of

$$1 - \frac{V_0}{E} - \frac{\hbar^2(\ell+\frac{1}{2})^2}{2E\mu R^2} = 0$$

Using

$$\frac{dR}{dt} = \left(\frac{2E}{\mu}\right)^{\frac{1}{2}} \left[1 - \frac{V}{E} - \frac{\hbar^2(\ell+\frac{1}{2})^2}{2ER^2\mu}\right]^{\frac{1}{2}} \tag{1a}$$

$\mathrm{Im}[\eta(\ell)]$ in Eq. (1) becomes

$$\mathrm{Im}[\eta_\ell] = \hbar^{-1}\left[\int_0^\infty V_i(t)\,dt\right]_\ell$$

Thus $\mathrm{Im}[\eta_\ell]$ is just the time average of V_i over the trajectory dictated by V_0. Denoting this time average by $\overline{V}_i$, Eq. (2) can be written as

$$\mathrm{Im}[\eta_\ell] = \hbar^{-1}\,\overline{V}_i\,T \tag{3}$$

where τ represents the period of time that the collision pair spends in the reaction zone characterized by V_i. In this way, V_i serves only to describe that confined region of space in which reaction can take place, and it is V_0 which determines how long the collision pair spends under the influence of V_i (V_0 plays a role analogous to the real part of the index of refraction which adjusts for the speed of light through a refracting or absorbing medium). Given as a function of internuclear distance, V_i represents the extent of coupling between the discrete electronic state $He^* + Ar$ and the $He + Ar + e^-$ continuum. This coupling, since it denotes an electron exchange mechanism, is not only expected to be stronger at shorter interatomic distances, but is also, given the properties of s-type atomic wavefunctions, expected to behave in an exponential manner. For reaction probabilities that are not too large, V_i is logically buried within the repulsive core of V.

Finally, it must be mentioned for completeness that the parameterization of V_i is sometimes all together bypassed. Instead, the necessary parametrization is carried out at the stage of the reaction probability, which is better known as the opacity function. This probability is related to V_i via

$$P_\ell = 1 - \exp(-4\ \mathrm{Im}[\eta_\ell])$$

$$= 1 - \exp \int_{R_c}^{\infty} 4 \left[\frac{V_i}{\hbar V_\ell}\right] dR \qquad (4)$$

Computationally, this procedure is more direct and convenient. However, the advantages of using P_ℓ instead of V_i are ultimately offset by the fact that the P_ℓ thus obtained seldom transcends in its application beyond the particular set of experimental data under consideration. This is in contrast to finding a V_i that agrees with the data. General features in the optical potential can be more easily extended to understand new data and to make predictions about other similar dynamical processes.

In our analysis, the parametric form for the imaginary potential is

$$V_i(R) = \exp\left[-B(R-R_0)\right] \quad \text{(in kcal/mole)} \quad \text{(R in Å)} \tag{4a}$$

We feel that the existing plethora of data on $He(2^3S)$ + Ar does permit the determination of the two adjustable parameters B and R_0. Moreover, the functional form we have chosen should be quite adequate for the range of energies sampled in our differential cross section measurements. We recognize however that this simple exponential form need not hold for very small R (which generally corresponds to the high collision energy region). For example, the calculations by Miller et. al. on the system He(2S) + H yielded a V_i which levels off to a constant value as $R \to 0$.[16]

C. The Total Ionization Cross Section

Using our best fit V_i and V_o, we have calculated the total cross section for ionization as a function of collision velocity in the range of 1000-5000 m/sec. We have not attempted to extend our calculation to a lower energy range (where the relative kinetic energies become comparable or less than the potential well depth) because at such energies, complications arising out of the phenomenon of orbiting resonances can set in. This corresponds to a situation where we have some value of the angular momentum ℓ for which the collision energy just equals the effective potential energy. This means that the linear velocity (Eq. (1a)) can become, at a certain internuclear distance, zero for this particular ℓ. The particles, in principle, can then orbit around each other with separation R for an indefinitely long period. If the ionzation width is non-negligible at R, then from Eq. (3), we see that since τ is now very large, a finite V_i would result in a high probability for ionization. Such resonances are very sensitive to the exact form of the attractive part of the interaction potential. So far, they have yet been experimentally observed for He(2S) + Ar. This is due largely to the fact that they are very narrow, and their energies lie below 1 meV.

Our calculated cross section follows closely the experimental data of Illenberger and Niehaus[2] as shown in Fig. 4.

D. Total Elastic Cross Section

We have also calculated the total elastic cross section in the relative velocity range of 700-4000 m/sec. This is the region where experimental

measurements have been made by Rothe and Neynaber.[1] Our calculation reproduces very well the broad peak around 1300 m/sec. This is shown in Fig. 5.

It is instructive to compare our calculated cross section with that obtained via the Schiff-Landau-Lifshitz approximation.[17] In this approximation, we have the total cross section given by the simple formula

$$\sigma_{\substack{TOTAL \\ ELAS}}(V) = 8.083 \left[\frac{C_b}{\hbar V}\right]^{2/5} \quad (\text{Å}^2) \tag{5}$$

Eq. (5) is expected to be valid for scattering of neutrals in the thermal energt range provided the influence of the shortrange exchange and repulsive forces can be neglected. Then the absolute size of the total cross section averaged over the glory oscillation is only determined by the Van der Waals constant.[18] The SLL formula gives the straight line in Fig. 5.

E. The Ionic Potential

As discussed previously, we can obtain the ionic potential for He + Ar^+ if we know the covalent potential for He* + Ar as well as the absolute associative ionization cross section as a function of energy. The following procedure is then used. From Eq. (57) in Chapter II, we can, for various values of the collision energy, calculate the total associative ionization cross section as a function of the parameter R_{AI}. This results in a family of R_{AI} vs. $\sigma(R_{AI},E)$ curves onto which we can now

mark the experimentally determined associative ionization cross section. As shown in Fig. 6, the intersection of the experimental data curve with each theoretical curve gives the correct R_{AI} for each collision energy E. Once $R_{AI}(E)$ is found, we can use Eq. (59) in Chapter II to calculate $V^{+}(R_{AI})$.

The ionic potential so obtained is plotted in Fig. 7. We note that the experimental data only permits an accurate determination of the ionic potential up to 3.4 A, the behavior of the potential at smaller internuclear distances is uncertain. Had our covalent potential for He^{*} + Ar been more repulsive, so that $V^{*}(R_{AI}) - E = 0$ is satisfied for a larger R_{AI}, then we would be able to obtain the entire well-region of the ionic potential.

F. Opacities

The probability of ionization as a function of the angular momentum ℓ is shown in Fig. 8 for various energies. We see that for small collision energies the shape is roughly Gaussian; for large energies, saturation sets in at the lower values of the angular momentum ℓ. This is expected since at the higher energies, a much stronger region of V_i is sampled, and small angular momenta with their concomitant smaller classical turning points should therefore lead to strong absorption.

Fig. 9 gives the classical turning point as a function of the angular momentum ℓ for the same range of energies as in Fig. 8. We see that for small values of ℓ (where reaction is most likely to take place), the classical turning point varies very slowly.

G. Sources of Uncertainty

In fitting our data, we have assumed that the real and imaginary component of the interaction potential can be independently determined. This however is not strictly true if the available information is confined to only the differential cross section data. Specifically, there exists a trade-off relationship between the slope of the repulsive wall of V as determined by β_1 in Eq. (1b), and the imaginary potential V_i. Thus one can have different combinations of β_1 and V_i all yielding essentially the same fit to the differential cross section measurement 0° to 90° (lab.). This ambiguity can be removed if total ionization cross section measurements are made which cover the range of chemically accessible energies. This is made apparent in Fig. 10 in which we show two such combinations of β_1 and V_i. We note that while there is virtually no discernible difference in the calculated differential cross sections, the total cross section values obtained from them exhibit a marked dissimilarity.

In addition to the aforementioned indistinctness in the contributions of β_1 and V_i, $V_i(R)$ itself is the source of yet another ambiguity. When V_i is changed to compensate for so that the calculated cross section remains the same, this can be accomplished in two ways. (a) $V_i(R)$ is uniformly increased or decreased by changing R_0 in Eq. (4a) only; (b) The coefficient B in V_i is changed while keeping R_0 the same. The differential cross section measured at one kinetic energy is unable to distinguish which approach is more valid or realistic. Again, it is only by considering how these two different V_i's are reflected in the energy dependence of the total ionization cross section, one is able

to secure the desirable confidence in a particular V_i. Of course, if differential cross section measurements are carried out over a wide range of energies, and if the oscillations at small angles are resolved for at least one energy (generally at low energy), then one can fairly uniquely determine both parts of the potential by imposing the principle of self-consistency without the need for total cross section data. This however is seldom realizable in practice. It is very difficult to get differential cross section information for the same broad range of energies as is routinely accomplished in total cross section measurements. The two sources of data therefore go hand in hand in establishing the most accurate potential.

Another assumption inherent in our analysis is that $V_i(R)$ is independent of the collision energy.** This is the so-called local complex potential approximation. It is akin to the Born-Oppenheimer approximation in that we prescind from our consideration of the mechanism which leads to ionization the effect of the nuclear motion. Thus we only look at the spatial dependence of the ionization coupling function V_i, and neglect, assuming it to be negligible, its temporal or energy dependence. Granted, from the standpoint of the reaction probability, there is already an energy factor which is found in the inverse velocity term multiplying V_i (Eq. (4)). However, it is not clear that V_i itself is strictly energy-independent (formal derivation of the optical model in no way precludes this possibility). Certainly, if the widely accepted mechanism of electron exchange resulting in Penning ionization is correct,

** This assumption should be quite reasonable in the energy range our experiment has been performed.

then it is reasonable to believe that as the interacting particles are hurled at each other with higher collision velocities, the postulated concerted process of electron transfer and ejection should have a diminished coupling strength. Thus in the overall reaction probability, there would be two forces causing it to decrease as a function of collision energy. Moreover, these forces may enjoy separate regions of dominance.

H. Validity of Semiclassical Approach

We have performed calculations to investigate the validity of Eq. (1) for the phase shift. Roberts and Ross[19] have already shown that, to a good approximation, the imaginary part of the phase shift can be calculated from Eq. (1) for a Lennard Jones or an exponential potential for a wide range of magnitudes of V_i. We found this to be the case with our MMSV potential also. However, significant deviation from the simple formula Eq. (1) for the real part of the phase shift was observed as V_i was increased. This deviation caused a large error in the differential elastic scattering cross section calculated from these phase shifts.

Eq. (1) is based on the assumption that the real part of the phase shift does not change as the imaginary part of the potential is "turned on". We have investigated this assumption by comparing phase shifts calculated quantum mechanically for the potentials V and $V-iV_i$. We found a fairly simple relationship between the change in the real part of the phase shift and the magnitude of the opacity, Eq. (4). This relation, shown graphically in Fig. 11, is nearly independent of the size of V_i or the partial wave

number, Thus if $\{\xi_\ell^\circ\}$ is the set of exact phase shifts for V, and $\{\xi_\ell + i\,\zeta_\ell\}$ those for $V-iV_i$, we have plotted $|\xi_\ell\ \xi_\ell^\circ|$ vs. $(1 - e^{-4\zeta\ell})$ (note: $\zeta_\ell \approx \zeta_\ell^\circ$). Fig. 11 shows that as long as the opaci y is smaller than about 0.9, the absolute error in ξ_ℓ is fairly small.

ξ_ℓ, however, is not a measurable quantity. In a practical calculation one normally calculates the differential cross section using the standard formula

$$\frac{d\sigma}{d\theta} = \lambda\!\!\!^{-2}\left|\sum_\ell (2\ell+1)\left[1 - e^{2i(\xi_\ell+i\zeta_\ell)}\right] P_\ell(\cos\theta)\right|^2 \qquad (6)$$

The overall reliability of Eq. (1) must be assessed by comparing the exact $\frac{d\sigma}{d\theta}$ (above) with that calculated using $\xi_\ell^\circ + i\zeta_\ell$. This is shown in Fig. 12. Using the best fit V_i, the quantum mechanical and the approximate semiclassical results are essentially the same at 65 MeV. However, if V_i is increased by a factor of 5, the approximate semiclassical analysis breaks down. Quantum mechanically, it is seen that as V_i is increased, only the large angle $\frac{d\sigma}{d\theta}$ is affected; $\frac{d\sigma}{d\theta}$ at small angles remains essentially unchanged. This is in accord with physical intuition.

When may Eq. (1) be safely employed? Although we know of no precise criteria, the following observations seem pertinent. For our optical potential $V-iV_i$, all the opacities P_ℓ's have values ≤ 0.7. For $V-i5V_i$, on the other hand, a sizable number of the partial waves with non-vanishing P_ℓ's have opacities exceeding 0.95. In fact, there are some 26 ℓ's, out of a total of 56 significant partial waves (with $P_\ell \geq 0.01$), for which

there is approximately unit probability for ionization. Referring to Fig. 10a, we see that $5V_i$ corresponds to a case where the magnitude of the imaginary part of the potential at the classical turning point becomes comparable to that of V_0, the real part of the potential. Under such circumstances, one does not expect the first order semiclassical approximation for the real part of the phase shifts to be reliable.

I. Conclusion

It is found that at low energies, for a given V, the total ionization cross section is much less sensitive to a particular V_i than at higher energies. Since the high energy data play such a vital role in determining V_i, it is important that there is no controversy in the measurements by different groups. This unfortunately is not the case. Pesnelle et al.,[3] and Illenberger and Niehaus[2] have both investigated the energy dependence of the total ionization cross section. While their results agree at low energies, this congeniality fails to carry through to higher energies where radically different behaviors are observed by the two groups. We are decidly biased in favoring Illenberger's data, which happen to agree with our own calculations. It would be most beneficial if another total ionization cross section measurement is made to arrest the existing uncertainty.

REFERENCES - CHAPTER III.

1. E. W. Rothe, R. H. Neynaber and S. M. Trujillo, J. Chem. Phys. 42, 3310 (1965).
2. E. Illenberger and A. Niehaus, Z. Phys. B20, 33 (1975).
3. A. Pesnelle, G. Watel and C. Manus, J. Chemp. Phys. 62, 3590 (1975).
4. R. E. Olson, Phys. Rev. A6, 1031 (1972).
5. H. Hotop and A. Niehaus, Z. Phys. 238, 452 (1970).
6. H. Hotop and A. Niehaus, Chem. Phys. Lett., 8, 497 (1971).
7. W. P. Sholette and E. E. Muschlitz, Jr. J. Chem. Phys. 36, 3368 (1962).
8. A. P. Hickman and H. Morgner, J. Phy. B, 9, 1765 (1976).
9. W. H. Miller, J. Chem. Phys. 52, 3563 (1970).
10. B. Brutschy, H. Haberland and K. Schmidt, J. Phys. B 9, 1 (1976).
11. Gerard and Hotop, 1975, unpublished results.
12. See for example:
    (a) E. E. Benton, E. E. Ferguson, F. A. Matsen and W. W. Robertson, Phys. Rev. 127, 206 (1962).
    (b) J. S. Howard, J. P. Riola, R. D. Rundel and R. F. Stebbing, Phys. Rev. Lett. 29, 321 (1972).
13. T. R. Proctor and W. C. Stwalley, 1975 (private communication).
14. C. H. Chen, H. Haberland, and Y. T. Lee, J. Chem. Phys., 61, 3095 (1974).
15. N. Nakamura, J. Phys. B 8, L 489 (1975).
16. W. H. Miller, C. A. Slocomb, and H. F. Schaefer III, J. Chem. Phys. 56, 1347 (1972).

17. L. I. Schiff, Phys. Rev. 103, 443 (1956).

18. For detailed discussion of this approximation and related references, see R. B. Berstein, Advan. Chem. Phys. 10, p. 75 (1966).

19. R. E. Roberts and J. Ross, J. Chem. Phys. 52, 1464 (1970).

TABLE I

MMSV POTENTIAL PARAMETERS

ε(kcal/mole)	0.10
r_m(Å)	5.5
β_1	5.2
β_2	5.7
C_6 (kcal/mole $Å^6$)	3048
C_8 (kcal/mole $Å^8$)	63678
b_1	0.75
b_2	1.119
b_3	-2.755
b_4	1.984
X_1	0
X_2	1.12
X_3	1.75

FIGURE CAPTIONS - CHAPTER III

Fig. 1a Elastic differential cross section for He(2^3S) + Ar at 65 meV.

Fig. 1b Elastic differential cross section for He(2^3S) + Ar at 132 meV.

Fig. 2 MMSV potential obtained in this work (solid line); dash-dot curve depicts the corresponding imaginary part of the potential. For comparison, we have also plotted Olson's V_0[4] (dashed curve).

Fig. 3 Comparison of the calculated differential cross sections using the optical potential derived in this work (solid line), and the analytical potential proposed by Olson[4] with Illenberger's *coupling function*[2] *(dashed line)*.

Fig. 4 Comparison of our calculated total ionization cross section as a function of relative collision velocity with Illenberger and Niehaus's[2] experimental data (Δ).

Fig. 5 Comparison of our calculated total elastic cross section (Δ) with the experimental data of Rothe and Neynaber (X).

Fig. 6 Functional dependence of the associative ionization cross section on the parameter R_{AI} (see text).

Fig. 7 The ionic potential for He + Ar^+. Our data is only accurate up to 3.4 Å.

Fig. 8 Probability of chemi-ionization, i.e., Opacity as a function of the angular momentum ℓ. This is shown for five different collision energies.

Fig. 9 Dependence of the classical turning point on the angular momentum for various collision energies.

Fig. 10a Experimental differential cross section at 65 meV indiscriminately admits the two optical potentials shown in the figure. These potentials are different only in the slope of their repulsive wall and their respective imaginary component. Solid line corresponds to the case of $\beta_1 = 5.2$, $V_i^{OPT} = e^{-5.2934(r-3.55)}$; dashed curve corresponds to $\beta_1 = 4.5$, and $V_i = e^{-5.2934(r-3.35)}$.

Fig. 10b Theoretical total ionization cross sections vs. velocity using the two sets of $\{\beta_1, V_i\}$ in (a). The solid line is that of $\beta_1 = 5.2$, $V_i = e^{-5.2934(r-3.55)}$, and is in good agreement with the data of Illenberger and Niehaus, whereas the dashed curve is calculated from $\beta_1 = 4.5$, $V_i = e^{-5.2934\ (r-3.35)}$.

Fig. 11 Phase shifts ξ° are computed for the potential V_0 and compared with phase shifts $\xi + i\zeta$ for the cases of $V_0 - i\ V_i^{OPT}$, $V_0 - i(10V_i^{OPT})$, and $V_0 - i(100\ V_i^{OPT})$. The phase shifts are computed quantum mechanically by numerical integration (Numerov algorithm). The calculations were done for several partial waves. We have plotted $\Delta\xi = |\xi_\ell - \xi_\ell^\circ|$ vs. the opacity, which is $[1 - \exp(-4\zeta_\ell)]$. For the first order semiclassical approximation. One assumes $\Delta\zeta = 0$. ($\Delta\zeta$ is plotted in radians).

Fig. 12 Calculated differential cross sections, obtained by assuming a sharper resolution function for the detector, for the cases of V_i^{OPT} and $5\ V_i^{OPT}$. The curve for V_i^{OPT} is essentially identical to that obtained via a full quantum mechanical treatment. The curves for $5\ V_i^{OPT}$ are displaced to aid comparison, since the small angle oscillations are essentially identical for V_i and $5\ V_i$.

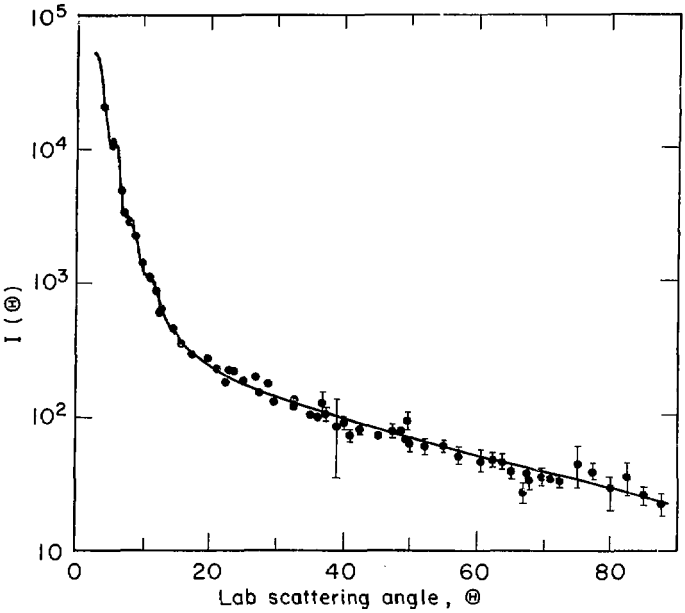
10^5
10^4
10^3
10^2
10
I (Θ)
0
20
40
60
80
Lab scattering angle, Θ
XBL762-5198

Fig. 1a

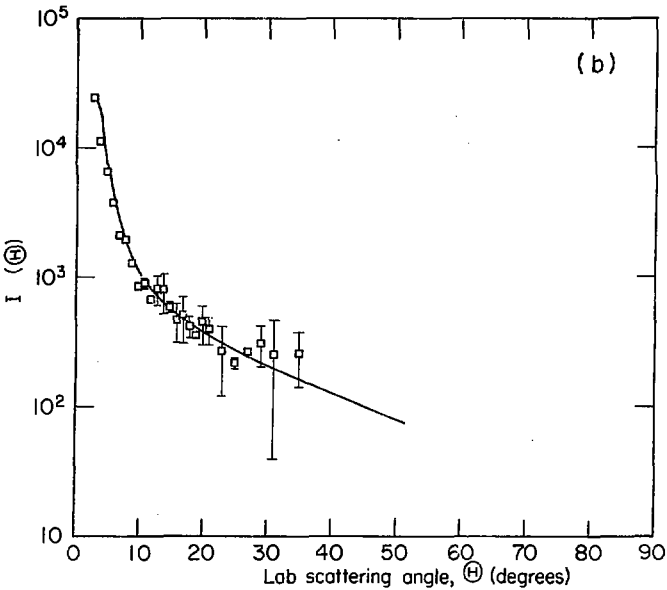

Fig. 1b

XBL 762-2206

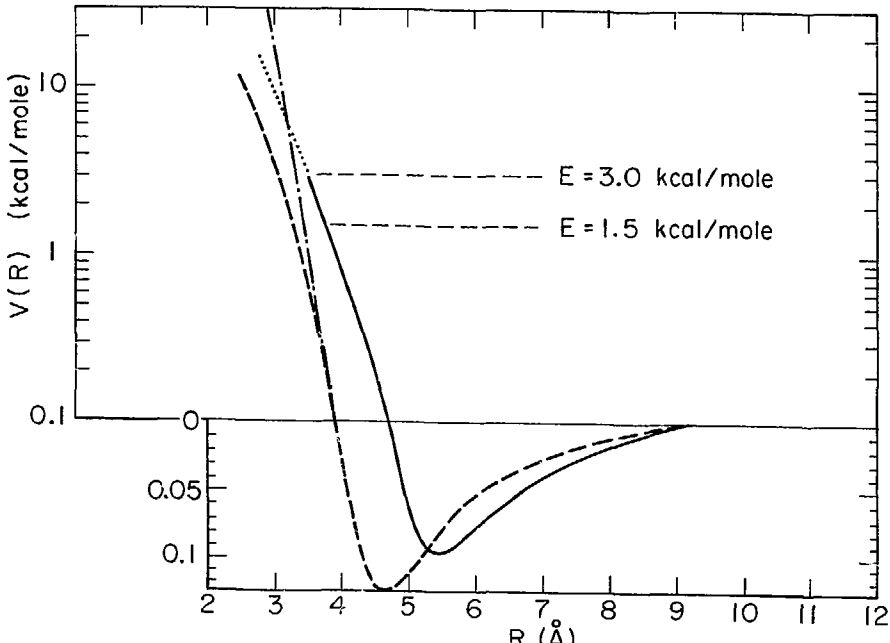

Fig. 2

NBL 762-2209

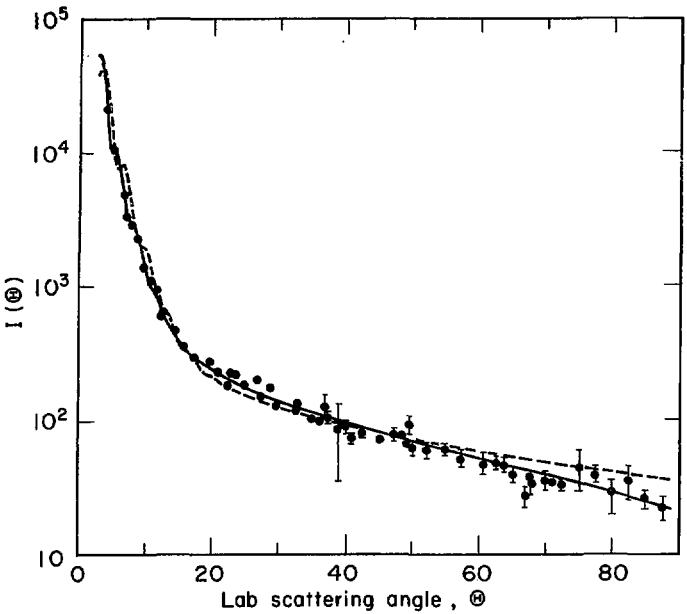
10^5
10^4
10^3
10^2
10
I (Θ)
0
20
40
60
80
Lab scattering angle , Θ
XBL762-5199

Fig. 3

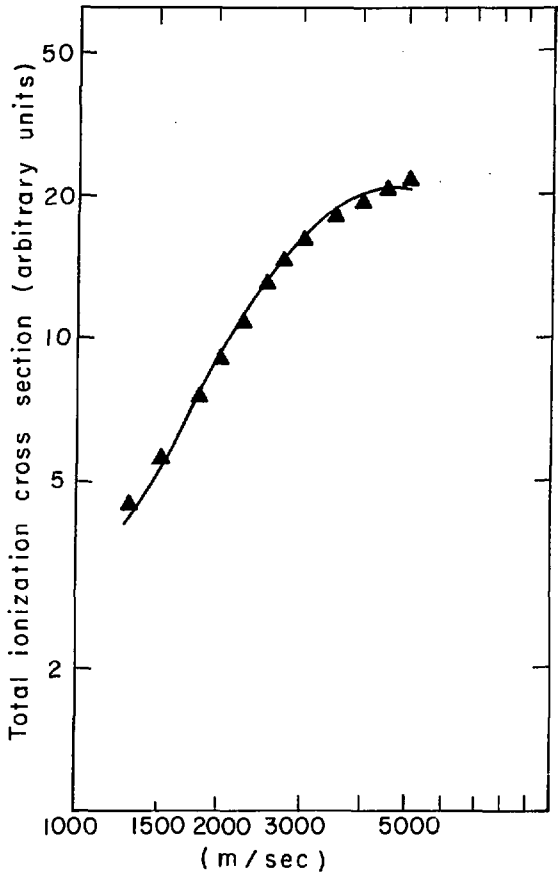

XBL 762-2201

Fig. 4

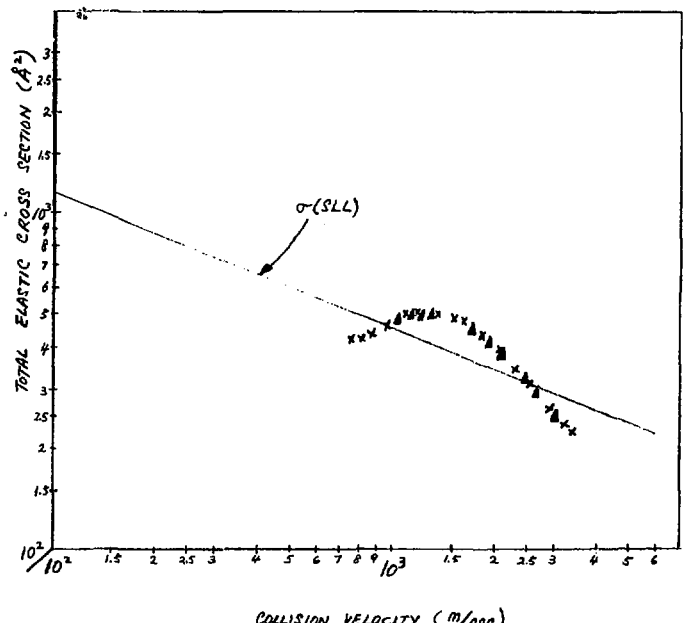

Fig. 5

XBL 7710-10239

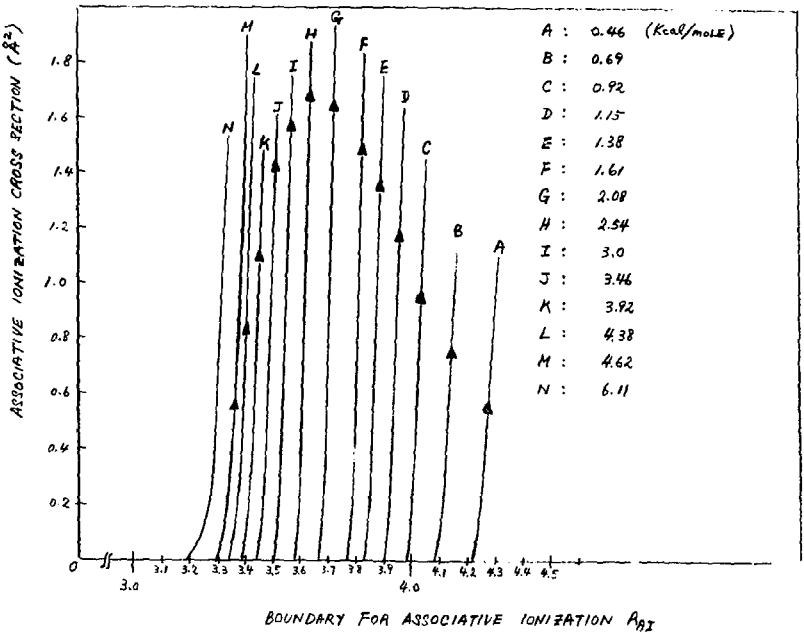

Fig. 6

XBL 7710-6798

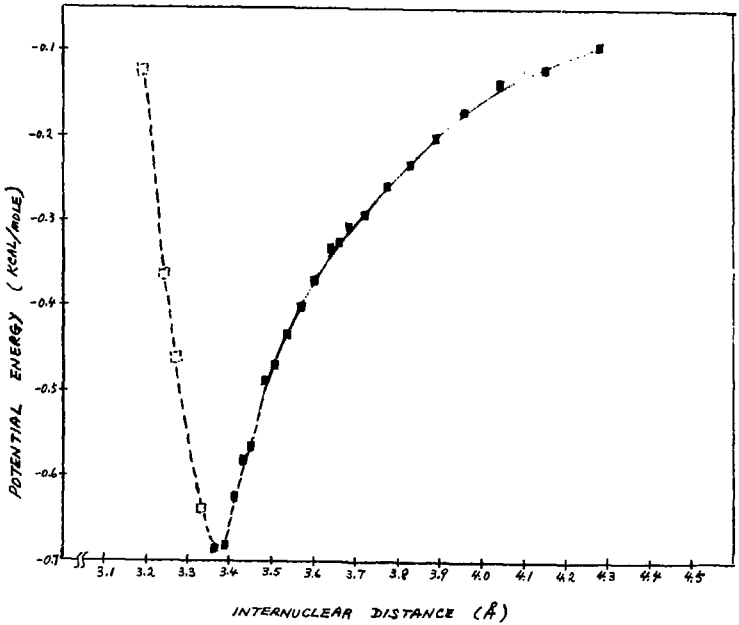

Fig. 7

XBL 7710-6797

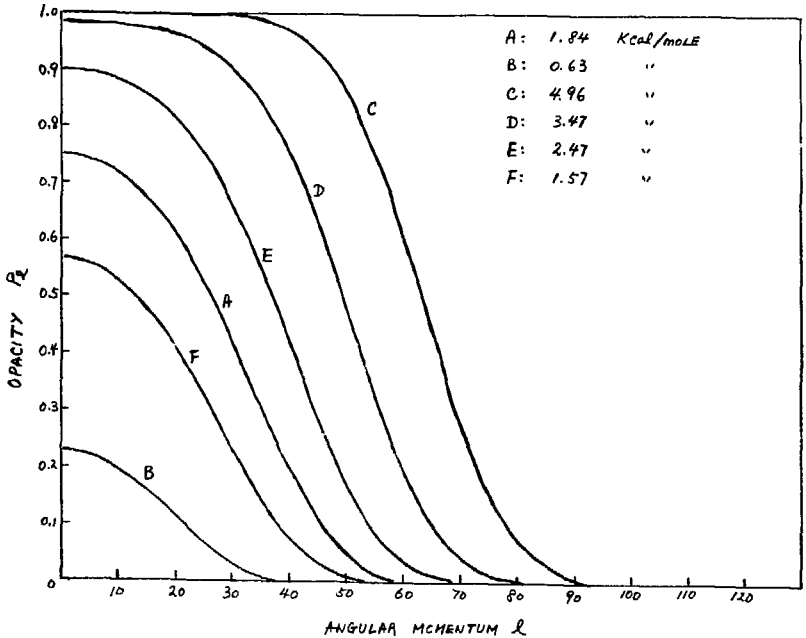

Fig. 8

XBL 7710-6785

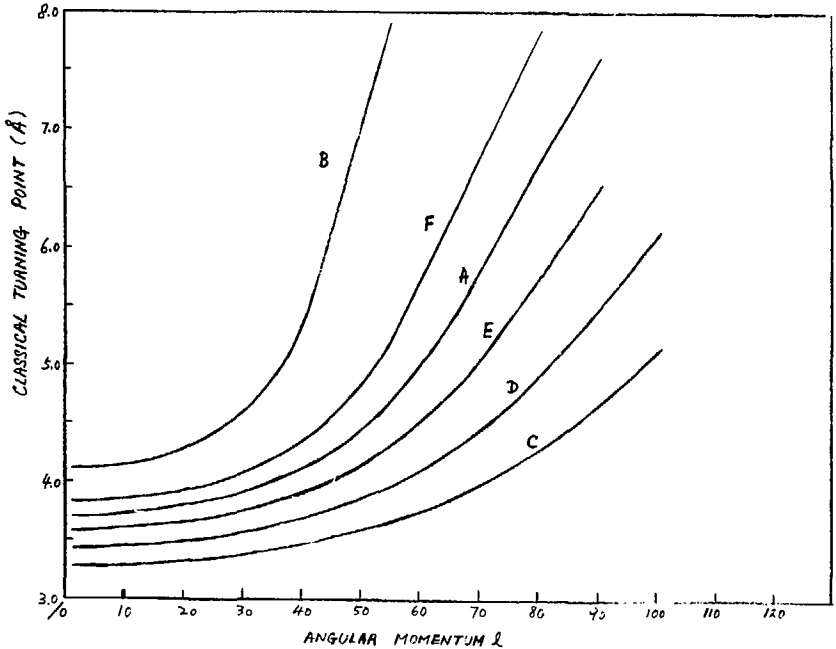

XBL 7710-6782

Fig. 9

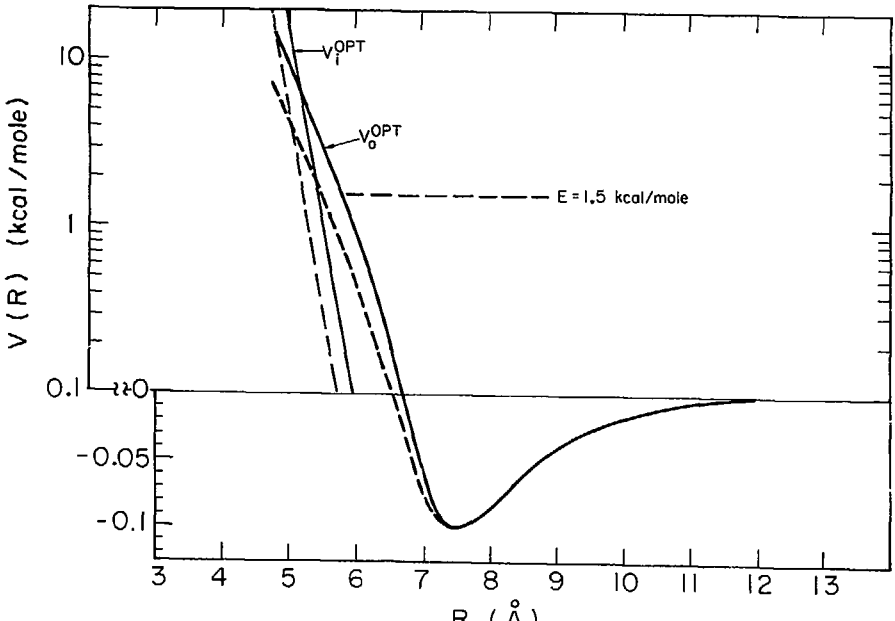

Fig. 10a

XBL 762-2210

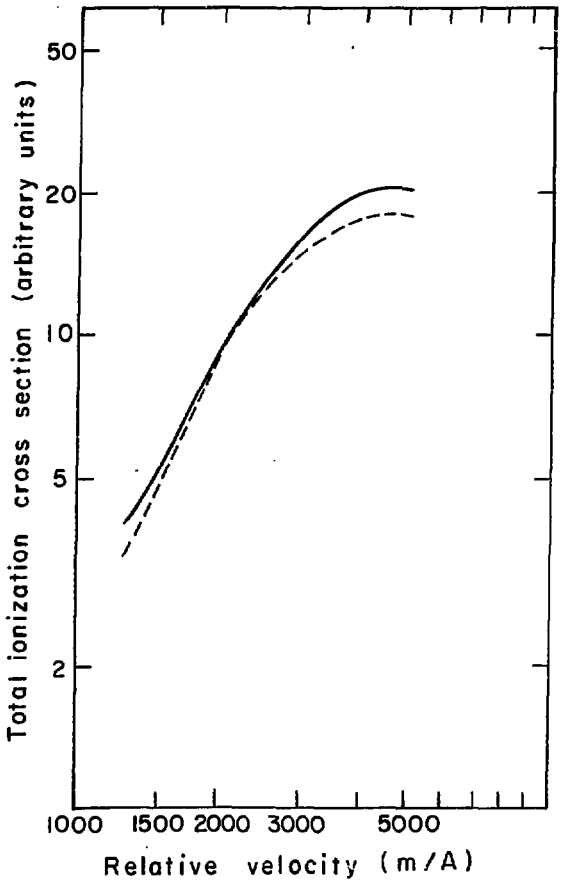

Fig. 10b

XBL 762-2202

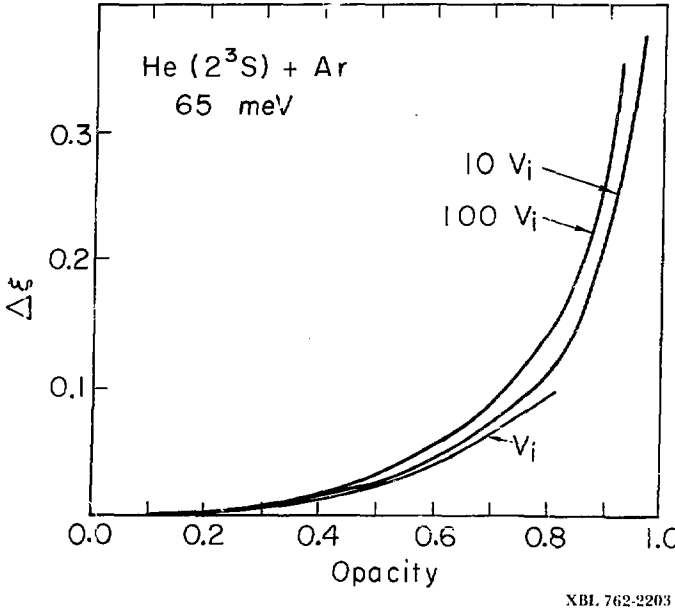

XBL 762-2203

Fig. 11

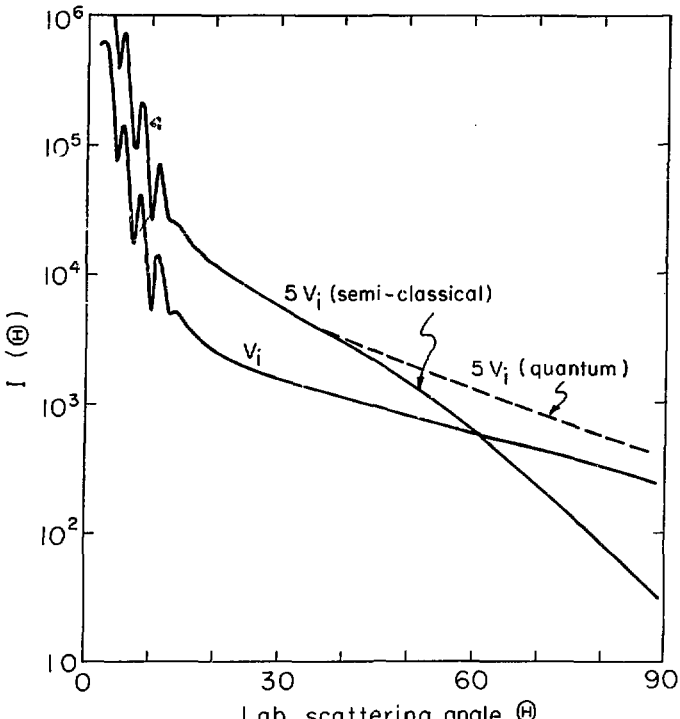

Fig. 12

XBL 762-2208

IV. THE INTERACTIONS OF $He(2^1S) + D_2$, AND $He(2^3S) + D_2$

A. Introduction

The interaction between helium metastable atoms and hydrogen molecules provides the simplest example of chemi-ionization involving a molecular target. The participation of a molecule as the quenching agent in the Penning ionization process is quite unlike that of an atom in several significant regards. First, the forces which characterize the interaction between two atoms are generally radial in nature, i.e. isotropic. Such symmetry is in principle absent in an atom-molecule system which necessarily interacts on a potential which is anisotropic (though the anisotropy can be quite small in some instances). This angular dependence in the potential, in the language of molecular scattering, means that for the same impact parameter (i.e. the same orbital angular momentum), dramatically different interaction potentials as well as classical turning points are possible--depending on the angle of approach of the two colliding particles.

The second noteworthy feature about an atom-molecule Penning ionization system is that the molecule can suffer dissociation in the process of being ionized by the metastable atom. We have already established earlier that if no significant bonding occurs before any transferal of electron takes place, the process whereby the target molecule is ionized is Franck-Condon like. Thus if the molecule's covalent potential energy curve is sufficiently different from its corresponding ionic curve, the resultant molecular ion will be formed in some highly excited vib-rot states from which it can undergo dissociation. Hence, apart from the usual associative and Penning ions, Penning ionization of a molecule can give rise to other interesting ionic species.

The third important difference between metastable atom-atom and metastable atom-molecule interaction is that in the latter case, even when the excess energy of the metastable atom is lower than the ionization potential of its collision partner so that Penning ionization is out of the question, the excited atom can still be quenched.** The molecular target, by virtue of it having many more internal degrees of freedom than an atom, can take up the metastable's surplus electronic energy in the form of vibrational and rotational quanta. Indeed, the relative abundance of energy sinks in a molecule would also enable the collision energy in the reaction to be likewise channelled to exciting the molecule internally. One consequence of this is that the energy dependence in the total ionization cross section needs no longer yield to a straight forward interpretation.

We see therefore that in studying the interaction of a metastable atom with a molecular target, we venture into much hitherto unchartered terrain. In this voyage, $He^* + H_2$ represents the simplest four-electron system which is tractable to attack at a fundamental level both theoretically and experimentally. It thus affords an excellent testing ground for more complex intermolecular force problems, and has accordingly attracted a good deal of attention.

Previous experimental studies of this system can be classified into a few broad categories according to the particular technique used. The first group employed the crossed-molecular beam method. Hotop and Niehaus[1]

** While electronic energy transfer without ionization is certainly possible between atomic collision pairs--He-Ne being the best known example--such processes, however, require very precise mutual matching of energy levels, and therefore are in general not very probable among dissimilar atoms.

in 1968, using essentially thermal beams--their metastable beam was a mixture of $He(2^1S)$ and $He(2^3S)$ atoms of undetermined composition--measured the relative cross section for the production of the various possible ions resulting from Penning ionization, namely H_2^+, HeH_2^+ and HeH^+. A ratio of 9.1:0.2:1.0 was found. Hotop, Niehuas and Schmeltekopf[2] in a subsequent experiment separated out the contribution of the singlet and the triplet metastable atom; they found that the ratio of the singlet to triplet cross section with respect to the formation of the ions H_2^+ and HeH^+ were quite close to unity. From this they concluded that Penning ionization was primarily dominated by an electron exchange mechanism. Hotop and Niehaus[3], in another experiment, also undertook to measure the Penning electron energy distribution for $He(2^3S) + H_2$. Such a study was necessary to further one's understanding of the ionization process. If in the course of collision, a quasimolecule in the superexcited stae, HeH_2^{**}, was formed, which then autoionizes, a different spectrum would be observed than in the case of H_2 being ionized while the separation of the collision partners was still relatively large. (In the latter case, the different ionic species would arise essentially from reactions of H_2^+ in certain vibrational states with He in its ground states. When Hotop and Niehaus compared their Penning electron spectrum with the corresponding photoelectron spectrum obtained by photoionizing H_2 with the resonance radiation He(2p → 1s; 584 Å), they found that while the population of electronic states of the molecular ions is quite different for the two methods of ionization, the relative population of vibrational states in each electronic state is very nearly equal. This result is additional and complementary confirmation

of the statement that the potential curves of the molecule and the molecular ion at the instant of ionization are hardly perturbed by the collision; to wit, Penning ionization of H_2 by $He(2^3S)$ is a Franck-Condon process.

In another crossed-molecular beam study, Leu and Siska[4] monitored the angular distribution of the H_2^+ ions formed in $He(2^1S)$ colliding with H_2. They found that the Penning ions sharply peaked in the forward direction (in the direction of the H_2 molecule) with substantial kinetic energy loss. Leu and Siska postulated that the dominant ionizing collisions were ones in which the collision partners were on the downhill side of a barrier when ionization occured; furthermore, the latter process landed the particles on the attractive portion of the $He\text{-}H_2^+$ potential.

Other crossed-molecular beam studies include that of Howard et al.[5] who measured the absolute total cross section for ionization in thermal energy collisions of $He(2^1S)$ and $He(2^3S)$ with H_2. They found a cross section for the singlet metastable to be 3.0 A^2(± 20%), and that for the triplet, 3.4 A^2(± 20%). Subsequently, West et al.[6] from the same laboratory obtained the branching ratio for the formation of various ions. Their experiment was carried out at an effective temperature of 600° K; they obtained for the ions H_2^+, HeH^+, H^+ and HeH_2^+ a relative production ratio of 0.85:0.1:0.022:0.026 (both spin states of the metastable atom yielded the same result).

Instead of crossing the molecular beams as in all the aforementioned experiments, Neynaber et al.[7] used the technique of merging beams to study the formation of HeH^+ ions. They found that at collision energies below 4 eV, much of the HeH^+ were scattered in the direction of the helium

metastable beam (the beam used here was a mixture of He(2^1S), He(2^3S) and He(1S) in the ratio of 1:12:3). Since this was highly indicative of a spectator-stripping mechanism, Neynaber et al. assumed the validity of such a picture and calcualted the relative kinetic energy of the product species HeH^+ and H (not including the energy of the ejected electron) as a function of the interaction energy; very good agreement with experimental results was obtained. Neynaber et al. also sought to secure more direct experimental support for Hotop and Niehaus's model for the ionization process (vide supra) by studying the reaction $He + H_2^{+X} \longrightarrow HeH^+ + H$, where χ denotes ground state or vibrationally excited H_2^+. If the electron is indeed ejected before any significant bonding occurs, then one would expect the energy distribution of the HeH^+ ion from the ionic reaction to be similar to that obtained for the metastable reaction $He^* + H_2 \longrightarrow HeH^+ + H$. This expectation was found to be experimentally borne out only for interaction energies less than 1.5 eV; the two distributions at higher energies were quite different. Neynaber et al. concluded that at the higher energies there should be a reasonable degree of bonding in the $He^* - H_2$ complex before ionization took place, so that Hotop and Niehaus's model was no longer applicable. It must however be cautioned that in Hotop and Niehaus's experiment, the metastable He atoms collided with H_2 molecules in the ground electronic, ground vibrational and low rotational states; by contrast, in the experiment of Neynaber et al., the H_2 beam was in an unknown state of vibrational excitation. Since the precise role played by the presence of excess vibrational energy in the ionization process is not entirely clear, one may not be able to make direct comparisons between the results obtained by these two groups: Hotop and Niehaus, and Neynaber et al.

In any event, a rather different model for the ionization process was proposed by Penton and Muschlitz.[8] They measured relative reaction cross sections using a thermal beam of $He(2^3S)$ and $He(2^1S)$ atoms (in ratio of 0.9:0.1) in a beam-gas set-up. They ran the same measurements for three different target gases, H_2, HD and D_2, and found that the cross section for the production of H_2^+, HD^+ and D_2^+ increased in this order. They concluded that a plausible explanation for this isotope "shift" lay in the formation of a highly excited collision complex $(HeH_2)^*$ which could subsequently follow two modes of decomposition:

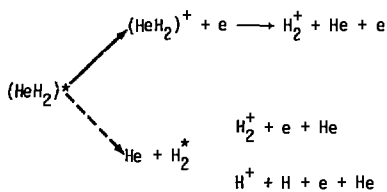

Another beam-gas study on helium metastable atoms interacting with hydrogen molecules and its isotopes was recently carried out by Specht et al.[9] Apart from obtaining the branching ratios for the various ions, Specht et al. were particularly interested in the production of HeH^+ and HeD^+ in the reaction $He^* + HD$ at thermal energies (their He^* beam was again composed of a mixture of the two spin states of the metastable atom in the ratio of 2:1, (singlet):(triplet). It was found that the ratio of these two ions was the same as that obtained from the corresponding ion-molecule reaction $HD^+ + He$. Specht et al. felt that this observation lent strength to Hotop and Niehaus's model for the ionization process.

In addition to all the beam-related studies discussed above, a number of other groups have, without the use of beams, performed measurements on the system He* + H_2. Schmeltekopf and Fehsenfeld[10], in a flowing afterglow apparatus under thermal conditions, measured the quenching rate constant for the reactions He(2^1S) + D_2, H_2 and He(2^3S) + D_2, H_2. They found that in all cases, the singlet is quenched at a higher rate than the triplet (for D_2, singlet rate is 4.15 x 10^{-11} cm^3/sec, and the triplet rate is 2.6 x 10^{-11} cm^3/sec; for H_2, singlet rate is 4.88 x 10^{-11} cm^3/sec, and triplet rate is 3.18 x 10^{-11} cm^3/sec). In a later study carried out by the same laboratory, Lindinger et al.[11] obtained the temperature dependence of the rate constant for He(2^3S) + H_2. A very strong temperature dependence was observed for this reaction. This was a very important experimental discovery, and not anticipated by theoretical models at that time. It served to explain why previous measurements at room temperature of the ratio of singlet to triplet ionization cross sections by the flowing afterglow method were always larger by a factor of about three than those obtained via the beam technique. It turned out that in the beam set-up, the relative velocity distributions of the beams corresponded to an effective temperature much higher than 300° K.[19] Lindinger et al. found that their measured cross sections at 800° K were in much better agreement with the beam results than those taken at 300° K.[5] Bolden et al.[12], also in a flowing afterglow set-up, measured the ionization cross section for He(2^3S) + H_2 at thermal energies (strangely) with respect to the channels He* + H_2 → H_2^+ + He, and He* + H_2 → H^+ + H + He. They obtained a value of 1.5 A^2. Veatch and Oskam[13], by monitoring the time behavior of the ions H_2^+ and HeH^+ in the afterglow of a He + H_2

mixture which had been subjected to a high voltage dc pulse, obtained a rate constant of 5.2×10^{-11} cm^3/ sec (~1 $Å^2$) for the ionization process under thermal conditions.

Despite the seeming plethora of experimental data--rate constants, total ionization cross sections, branching ratios for the formation of different ionic products, and ratio of singlet to triplet metastable ionization cross sections--on He* + D_2/H_2, it must be pointed out that the general utility of these measurements are of a corroborative, as opposed to deterministic, nature. That is to say, they cannot by themselves reveal much about the fundamental physical parameters which govern the chemi-ionization process. For these, one must again turn to elastic differential cross section measurements which, as argued previously, do reflect in a much more direct and straight forward way the nature and shape of the interaction potential involved. We do not, however, wish to suggest that scattering experiments alone hold the key to all the answers, and that other types of experiments are of lesser importance. Indeed, we hasten to re-emphasize, as we have done in Chapter III, that results from the former technique must be conjoined, in a complementary sense, with those from the latter in determining the uniqueness and accuracy of a given model potential. The primary advantage of elastic differential cross section data is that they can, if analysed carefully, start us off with a good approximate potential, on which further refinements can be made to zero in on Nature's own choice. This is the approach we take in our laboratory. But before we report our work on He* + D_2, it is instructive to survey the efforts made on the theoretical front towards understanding this important system.

Cohen and Lane[14] in early 1977 reported the first theoretical interaction potential energy surfaces and widths for both He(2^3S) and He(2^1S) atoms with H_2. Aside from the relatively shallow van der Waals minima at large He* + H_2 separations, the potential curves for all orientations regardless of the spin state of the metastable He were found to be repulsive. Moreover, for He(2^3S) + H_2, the higher order expansion terms for the potential as well as the ionization width (which terms contain the angular dependence) were seen to be small as compared to the zero-order angular-independent term, i.e., the anisotropy is only very slight. From this, one would expect that the ionization cross section calculated from an orientation averaged potential curve (the spherical potential approximation) should approximate quite well that obtained by averaging the cross sections calculated from different orientations (the infinite-order sudden approximation). This was indeed what Cohen and Lane concluded as they calculated the ionization cross section covering the range of relative energies 0-10 eV. The ratio of singlet to triplet ionization cross section in that energy range is found to be less than one at low energies, but rises quickly to reach unity at 65 meV. It finally peaks to a value of 2.6 at 100 meV. Since the calculated ionization width for the singlet metastable state deviates only slightly from that of the triplet state, the observed dramatic energy dependence in the ratio of the two cross sections must be attributed to dissimilarities that lie in the respective real potential. The singlet surface is the more repulsive of the two at $R > 3.7$ Å, while the triplet is more repulsive for $R \leq 3.7$ Å. The potential energy where the two surfaces cross is essentially the same as the relative kinetic energy at which σ_S begins to exceed σ_T (at around 70 meV).

Prior to the above study, Preston and Cohen[15] calculated the total cross section and branching ratios for the various ionic channels as a function of the collision energy (0 to 0.7 eV). Their theoretical treatment of the ionization process was an extension of the trajectory-surface-hopping model. In this framework, a classical trajectory begins on the excited state potential. At each step in the trajectory, the probability P(R) of leaking into the continuum is computed by Miller's semiclassical formula, and compared to a pseudorandom number ζ. If $P(R) \leq \zeta$, the trajectory continues on the resonant surface; however, if $P(R) > \zeta$, the electron leaks into the continuum, and the nuclei make a vertical transition to the lower ionic surface. If ionization occurs, the trajectory follows the lower surface to one of the possible chemi-ionization channels. Preston and Cohen's calculated branching ratios based on the above treatment agree surprisingly well with the experimental data of Hotop and Niehaus.

Quite recently, Hickman et al.[16], using a method based on Feshbach projection operators, have recalculated from scratch the $He(2^3S) + H_2$ potential surface and width. Compared to those obtained by Cohen and Lane, the real part of Hickman's potential is slightly more repulsive--it is however shifted in by about 0.4 Å--the corresponding ionization width is also smaller. Hickman et al., in a different report[17], performed quantum mechanical scattering calculations within the rigid-rotor approximation for $He(2^3S) + H_2$ using their own theoretical potentials. They obtained the elastic differential cross section as well as the total ionization cross section in the energy range 0.01 to 0.5 eV. The energy dependence of the rate constants calculated from these values for the ionization cross section differes, however, from the experimental results

of Lindinger et al. In a subsequent publication by the same group, Isaacson et al.[20] extended their large scale configuration interaction calculations to obtain also the interaction potential for singlet metastable helium and hydrogen molecules. They found that the singlet surface, unlike its triplet counterpart, is highly anisotropic. Moreover, a fairly pronounced relative maximum is found in the potential for the C_{2v} (i.e. perpendicular) configuration at 3.17 Å. Isaacson et al. have tentatively assigned this surprising hump to be the result of an induced s-p hybridization of the helium atomic orbitals by the H_2 molecule as the two colliding partners come into very close vicinity of each other. However, since the same phenonenon should occur with equal ease for the co-linear geometry, yet nothing unusual can be seen in the C_∞ co-linear potential curve, the hybridization explanation should at best be regarded as being only part of the whole truth, and further qualifications are definitely in order.

From the above discussion we see that while theoretical calculations on the system He* + H_2 have indeed added significantly to our qualitative understanding of the important parameters governing the Penning ionization process, in terms of quantitative reliability however, all the ab initio potentials thus far proposed still leave something to be desired. Large scale CI calculations are inherently self-limiting in the sense that as more basis sets are included for higher accuracy, the cost of running the resulting computer program becomes prohibatively expensive. Thus current theoretical efforts are directed towards finding alternative ways to either supplement or even replace the more traditional computational methods.

In our laboratory, we have undertaken to measure the elastic differential cross section for both $He(2^3S) + H_2$ and $He(2^1S) + H_2$. As argued before, such measurements constitute probably the most direct experimental means available to us at present to extract detailed information about the interaction potential. We have also measured, at several energies, the relative cross sections for the production of the three principal ions, HeH_2^+, HeH^+, and H_2^+, stemming from the ionization process. In the case of $He(2^3S) + H_2$, a best-fit potential was found which reproduced quite well the rate constant results of Lindinger et al. as well as our own relative cross section data.

Before discussing the analysis of our data, two supplementary comments are in order.

(i) In a strict sense, all the measurable properties that arise from the $He^* + H_2$ interaction depend of course on the full, angularly dependent potential $V(R,\theta)$ and width $\Gamma(R,\theta)$. However--with respect to $He(2^3S) + H_2$--since the anisotropy that exists is extremely small, our scattering measurements, to a very high degree of accuracy, can be interpreted as reflecting only the spherically symmetric parts of the potential and its accompanying width, denoted V_0 and Γ_0 respectively. Moreover, under our experimental conditions, only the highly symmetrical lowest rotational states of H_2 are appreciably populated; and, given the wide rotational spacings in H_2, the cross section for rotational spacings in H_2, the cross section for rotational excitation is very small for the range of relative kinetic energy used in our study.

We are thus afforded a separate determination of V_0 and Γ_0, the angular-independent component of the interaction potential and its ionization width; this should prove useful in sharpening the interpretation of data that do depend significantly on the higher order anisotropic terms.

In the case of $He(2^1S) + H_2$, the situation is much more complicated. Here it is believed that the interaction potential is very anisotropic, thus rotational excitation is quite probable even for low collision energies. Elastic differential cross section measurements on the singlet system will therefore not be as informative as those for the triplet; analysis of the data will certainly not be straight-forward. Indeed, one should secure the corresponding inelastic differential cross sections in order to fully understand as well as to quantify the extent of the anisotropy that is present.

(ii) We have used D_2 instead of H_2 in all our differential cross section measurements because the former results in a much wider range of measurable angles in the laboratory frame. This is made evident in Fig. 1 where we have drawn the respective Newton diagram for D_2 and H_2. Recalling that we are only monitoring the intensity of the helium metastable atoms as a function of laboratory angles, we see that since H_2 has only half the mass of He, the center of mass vector would be biased towards He, resulting in a shrinking of the available angular scanning range for He*. The use of D_2 is therefore much more informative in this regard.

B. Results and Discussion for $He(2^3S) + D_2$

We have measured the elstic differential cross section for the system $He(2^3S) + D_2$ at three coilision energies, 1.02 Kcal/mole, 1.73 kcal/mole and 2.6 kcal/mole. These are shown, along with their calculated counterpart, in Fig. 2, Fig. 3 and Fig. 4. The theoretical fit is based on a potential of the MMSV form:

$$f(x) = \exp[-2\beta_1(x-1)] - 2\exp[-\beta_1(x-1)] \qquad x_1 < x \leqslant 1$$

$$f(x) = \exp[-2\beta_2(x-1)] - 2\exp[-\beta_2(x-1)] \qquad 1 < x \leqslant x_2$$

$$f(x) = b_1 + (x-x_2)\{b_2 + (x-x_3)[b_3 + (x-x_2)b_4]\} \qquad x_2 < x \leqslant x_3$$

$$f(x) = -c_6 x^{-6} - c_8 x^{-8}$$

where

$$f(x) = \frac{V(R)}{\epsilon} \; ; \quad x = \frac{r}{r_m} \; ; \quad c_n = \frac{C_n}{\epsilon r_m^n}$$

The values for the various parameters defining our best-fit potential are tabulated in Table I.

We note that at the lowest collision energy probed, approximately three peaks are resolved in the small angle region of the differential cross section. The position and relative intensity of these peaks are extremely sensitive to the well region and long range part of the potential; thus their faithful reproduction by our proposed potential gives us much confidence in the latter's reliability. The imaginary part of the potential is assumed to have the form

$$V_i(R) = \exp\left[-B(R-R_0)\right] \quad \text{(in kcal/mole, R in Å)}$$

with the values of B and R_0 given also in Table I. We have plotted our potential, both its real and imaginary component, in Fig. 5. When we compare this potential with those derived theoretically by the two groups Hickman et al., and Cohen and Lane, we observe significant differences. The respective slopes of the three potentials are shown in Fig. 6. We see clearly that our potential has a much steeper wall; it is therefore not surprising that our best-fit ionization width is also much greater than those obtained theoretically. The widths are plotted in Fig. 7. Since neither Hickman et al. nor Coehn and Lane has extended their calculations sufficiently to take into account the van der Waals minimum

in the potential*, comparisons between the theoretical differential cross sections calculated from these two potentials with our experimental data is only meaningful in the large angle region. We have splined our best-fit van der Waals minimum to their repulsive walls to compare the resulting differential cross sections. We found that both theoretical potentials give differential cross sections which are too high. This can be attributed mainly to the corresponding calculated ionization widths; they are too small.

C. $He(2^1S) + D_2$, a Comparison Study

For $He(2^3S) + D_2$, our measurements show that the fall-off at large angles in the metastable intensity is very gradual; this implies a smooth coupling between the potential's real and imaginary part. A marked contrast is found in the differential cross section data for $He(2^1S) + D_2$. We have again scanned this for three energies: 1.02 kcal/mole, 1.73 kcal/mole and 2.6 kcal/mole. They are plotted respectively in Fig. 8, 9 and 10. The most striking thing we immediately notice is that at the two higher energies, there is a very distinct discontinuity

* This is in part due to the fact that CI calculations are simply not designed to get at van der Waals minima. Even for a relatively simple four-electrons systems such as He-He, in order for bound state type CI calculations to reproduce accurately the van der Waals minimum, f-type functions have to be included in the basis set. Thus the situation gets totally out of hand, computation-time (and cost-wise), for systems with more lectrons. Beside, the available experimental data on $He^* + H_2$--at the time when these works were done--were confined to rate constants and ionization cross sections only. These latter properties of the system depend largely on the interplay between the repulsive wall of the potential and Γ, the ionization width. The van der Waals minimum exerts little, if any, influence at all.

in the metastable intensity. Indeed, we have failed to secure a spherically symmetric potential which can reproduce this feature in the differential cross section. Haberland and co-workers[18], having recently also studied this system, found that the only way they could have a good and self-consistant fit to their differential cross section data, which spanned a fairly extensive range of energies, was to introduce an anomalous hump in the repulsive wall--while keeping a simple exponential function for the ionization width. This would seem to be in accord with what Isaacson, Hickman and Miller[20] have concluded from their theoretical investigation. However, as noted before (vide supra), the latter group only found a hump for the C_{2v} configuration, and it is shifted quite in relation to the repulsive wall of the C_{∞} potential which has a monotonic slope. It is therefore not entirely clear what a spherically averaged representation of such an anisotropic potential would look like; moreover, whether it bears any direct simple relation to the effective spherically symmetric potential obtained by Haberland et al. In the very recent work of Siska et al.[21], we are given another perspective to view this anomalous hump. Siska et al. have measured the elastic differential cross section for He(2^1S) + Ar. They found that they could fit their data very well by splinning two distinctly different potentials together: for the inner segment, they used the potential for He^+ + Ar, and for the outer segment, the Li + Ar potential. The good fit was explained by proposing that there are in reality two separate repulsive regions. There is firstly an outer electron-electron repulsion at larger internuclear separations were the metastable helium atom looks very much like a lithium atom; then as the

collision partners get closer, s-p hybridization of the helium atomic orbitals would permit access to the inner repulsive wall where the metastable helium appears like He^+. Whether this same approach can be used for $He(2^1S) + D_2$ is yet to be fully investigated. We note in passing here that our differential cross sections for $He(2^1S)$ and $He(2^3S)$ at the lowest collision energy (1.02 kcal/mole) are nearly identical. This is very strong evidence that the respective van der Waals wells, down to 4.5 Å, are similar for the two metastable states.

D. Rate Constants

Lindinger et al. is the only group which has measured the rate constant k(T) for $He(2^3S) + H_2$ over a sufficiently wide range of temperatures. We want to note that this is a macroscopic property of the interacting system; indeed, it is a highly averaged representation of the more fundamental total ionization cross section $\sigma(v)$ (v is the relative collision velocity) which is more intimately related to the interaction potential. k(T) is linked to $\sigma(v)$ via

$$k(T) = \langle v\sigma(v) \rangle = \int_0^\infty f(v)\ v\sigma(v)\ dv \qquad (1)$$

where

$$f(v) \equiv \text{Maxwellian Velocity Distribution} = \frac{4}{\sqrt{\pi}} \left(\frac{m}{2kt}\right)^{3/2} v^2 e^{-\frac{mv^2}{kT}}$$

From Eq. (1), it is clear that agreement with the experimental values for the rate constant is but a necessary condition for any proposed potential for $He(2^3S) + H_2$; it, however, is by no means sufficient. Since a number of different potentials can give the same fit to the experimental rate constant's curve, we are only justified to use the latter to rule out models for the potential which disagree with it, and conversely, can only use whatever agreement that does exist as merely indirect corrobative evidence for our model potentials's accuracy. Seen in this light, the theoretical potential as calculated by Hickman et al. is definitely wrong. The rate constants generated from it are about a factor of 2 smaller than the corresponding experimental data points of Lindinger et al. along with their uncertainties*, also shown are the rate constant results as calculated from Hickman's et al. (broken line).

E. Branching ratios of Ionic Products

For both $He(2^1S) + D_2$ and $He(2^3S) + D_2$, we have measured the relative intensities for the three principle ions HeD_2^+, HeD^+ and D_2^+ at four collision energies: 1.02, 1.73, 2.0, and 2.6 (kcal/mole).** Table II compares our branching ratios at 1.73 kcal/mole with those obtained by

---

* Lindinger et al. used H_2 as opposed to our D_2 in their measurements. However, from a previous study by the same group, it was shown that the rate constant for the two isotopes are the same within experimental error.

** In the mass spectrometer, we are of course not able to distinguish between He^+ and D_2^+ which have the same mass. Thus to ensure that the counts we got for D_2^+ were not in part due to the ionization of highly excited helium atoms (in their Rydberg states), we repeated the same measurements using H_2 as the quenching agent. We found that the branching ratios remain the same within experimental uncertainties.

other groups. We see that our results for the singlet metastable case differ significantly from all the other measurements; they are also quite different from the corresponding triplet case.

The ratio of the singlet to triplet cross section with respect to the various ions reveals some interesting features. We see that while the singlet cross section is much less than the triplet cross section for the production of D_2^+, the converse is true for HeD^+ and HeD_2^+ formation. The exact ratios are tabulated in Table III for the four collision energies, and in Fig. 12, we show that the energy dependence of the formation of the three ions. Also included in Table III are the singlet-to-triplet cross section ratios determined by other groups. We observed that with the exception of the flowing afterglow result, all the ratios are less than unity. The disagreement with the flowing afterglow data has been partially explained by Cohen and Lane in their theoretical work. They have shown that the ratio of singlet to triplet cross section calculated from the same set of potentials depends heavily on the velocity distribution assumed in the reactants. Fig. 13, which is taken from Cohen and Lane's paper, shows this very clearly.

F. The Total Ionization and Elastic Cross Section

Experimental measurements of the total ionization cross section for $He(2^3D) + D_2$ to date are unfortunately all confined to a very limited energy range. Meaningful comparisons between our calculated energy dependence in the ionization cross section with experimental data is therefore not possible. Nonetheless, we have, in Fig. 14, scaled the four relative cross section data points we have obtained to the theoretical

cross section curve from our proposed potential. Good agreement is found. On the same graph are shown the results of Preston and Cohen--similarly scaled.

We have also calculated the total elastic cross section as a function of the collision energy. This is shown in Fig. 15. We see that after a relatively sharp initial fall-off, the elastic cross section decreases very gradually as the collision energy increases. Since the ionization cross section also saturates at higher energies, one would expect a fairly constant ratio of ionization/elastic cross section over a substantial energy span.

G. Opacities and Classical Turning Points

We have plotted the probability of ionization as a function of the angular momentum for several energies in Fig. 16. We see the usual saturation effect at small angular momenta. We also note that even at a collision energy of 3 kcal/mole, the highest opacity is still less than 0.95. Thus we would expect the first-order semiclassical approximation for the phase shift employed in our analysis to be quite good.

In Fig. 17 we show the classical turning points as a function of the angular momentum for the same collision energies as in Fig. 16. In all cases, the classical turning points would remain fairly constant for angular momenta values less than 12; this again is a reflection of the steepness of the interaction potential's repulsive wall.

H. Conclusion

Many questions remain begging with regard to the Penning ionization reactions $He(2^3S) + D_2$ and $He(2^1S) + D_2$. For the former, the availability of an accurate potential, as what we have deduced from our scattering data, should greatly aid in the interpretation of future measurements on this system. In the case of the latter singlet reaction, however, the interaction potential is still to be determined. Differential cross section measurements by themselves are definitely not equal to this task as rotational excitation can be quite important in this singlet metastable system. Since the latter process becomes most probable at small impact parameters (corresponding to large angle scattering), interpretation of the large angle region of the differential cross section cannot be done just in terms of the interplay of spherically symmetric real and imaginary potentials. It would be necessary to have measurements of the total ionization cross section over a wide range of energies in order to separate out the contribution of the ionization width from that caused by whatever anisotropy that exists in the real part of the potential. Inelastic differential cross section measurements are also needed to determine the extent of rotational excitation of the D_2 molecule in the collision process.

In terms of reaction dynamics--for the triplet metastable case--the evidence at the moment is in definite favor of the idea that ionization of the quencher occurs before there is any significant bonding with the metastable atom. Furthermore, by plotting the reaction probability vs. the classical turning point for various collision energies as we have done

in Fig. 18, it is readily seen that, to a good approximation and for the energy range considered, the reaction probability is independent of the collision energy for a given classical turning point. We also note that the classical turning point corresponding to an opacity of 0.5 is about 4.05 A. At this internuclear separation, the charge induced dipole interaction as given by the expression

$$V = -\frac{e^2\alpha}{2R^4}$$

where e^2 = 332.11 A kcal/mole, is 0.13 kcal/mole. Thus the formation of the ionx HeD^+ and HeD_2^+ is tied to the second step of the model, viz.,

$$He + D_2^+(v') \longrightarrow [He\text{-}D_2^+(v')] \longrightarrow HeD_2^+ \text{ or } HeD^+ + D$$

The reaction path forming HeD^+ is endothermic by about 0.8 eV for D_2^+ in the ground state. If we assume, as do Hotop and Niehaus, that the bond energy of the intermediate complex $He\text{-}D_2^+$ is less than one vibrational quantum of D_2^+, and if we assume that the dissociation energy of HeD^+ is around 1.8 eV, then the formation of the associative ion HeD_2^+ is possible only for D_2^+ ions in the v' = 0 state, and that for the rearrangement ionization ion HeD^+, v' $\geqslant$ 3 (the vibrational spacing for D_2^+ is about 0.3 eV). Much work remains to be done to determine in which vib-rot

state is the D_2^+ ion initially formed, and its effect on the subsequent reaction. In this regard, knowledge of the He-D_2^+ ionic potential should be extremely helpful. Thus a complementary study would be to perform the low-energy differential cross section measurements for the ion molecule reaction He + D_2^+.

REFERENCES - CHAPTER IV

1. H. Hotop and A. Niehaus. Z. Phys. 215, 395 (1968).

2. H. Hotp, A. Niehaus and A. L. Schmeltekofp. Z Phys. 229, 1 (1969).

3. H. Hotop and A. Niehaus. Chem. Phys. Lett. 3, 687 (1969).

4. M. T. Leu and P. E. Siska, J. Chem. Phys. 60, 4082 (1974).

5. J. S. Howard, J. P. Riola, R. D. Rundel and R. F. Stebbing, J. Phys. B, 6, L109(1973).

6. W. P. West, T. B. Cook, F. B. Dunning, R. D. Rundel, and R. F. Stebbing, J. Chem. Phys. 63, 1237(1975).

7. R. H. Neynaber, G. D. Magnuson and J. K. Layton, J. Chem. Phys. 57, 5128(1972).

8. J. R. Penton, and E. E. Muschlitz, Jr., J. Chem. Phys. 49, 5083 (1968).

9. L. T. Specht, K. D. Foster and E. E. Muschlitz, Jr., J. Chem. Phys. 63, 1582(1975).

10. A. L. Schmeltekopf and F. C. Fehsenfeld, J. Chem. Phys. 53, 3173 (1970).

11. W. Lindinger, A. L. Schmeltekopf and F. C. Fehsenfeld, J. Chem. Phys. 61, 2890(1974).

12. R. C. Bolden, R. S. Hemsworth, M. J. Shaw and N. D. Twiddy, J. Phys. B, 3 61 (1970).

13. G. E. Veatch and H. J. Oskam, Phys. Rev. A 8, 380 (1973).

14. J. S. Cohen and N. F. Lane, J. Chem. Phys. 66, 586 (1977).

15. R. K. Preston and J. S. Cohen, J. Chem. Phys. 65, 1589 (1976).

16. A. P. Hickman, A. D. Isaacson and W. H. Miller, J. Chem. Phys. (1977). To be published.

17. A. P. Hickman, A. D. Isaacson and W. H. Miller, J. Chem. Phys. 66, 1483(1977).

18. H. Haberland. (Private communication)

19. R. D. Rundel, F. B. Dunning, and R. F. Stebbings, Rev. Sci. Instrum. 45, 116 (1974).

20. A. D. Isaacson, A. P. Hickman, and W. H. Miller, J. Chem. Phys. 67, 370 (1977).

21. Private Communications.

TABLE I

MMSV POTENTIAL PARAMETERS

ε(kcal/mole)	0.0285
r_m (Å)	6.4
β_1	5.9
β_2	7.5
C_6 (kcal/mole Å^6)	250
C_8 (kcal/mole Å^8)	2700
b_1	-0.750
b_2	1.133
b_3	-3.979
b_4	3.470
x_1	0
x_2	1.092
x_3	1.75

Imaginary Potential:

$V_i = \exp(-B(R-R_o))$ kcal/mole

$B = 5.2$ (Å^{-1})

$R_o = 3.8$ (Å)

TABLE II

BRANCHING RATIOS FOR COLLISIONS OF He(2'S,2^3S) with D_2

	D_2^+	HeD^+	HeD_2^+
He(2'S)			
Ref. 6	0.85	0.10	0.026
Ref. 2	0.84	0.13	0.028
Ref. 15 (Theoretical)	0.905	0.095	⟨0.00⟩
This Work	0.54	0.41	0.042
He(2^3S)			
Ref. 6	0.88	0.081	0.015
Ref. 2	0.88	0.10	0.016
Ref. 15	0.905	0.095	⟨0.00⟩
This Work	0.93	0.068	0.006
Mixed Beam Result			
Ref. 9	0.83	0.15	0.02

TABLE III

RATIO OF $He(2^1S)/He(2^3S)$ ION PRODUCTION CROSS SECTION

Energy (kcal/mole)	HeD_2^+	HeD^+	D_2^+	Total
1.02	0.412	0.509	0.362	0.373 ±10%
1.73	3.367	2.219	0.127	0.282 ±15%
2.0	3.085	2.603	0.250	0.426 ±10%
2.6	1.871	1.747	0.231	0.335 ±10%
RESULTS OBTAINED BY OTHER BEAM STUDIES AT 300°K				
Howard et al. (Ref. 5)				0.87±10%
Dunning et al.(Ref. 6)				0.67±25%
Hotop et al. (Ref. 1)				0.60±5%

FIGURE CAPTIONS - CHAPTER IV

Fig. 1 Newton diagrams for He^*+D_2 and He^*+H_2. We see that the use of D_2 instead of H_2 is clearly advantageous in terms of the wider laboratory angular range it provides.

Fig. 2 The elastic differential cross section for $He(2^3S) + D_2$ at 1.02 kcal/mole.

Fig. 3 The elastic differential cross section for $He(2^3S) + D_2$ at 1.73 kcal/mole.

Fig. 4 The elastic differential cross section for $He(2^3S) + D_2$ at 2.6 kcal/mole.

Fig. 5 The MMSV potential obtained in this work along with its corresponding ionization width.

Fig. 6 Comparison of the slope of our proposed potential with those calculated by the two groups Cohen and Lane, and Hickman et al.

Fig. 7 Comparison of the ionization width obtained in this work with those calculated by the two groups Cohen and Lane, and Hickman et al.

Fig. 8 The elastic differential cross section for $He(2^1S)+D_2$ at 1.02 kcal/mole.

Fig. 9 The elastic differential cross section for $He(2^1S) + D_2$ at 1.73 kcal/mole.

Fig. 10 The elastic differential cross section for $He(2^1S) + D_2$ at 2.6 kcal/mole.

Fig. 11 The temperature dependence of the rate constant for $He(2^3S)+D_2$ as calculated from our proposed potential is compared with the experimental data of Lindinger et al. (here shown with their uncertainties).

Fig. 12 Energy dependence of formation of various ionic products in the interactions $He(2^3S)+D_2$, and $He(2^1S)+D_2$.

Fig. 13 Ratio of singlet to triplet ionization cross sections as a function of the relative collision velocity. The figure is taken from the work of Cohen and Lane.

Fig. 14 Comparison of the calculated ionization cross sections based on our proposed potential with Preston and Cohen's theoretical results.

Fig. 15 The calculated total elastic cross section as a function of the collision energy based on our proposed potential.

Fig. 16 The probability of ionization as a function of the angular momentum for various collision energies.

Fig. 17 The classical turning point as a function of the angular momentum for various collision energies.

Fig. 18 The probability of ionization as a function of the classical turning point for various collision energies.

He^*/D_2

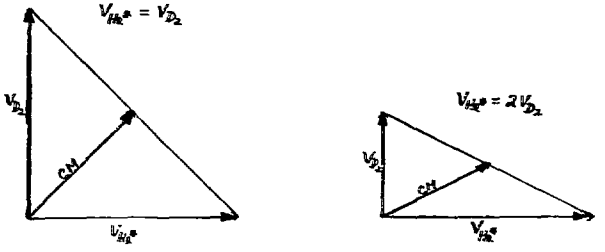

He^*/H_2

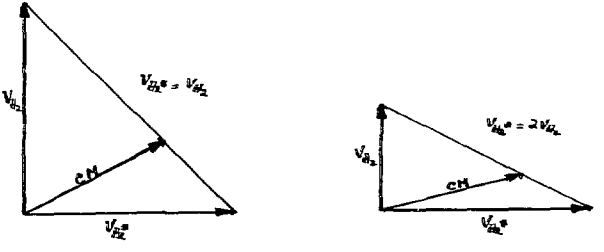

Fig. 1

XBL 7710-10240

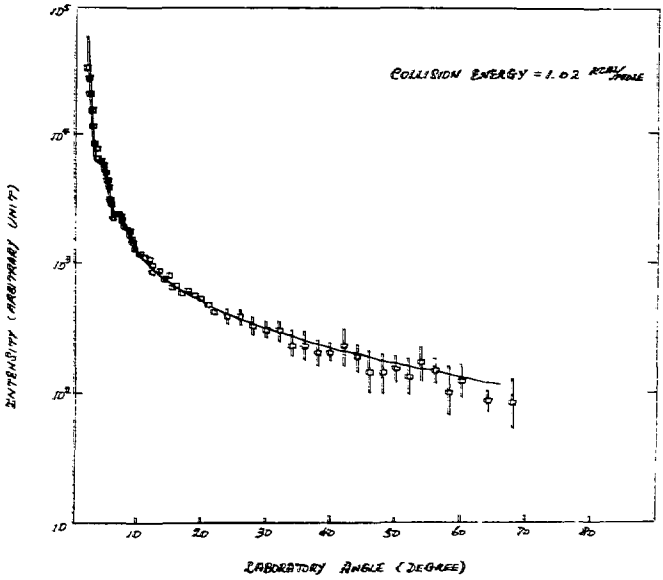

KSL 7710-5784

Fig. 2

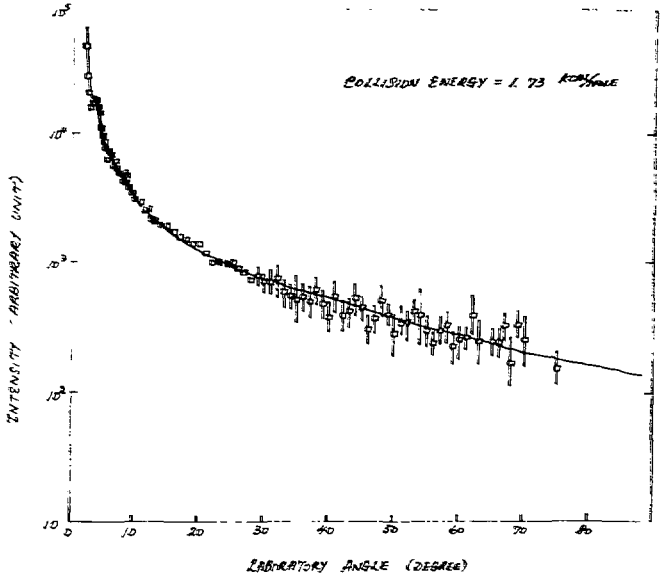

Fig. 3

KSL 7710-6779

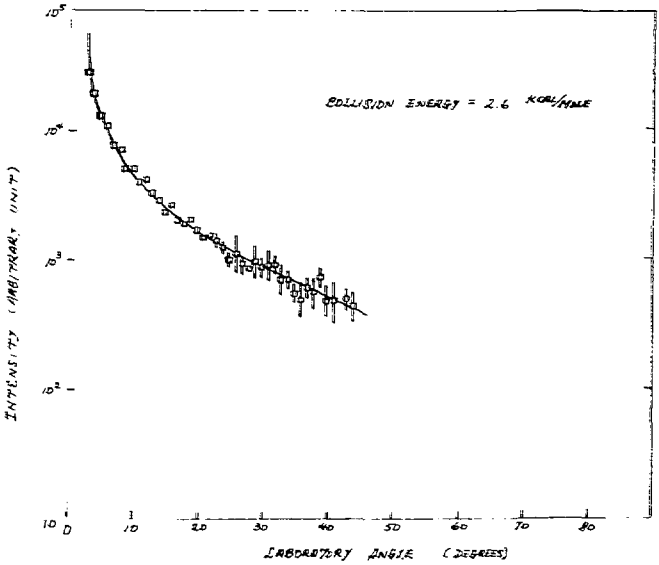

KSL 7710-5783

Fig. 4

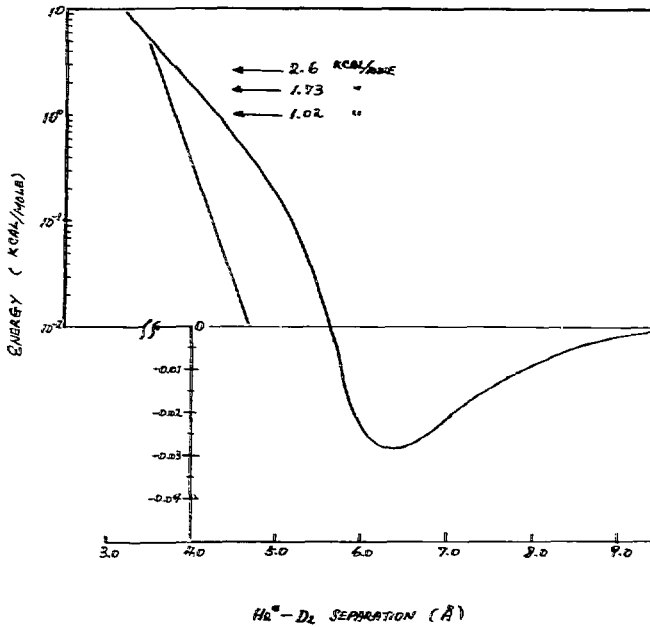

XBL 7710-6786

Fig. 5

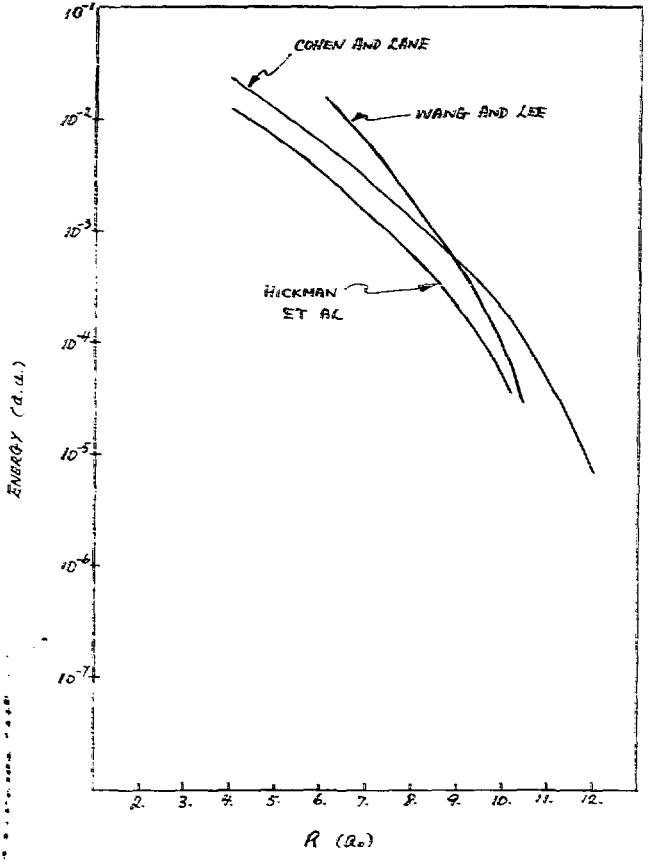

Fig. 6

KSL 7710-6780

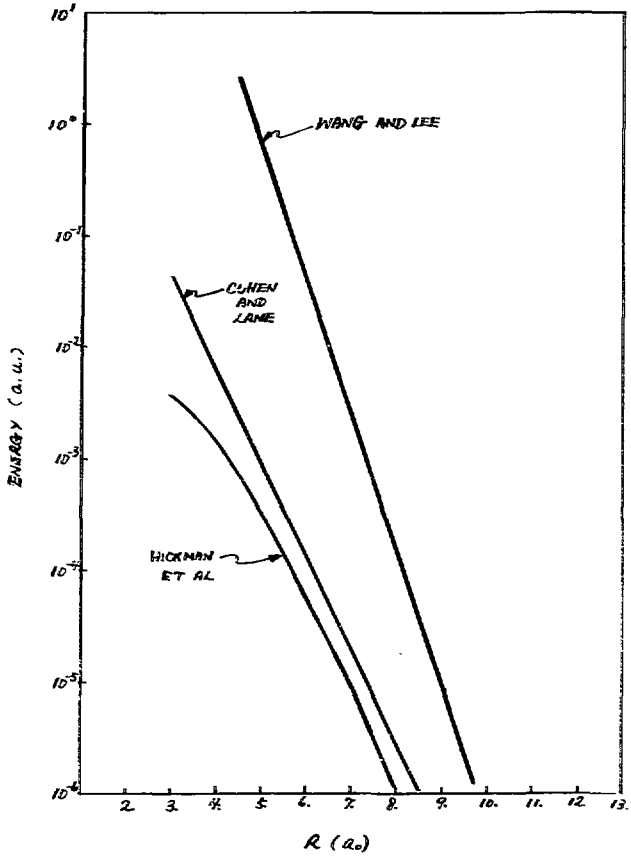

Fig. 7

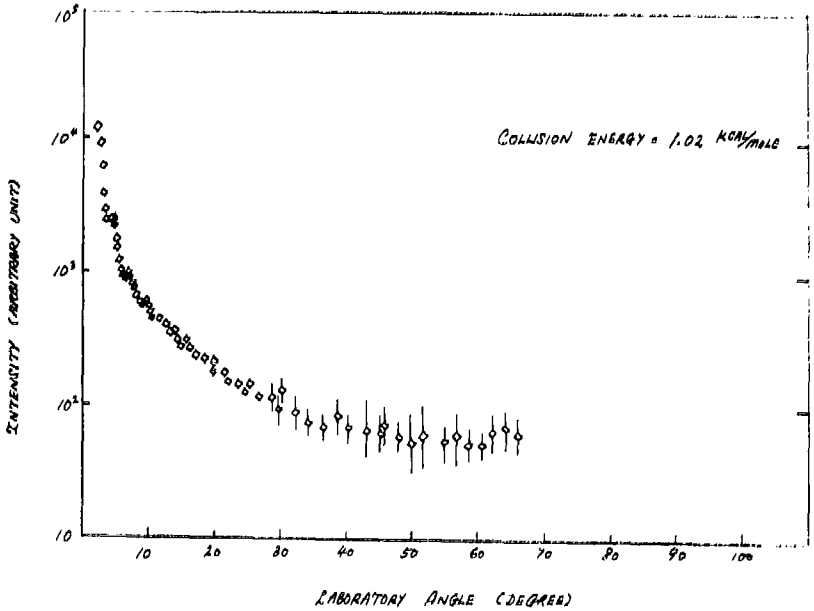

Fig. 8

XBL 7710-6739

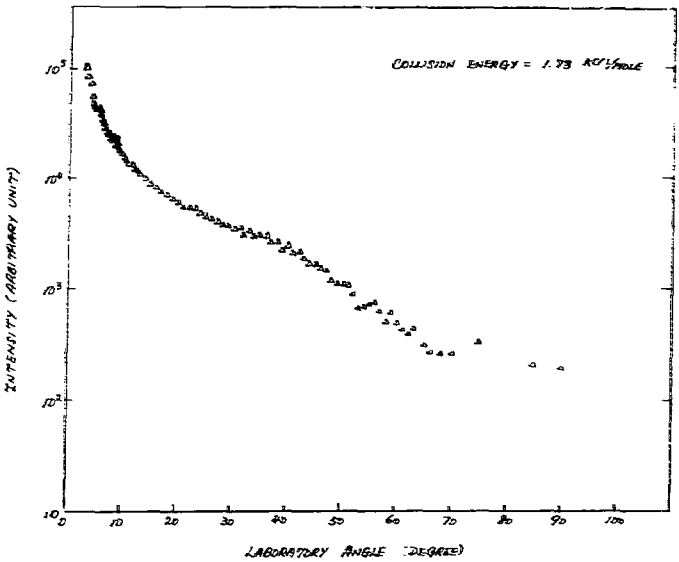

ISL 7710-6788

Fig. 9

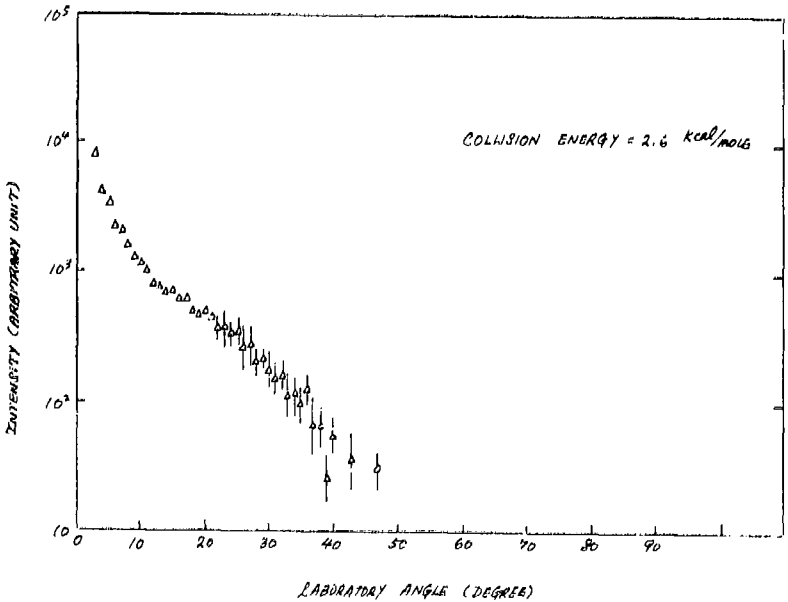

FIG. 10

XBL 7710-6790

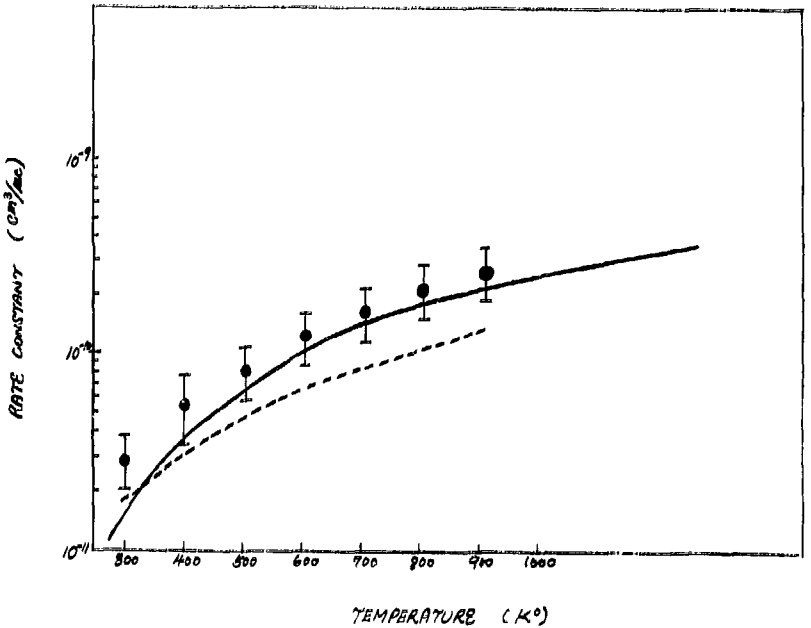

Fig. 11

XBL 7710-6791

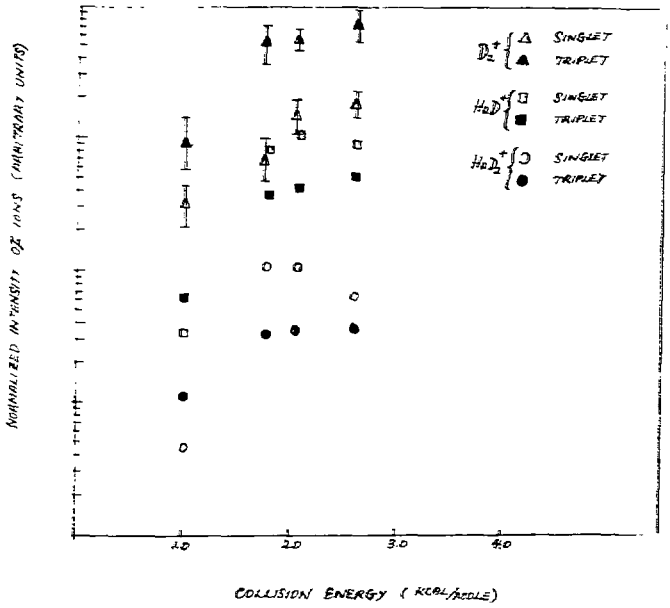

Fig. 12

KBL 7710-6792

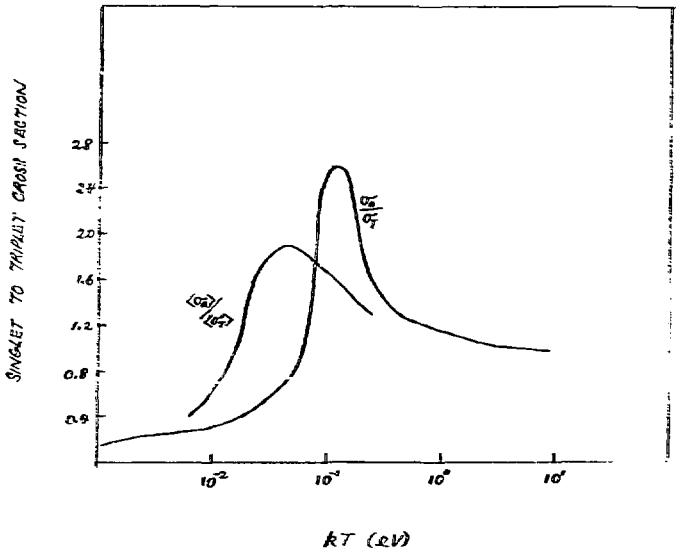

KBL 7710-6744

Fig. 13

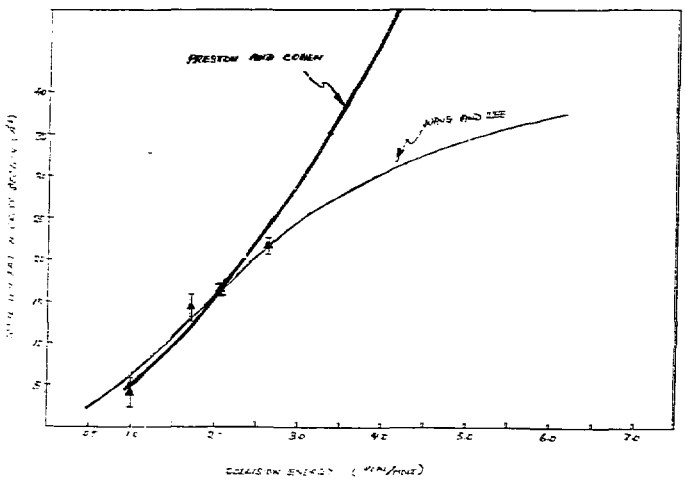

KBL 7770-10056

Fig. 14

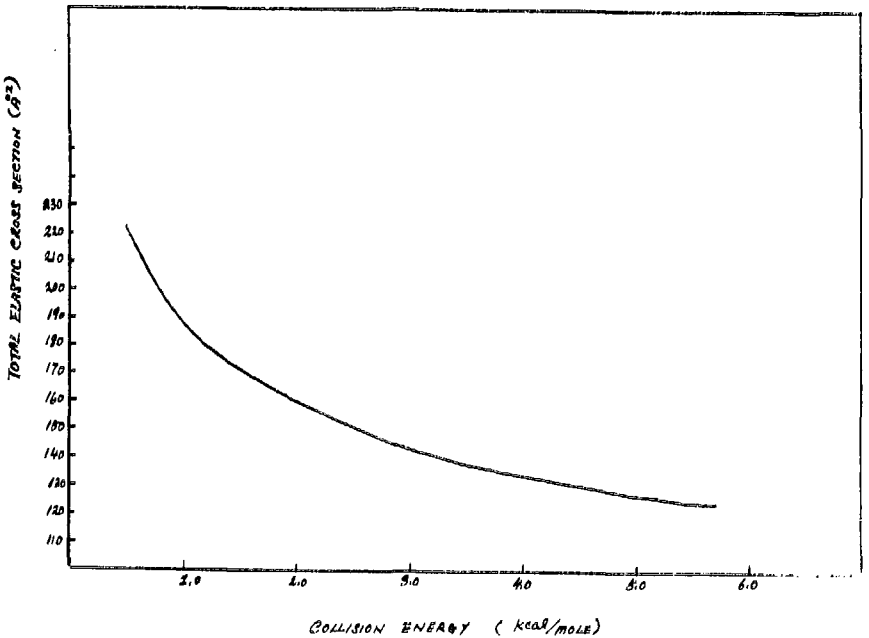

Fig. 15

XBL 7710-6793

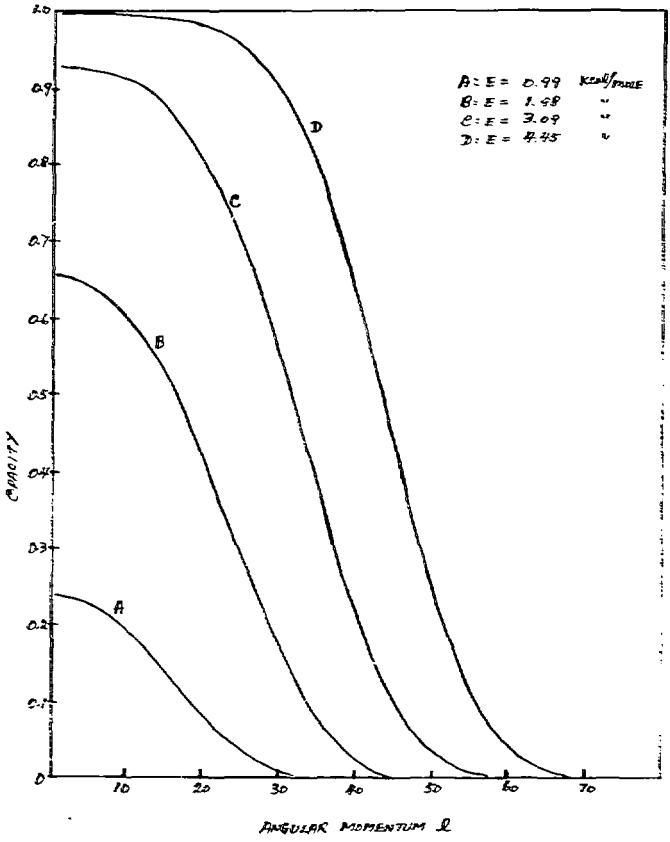

Fig. 16

XSL 7710-6781

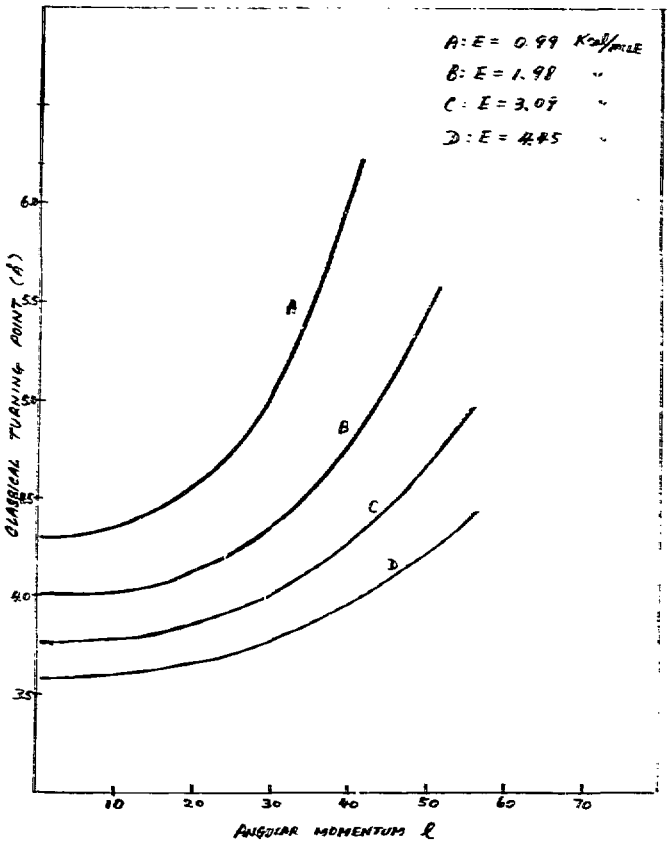

Fig. 17

XBL 7710-6795

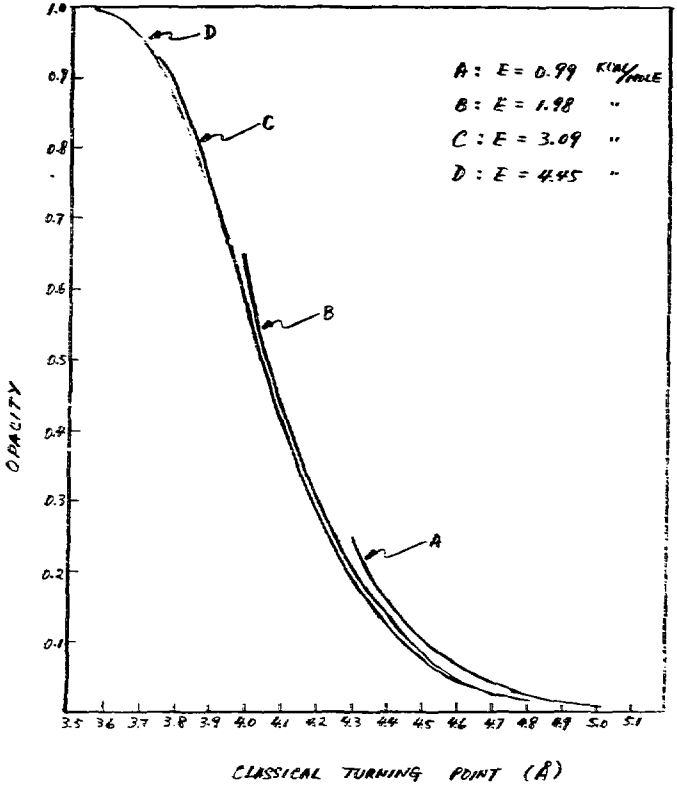

Fig. 18

XBL 7710-6795

V. THE CONSTRUCTION AND PERFORMANCE CHARACTERISTICS OF A NITROGEN-LASER-PUMPED-DYE LASER SYSTEM

A. Dye Laser Physics

Since their first discovery eighteen years ago, lasers have nowadays found themselves into many branches of science. The phenomenal growth of their range of applicability has placed an ever increasing demand on coherent radiation sources which are at once powerful as well as widely tunable. This challenge is met in part, at least in the visible region of the spectrum, by dye lasers.

For our purposes here, dyes, as far as their chemical constituency is concerned, are simply large molecules which contain conjugated double bonds. Laser dyes, in partiuclar, are distinguished in their unique spectroscopic properties. These include:

(a) Both the absorption and emission bands are fairly broad (about 1000 cm^{-1}).

(b) The fluorescence band is generally a mirror image of the absorption band.

(c) The fluorescence lifetime is about 10^{-9} sec.

(d) The maximum of the fluorescence band occurs at a longer wavelength (lower energy) than the maximum of the principle absorption band. This displacement is known as the Stokes shift of fluorescence from the absorption. The extent of this Stokes shift, and the width of the fluorescence and absorption spectra may be such that the short wavelength tail of the fluorescence substantially overlaps the long wavelength tail of the absorption.

(e) A triplet-triplet absorption band may overlap the fluorescence band.

These physical properties of laser dye molecules may be understood with reference to Fig. 1. We have plotted here the pertinent energy levels of a typical laser dye molecule with respect to some generalized configuration coordinate (the triplet system has been arbitrarily shifted to the right for clarity). We have deliberately magnified in this diagram the difference in the coordinate position which corresponds to the minimum energy for each state, thus emphasizing that the equilibrium configuration depends on the particular electronic state. The ground electronic state of the dye molecule is a singlet S_0. Many vibrational and rotational levels can exist within it. The energy difference between neighboring vibrational states is ~1400-1700 cm^{-1}, while the energy spacing between rotational states is smaller by approximately two orders of magnitude. Thus these rotational levels effectively form a near continuum of states between the vibrational levels. At room temperatures, the thermal equilibrium distributions are such that very few molecules are more than 200 cm^{-1} away from the lowest ground state level.

The absorption process (in solution) therefore can be seen as the promotion (in the usual Franck-Condon fashion) of the dye molecules from their low-lying levels in S_0 to some excited vib-rot states in S_1 (this is denoted by $A \rightarrow b$). The latter states, like those in S_0 and for the same reasons, also span a quasi-continuum. Thus the absorption has resulted in a non-equilibrium distribution of population in S_1, this is however quickly dissipated by collisions with surrounding solvent

molecules.* A large molecule typically experiences some 10^{12} collisions/sec in a liquid solution, this means that thermal equilibrium in S_1 can be reached in the time of the order of a pico-second. These collisionally-induced non-radiative transitions effectively quench all the molecules in S_1 down to its lowest vibrational level ($b \rightsquigarrow B$). From here, they can return to S_0 via the emission of a photon whose energy is now necessarily less than that of the absorbed light ($B \rightarrow a$). This is a spin-allowed transition, and thus the typical fluorescence lifetime of the state S_1 is around 10^{-9} sec. The ratio of the number of emitted photons to the number of absorbed pump-photons is called the fluorescence quantum efficiency, and can be as high as unity for some dye solutions.

In addition to fluorescence, molecules in S_1 can undergo three other types of transitions; these therefore compete with the radiative process of primary utility. Transitions between S_1 and other excited singlet states ($S_1 \rightarrow S_2$) can possibly occur at the same wavelength as the fluorescence. Also, non-radiative transitions between states of the same multiplicity (internal conversion) can occur ($S_1 \rightsquigarrow S_0$).[1] Finally, molecules in S_1 can change their multiplicity by non-radiatively crossing over to a low-lying triplet state T_1. This interesting process of inter-system crossing can be brought about by internal perturbations (spin-orbit coupling, the presence of substituent groups in the dye molecule with nuclei of high atomic number) as well as by external perturbations (paramagnetic collision partners, like O_2 molecules in the solution).

---

* Since this relaxation in S_1 also occurs in the gas phase, an additional mechanism besides collisions with solvent molecules must exist. This is postulated to involve the rapid intermolecular redistribution of excess vibrational energy via anharmonic coupling.

The lifetime for decay of the triplet state ($T_1 \rightarrow S_0$) is generally much longer than the fluorescence lifetime since the triplet→singlet transition is spin-forbidden. Thus the triplet state serves as a trap for the excited molecules; and che accumulation of molecules there introduces another complication as T_1 is but the lowest lying state of a manifold of excited triplet states. Triplet-triplet absorption ($T_1 \rightarrow T_2$) are spin-allowed and usually have relatively high extinction coefficients.[2] In a number of fluorescent dyes, this absorption overlaps with the $S_1 \rightarrow S_0$ spectrum (Fig. 2).

B. The Dye Molecule as Laser Medium

The basic laser cycle for dye molecules involves three steps: (a) excitation from the ground vibrational state of S_0 to excited vib-rot states of S_1; (b) fast radiationless transitions within S_1 which bring all the molecules down to its ground vibrational level; (c) fluorescence from the lowest-lying states of S_1 to the high-lying vib-rot levels of S_0. This whole process thus en' ils the participation of four groups of energy states of the dye which, like all other four-level laser media, is therefore expected to be very efficient in terms of the degree of inversion required for lasing. The presence of inversion (or positive gain) is defined by having the number of molecules in the upper lasing level (i.e. the ground vibrational state of S_1) to be greater than that in the lower lasing level (i.e. the high-lying states of S_0). The latter, as established earlier, is initially unpopulated (and once populated can be rapidly thermalized to the lowest state), we therefore conclude that only a small inversion marks the lasing threshold.

We now turn our attention to some qualitative criteria that must be satisfied by the excitation source to achieve positive gain. We will confine our discussion to operations in the pulse mode only. The somewhat more difficult continuous wave (cw) case has been dealt with by many authors.[3] The presence of an optical resonator bordering the dye medium as well as properly aligned with it is also assumed here to lend practical relevance to the notion of gain. Thus we seek to qualitatively describe the time evolution of a solution of dye molecules in the limit of excitation by a delta function pulse of the right frequency.

The excitation is taken to occur at t_0. This immediately (within 10^{-15} sec or shorter) results in a fraction W of the dye molecules being promoted to some excited vib-rot levels in S_1. At $t_0 + 10^{-12}$ sec., most of these excited molecules will have radiationlessly relaxed to the lowest vibrational state of S_1, and fluorescence now commences. Fluorescence, or spontaneous radiation, is isotropic, and its rate is independent of the number of photons present. Since the dye cell is in an optical cavity, some of the fluoresence photons will find themselves traveling along the optical axis of the resonator, and therefore be sent back into the dye cell (the fraction of photons sent back depends on factors like the transmission of the cavity's output coupler, and the degree to which the resonator is aligned, etc.). These rebounced photons will set-off another process, namely stimulated emission. The probability of stimulated emission, hence its rate, is directly proportional to the number of photons present (in sharp contrast to spontaneous emission). We see that initially, stimulated emission is necessarily very weak compared to spontaneous emission. However, as more and more photons are persuaded by the

ever-expanding train of stimulated photons to "join the bandwagon", there will come the inevitable time when it is more probable for the molecules in S_1 to undergo stimulated emission than radiating spontaneously. Indeed, an avalanche of stimulated photons then results, generating the familiar large pulse (Fig. 3).

The above description, while pictorial, nonetheless yields some important conclusions about the excitation source. (a) In real life, there is of course no delta-function pulse, but we see from our discussion that the excitation source should have a very fast time in order to adequately compensate for the loss due to spontaneous emission. (b) The higher the input power (hence more excitation photons), the faster can stimulated emission override its spontaneous competitor, and thus higher will be the conversion efficiency.

There is finally an additional requirement on the pump source which is implicit in the foregoing discussion. The excitation photons must have sufficient energy to be able to raise the dye molecules from S_0 to S_1. The separation between these two electronic states necessitates the use of visible photons. Clearly, the shorter the wavelength of the excitation source (within reason), the more different families of dyes it can pump. Anything in the near-UV region is therefore very attractive.

While the desired spectral, power-output, and rise-time specifications for efficient dye laser operation can be implemented in an excitation source in several ways,* pulsed systems such as the Nitrogen laser have proved to be most satisfactory in terms of the ease of construction as

---

* such as mode-locking a ruby laser and then frequency-double its output pulses.

well as the overall performance. In this chapter, we will describe the design considerations for and the actual construction details of such a nitrogen-laser-pumped dye laser system. We will also briefly mention a flashlamp-pumped dye laser by way of comparison.

C. The Nitrogen Laser

For our present interest, we will only consider three electronic states of molecular nitrogen: ground, $C^3\pi_u$ and $B^3\pi_g$. They are shown in Fig. 4. It has been found that[4] the total cross section for excitation by electron impact from the ground state X to the excited state C is on the whole twice as large as that for the B state. Thus population inversion of the C state relative to the B state, which results in the laser transition at 3371 Å, can be effectively realized in an electrical discharge.

The radiative lifetime of the C state is about 40 nsec., while that of the B state is 5-8 μsec. It is therefore obvious that steady state inversion, which requires that the B state be emptied faster than the C state is populated, can never be realized by radiative de-excitation of the B state alone. CW laser action is therefore extremely difficult. For the purpose of pumping dyes, however, pulse operation is actually a blessing since large peak powers can be obtained from moderate input power in the energy storage circuit. Also, any thermal heating problems in the dye solution due to the excitation process can be more easily taken care of. The gain of the N_2 laser is so high that feedback in the from of mirrors is unnecessary, and the laser light just pours out in a superradiant fashion.

D. The Physics of Electrical Discharges as Applied to the Excitation of N_2

It was noted earlier that the excitation cross section for the C state of N_2 is larger than that of the B state. To be more specific, we must reconize that the exact value for these cross sections depends on the energy of the electrons used, their ratio therefore would change as a function of the electron energy. From Fig. 5, we see that this ratio of the cross sections peaks around 16 eV. We therefore wish to design our electrical discharge circuit in such a way as to provide the electrons with this optimum energy.

To do this, we claim first of all that the electron distribution function for a nitrogen discharge can be well approximated by a Maxwellian function when the ratio of the electric field to the pressure of gas exceeds 30 to 40 volts/cm.torr. This is indeed the conclusion reached by Klein and Siambis[5] in their theoretical simulation of electrical breakdown phenomena. Secondly, since the average distance which an electron travels in the field E before it undergoes a collision is given by[6]

$$d_1 = (eE/m_e)t_1^2$$

the average time interval between collisions is

$$t_1 = (m_e v_d/eE)$$

where v_d is the drift velocity of the electron. t_1 is of the order of 10^{-12} sec, which is much shorther than the nanosecond time scale of the laser. Thus, for all practical purposes, the electrons in the discharge can be considered to be in a steady state with the instantaneous electric field.

The above observations make it very reasonable for us to describe the nitrogen plasma, which typically has E/p > 100 volts/cm.torr, in terms of an electron temperature T_e. To determine T_e, we seek an expression relating the temperature of the lectrons to the ionization rate, which can be measured. In terms of a kinetic model, the latter is given by plugging the ionization rate for one energy into the usual expectation formula.[7] Thus we have for the mean ionization rate

$$4\pi \int_0^\infty g(T_e,v)\ \{N_0\sigma(v)v\}\ v^2 dv \qquad (1)$$

where N_0 is the density of ground state molecules, $\sigma(v)$ is the ionization cross section at v, and v is the electron velocity. The expression in parenthesis is just the ionization rate at the velocity v. $g(T_e,v)$ is the normalized Maxwell-Boltzmann distribution.

Experimentally, the ionization rate is generally expressed as

$$\alpha v_d \qquad (2)$$

where α is the first Townsend coefficient, and v_d is the drift velocity of the electrons. We can therefore equate Eq. (1) and (2),

$$\alpha v_d = 4\pi N_o \int_0^\infty g(T_e,v)\sigma(v)v^3 dv \qquad (3)$$

For nitrogen, and for E/p between 20 to 150 volts/cm.torr. α and v_d are given as functions of (E/p) by[8,9]

$$v_d = 2.9 \times 10^5 \left(\frac{E}{p}\right) \quad \text{cm/sec}$$

$$\frac{\alpha}{p} = 1.4 \times 10^{-8} \left(\frac{E}{p}\right)^{3.7} \quad (\text{torr. cm})^{-1}$$

And an analytical expression for $\sigma(v)$ can be obtained via a polynomial fit to known experimental data. Thus Eq. (3) can be integrated in terms of kT_e. This has been done by Fitzsimmons et al.[10]; they have found that

$$kT_e = 0.71 \left(\frac{E}{p}\right)^{0.80} \text{eV} \quad (E/p \text{ in volts/cm torr}) \qquad (4)$$

There is one other functional relation we can derive. Sinc the electron current density J is defined by

$$J = V_d n_e$$

with

$$n_e \equiv \text{electron density}$$

Using this along with the normalized excitation rate given in Eq. (2), we see that the rate of ionization for an electron density of n_e can be written as

$$n_e \alpha v_d = \frac{J}{v_d} \alpha v_d$$

$$= J \alpha \qquad (5)$$

$$\propto J p f \left(\frac{E}{P}\right), \quad f \text{ is one function of } \left(\frac{E}{P}\right)$$

The important conclusion to be drawn from Eq. (5) is that for a given laser geometry and supply voltage, $E = V/d$ is determined. Thus once an optimum pressure is found, the amount of inversion per unit volume and hence the amount of available power is directly proportional to the current density.

E. *E/p and Overvolting*

Since the factor (E/p) figures so prominently in our calculations, we wish to look more closely at its physical significance. In an electrical discharge involving large currents, the electron density and gas conductivity growth vary rapidly as the gas begins to break down. After a variable statistical time lag, an avalanche occurs. Then, after the so-called formative time lag, streamers form and the conduction channel fills out. The formation of a conduction channel occurs very rapidly when the gas is overvolted by a few hundred percents (Fig. 6). The process of charge multiplication during a discharge has been studied by Townsend in great detail. We will just briefly trace the course of events and derive some important relations.

The increase in current density beyond its saturation limit is attributed by Townsend to the ionization of the gas by the primary electrons. This ionization takes place when the amount of kinetic energy gained by the electron between two successive collisions reaches a sufficiently high value. An electron can therefore cause the [illegible] it collides with to lose one electron in either one direct step, or if its

---

* A gas is overvolted when a voltage exceeding its static breakdown voltage determined by discharge geometry is "instantaneously" applied to it.

energy is not adequately high, more than one step. Now we can begin to see why the ratio E/p is so important: 1/p is proportional to 1/N (where N is the gas density) and to the mean free path and hence to the energy gained between successive collisions. Thus E/p gives the average energy gained between collisions.

α, the Townsend coefficient introduced earlier, represents the number of ionizations produced by one electron per unit length in the field direction y. Thus the number of electrons as measured along the field at point ℓ must satisfy the integral equation

$$N(\ell) = \int_0^{\ell} \alpha\, N(x)\, dx$$

This can be solved by converting it to a differential equation

$$\begin{aligned} dN &= \alpha\, N(\ell)\, d\ell \\ \frac{dN}{N} &= \alpha\, d\ell \\ \ln\frac{N}{N_0} &= \alpha\ell \\ N &= N_0\, e^{\alpha\ell} \end{aligned} \tag{6}$$

We see from Eq. (6) that for every electron leaving the cathode, exp (αd) electrons arrive at the anode, where d is the distance between the electrodes. But the picture is more complicated than this because with each ionization a positive ion is created, and this ion will more towards the cathode. On its way, it may further ionize the gas*, and when it hits the cathode it may do so with sufficient energy to eject a secondary electron. This latter phenomenon turns out to be very important, its probability is given as γ. γ is known generally as the second Townsend coefficient.

Thus if exp(αd) electrons arrive at the anode, each giving rise to (exp (αd) - 1) ion pairs in the course of its path, the corresponding number of secondary electrons from the cathode would be γ(exp(αd)-1). All these can then undergo the same process as the initial electrons. Thus the flux at the anode due to a single electron is

$$e^{\alpha d} + \gamma(e^{\alpha d}-1)e^{\alpha d} + \gamma^2(e^{\alpha d}-1)^2 e^{\alpha d} + \ldots$$

$$= e^{\alpha d}[1+\gamma(e^{\alpha d}-1) + \gamma^2(e^{\alpha d}-1)^2 + \ldots]$$

$$= \frac{e^{\alpha d}}{1 - \gamma(e^{\alpha d}-1)}$$

* This is called the β effect, and generally is not very important.

Eq. (7) gives the overall multiplication coefficient for the discharge. It becomes infinite when the electric field in the gas reaches a value such that

$$\gamma(e^{\alpha d}-1) = 1 \tag{8}$$

This is the famous Townsend breakdown criterion. It should be noted that the resulting current cannot be infinite but, being no longer determined by the existence of an ionizing agent, it is limited only by the internal resistance of the source of potential difference applied across the discharge, and, of course, by the maximum output available. Thus the dynamic resistance (dV/dt) at the point of breakdown is zero. This is shown in Fig. 7, where v_b is the breakdown voltage.

To see what determines v_b, we rewrite Eq. (8) as

$$d = \frac{1}{\alpha} \ln \left(1 + \frac{1}{\gamma}\right) \tag{9}$$

where d is the breakdown distance (or anode to cathode separation). α/p as we have shown earlier, is a unique function of E/p; if we assume that γ is also a function of E/p, Eq. (9) becomes

$$d = \frac{1}{pf\left(\frac{E}{p}\right)} \ln \left[1 + \frac{1}{\phi\left(\frac{E}{p}\right)}\right]$$

Since we are dealing with a uniform field, E can be replaced by V_b/d. The breakdown criterion can now be written as

$$pd = \frac{1}{f\left(\frac{v_b}{pd}\right)} \ln \left[1 + \frac{1}{\phi\left(\frac{v_b}{pd}\right)}\right] \tag{10}$$

which means that the breakdown voltage is a unique function of the product of pressure and electrode separation for a particular gas and electrode material. pd represents the number of free paths that exist in the field direction between the electrodes. v_b thus depends on pd, regardless of the form of the functions $f(v_b/pd)$ and $\phi(v_b/pd)$. This very important observation is known as Paschen's law.

For nitrogen, Paschen's law is approximately

$$v_b = 300[12.08(pd) + 5.0] \tag{11}$$

where V_b is in volts, p in atmospheres and d in mm. For fairly large pd, Eq. (11) can be written as

$$V_b = Apd$$

where A is some constant. The discharge circuit with its inherent dv/dt will cause the discharge to overvolt by some factor B, so

$$V_{ac} = B\,V_b = A\,Bpd$$

and therefore

$$\frac{E}{p} = \frac{V_{ac}}{pd} = AB \qquad (12)$$

The implication of Eq. (12) is that as long as the voltage supplied to the laser channel is greater than V_{ac} by a sufficient amount, the ratio E/p is determined entirely by the external circuitry through B, the overvoltage factor. Thus in the zero order approximation we have, E/p at breakdown is independent of the pressure and electrode separation. Experimentally, however, E/p does depend slightly on these parameters.

F. Discharge Uniformity

Uniform discharge is very desirable for maximum power output of laser. This can be easily seen by adopting a simple model for the discharge. Assume that the discharge sparks in N equally spaced channels along the electrodes. The total gain provided by all the channels is of course determined by the total current which is fixed.

If the total gain is G, then the gain per channel is

$$1 + \frac{G}{N} \tag{13}$$

Thus as $N \to \infty$, the beam passes through each differentially thin channel with unit amplification. Now if one of the end channels generates spontaneous noise P_o, the power output of the tube is then

$$P_{out} = P_o \left(1 + \frac{G}{N}\right)^N$$

As N increases, P_{out} has a limiting value of

$$P_{out} = P_o e^G$$

The limiting value is effectively reached when

$$N = 10G$$

Thus for a uniformly discharging laser tube that saturates at 10 kw from 10 mW of noise, G is

$$\ln\left(\frac{P_{out}}{P_o}\right) = 15 \quad .$$

Hence to effectively utilize this gain, there should be at least 150 channels. If the discharge only sparks at 5 or 6 places, the gain, instead of being 10^6, is only

$$\frac{P_{out}}{P_o} = \left(1 + \frac{15}{5}\right)^5 \approx 10^3$$

The loss in gain is another reason why overvolting is very important (overvolting also provides a high electron temperature). When the electrodes are highly overvolted, B is large (vide supra) and the channel-initiating avalanches form very quickly. The faster the channels are

formed, the closer together they are. This can be reasoned as follows: when one channel is formed, it tends to short the electrodes and the local potential falls. The potential drop propagates as a pulse down the electrodes at a speed close to that of light, so no new channels can be formed where this pulse has passed by. Thus, if the channels all start forming in some time τ, they can occur as close together as $x = c\tau$. Overvolting has the effect of drastically reducing τ. When the electrodes are overvolted by 500%, τ, the time for a channel to begin forming after the first channel has formed, is down to a few picoseconds, so x is on the order of mm, and the gain of the laser is high.

G. Details of Construction of a Nitrogen Laser

a. The Discharge circuit

The high voltage pulse generator circuit is of a capacitor transfer design. It is shown in Fig. 8, and can be analysed in the usual manner. C_1 here is charged up at $t = 0$ to some voltage V_0. At $t = 0$, the spark gap fires, and we seek to determine the behavior of the current as well as the voltage pulse across C_2 shortly after. The voltage drop across C_2 is of course the same as that across the discharge channel.

Consider the circuit loop marked A. We have represented the spark gap at breakdown by an inductance L_s. Kirchoff's law states that the net voltage drop around a close loop must be zero. Thus we have

$$L_s\frac{di}{dt} + \frac{1}{C_1}\int i\,dt + \frac{1}{C_2}\int i\,dt = 0$$

$$\left(\frac{1}{C_1} + \frac{1}{C_2}\right)\int i\,dt = -Ls\frac{di}{dt}$$

$$\frac{1}{C_{11}}\,i = -L_s\frac{d^2i}{dt^2} \qquad \left(C_{11} = \frac{C_1C_2}{C_1+C_2}\right) \tag{14}$$

To solve Eq. (14), let $i(t) = A\cos(\omega t) + B\sin(\omega t)$. We recognise our two boundary conditions to be:

$i(t=0) = 0$

$L\,(di/dt)_{t=0} = -V_o$ (since the voltage across an inductor cannot change rapidly)

we therefore see that $A = 0$, and $B = V_o/(L\omega)$. Substituting these into Eq. (14) gives

$$\frac{1}{C_{11}} \frac{V_o}{L\omega} \sin \omega t = L \left(\frac{V_o}{L\omega}\right) \omega^2 \sin \omega t$$

$$\omega^2 = \frac{1}{C_{11}L}$$

therefore the current as a function of time is

$$i = \frac{V_o}{L\omega} \sin \frac{t}{\sqrt{C_{11}L}} \tag{15}$$

The voltage across C_2 is related to the current by

$$V_{C_2} = \frac{Q}{C_2} \quad , \quad \frac{d}{dt} V_{C_2} = \frac{i}{C_2}$$

thus

$$V_{C_2} = \frac{V_0}{i\omega C_2}\int \sin \omega t$$

$$= \frac{V_0 C_{11}}{C_2} \quad (\cos \omega t - 1)$$

$$C_1 \approx C_2: \; V_{C_2} = \frac{V_0}{2}(\cos \omega t - 1) = -V_0 \sin^2 \frac{\omega t}{2}$$

We see that at $t = \pi/\omega$, $V_{C_2} = V_0$, and this the maximum voltage across C_2. In actual practice, the voltage will not be able to get this high because the gas in the laser tube will breakdown at a much lower voltage, usually around $V_0/2$ (reached after $\pi/2\omega$ sec). However, if the pressure in the laser tube is purposefully set high enough, the breakdown in the tube will not occur and the open circuit voltage of the pulse generator can be observed. This allows us to get an estimate on the damping time τ as well as the angular frequency ω via the relation

$$V_{observed} = V_0(1 - e^{t/\tau} \cos \omega t)$$

Combining the fitted values of τ and ω with a measurement of C_2, the spark gap inductance L_s and the damping resistance $R = 2L_s/\tau$ can be determined. Typical values for L_s and R are 15 nH and 2 ohms respectively. Since the damping resistance is quite high, and the C_1-to-C_2 transfer scheme necessitates all of the energy stored in C_1 be delivered through the spark gap to C_2, we therefore deliberately make C_1 a little larger than C_2 to compensate for the losses in the switch.

The optical output is very accurately synchronized with respect to the voltage across the laser tube with the peak power occuring at a time approximately half-way down on the falling laser tube voltage. This is shown in Fig. 9. The tight coupling between the driving electrical circuit and the optical properties of the laser are indicated by the fact that the time scales for both the optical and electrical characteristics are about the same.

b. The Discharge Tube

The laser tube design is shown in Fig. 10. The two vertical aluminum bars are held together via screws threaded into the horizontal plexiglas plates. Vacuum seal is afforded by the use of RTV on all the joints. Two 0.243" slots 0.125" deep are milled into the aluminum bars and copper tubings of 0.25" OD (1/16" wall) are pressed into them serving as electrodes by circulating water. This is very necessary when the laser is operated at a high repetition rate. Since the discharge produces a lot of ozone as well as other chemicals which tend to degrade synthetic plastics, we have covered the inner surfaces of the plexiglass walls with thin ceramic

plates (RTV is again used for this purpose). The high and low voltage side of the laser tube are connected by two sheets of resistive paper (around 100 ohms/sq. in) located along the outside of the plastic insulator and extending the length of the 24" long discharge tube. This small resistance is necessary to maintain the voltage across the laser tube close to zero during the charging of the primary capacitor C_1. Also, the location of the surface resistance shorts out the otherwise inevitable fringing electric fields and thereby assures a more uniform electric field inside the tube during the early development of the discharge. This field uniformity effectively prevents arc formation, and helps to confine the discharge to a thickness which is approximately equal to the diameter of the electrodes. On this basis, the closer the resistive paper is placed to the discharge, the better defined is the discharge. Ideally, therefore, the paper should be glued to the inside surface of the discharge tube, and then be covered with ceramic plates.

A front surface aluminized mirror and a quartz window are sealed to the two ends of the discharge tube with O-rings. They are both about 3" removed from the active region of the discharge so that dirty deposits arising out of the latter will be pumped away before they can accumulate on the surface of the mirror and the window. The aluminum mirror is roughly prealigned by sight via four alignment screws. The final alignment is performed when the laser is turned on. The mirror and the quartz plate are then both adjusted to give the fluorescence image of the laser pulse as seen on a piece of paper the approximate shape of an eye.

c. The Gas Flow

A good design for gas flow in the laser tube is crucial to its operation. It is highly desirable that the residual ionization remaining from the previous discharge pulse be distributed uniformly and with the proper density in order to seed the next discharge. These conditions can be met by flowing the gas in a direction transverse to the laser optical axis. As shown in Fig. 9, the N_2 gas comes in through an input manifold which is placed directly behind one of the copper electrodes (the left one in Fig. 8). The gas then flows across the tube through the action of a pump which is connected to an exhaust manifold located directly behind the other electrode. Sufficient uniform gas flow can be maintained by having 8 input and exit holes distributed evenly along each electrode and placed so as not to be opposite one another. At 60 Hz repetition rate, a 10 CFM pump is necessary for reliable operation. If the repetition rate is reduced, then the pump must be throttled in order to save some ions for the next discharge. The overall gas flow scheme is shown in Fig. 11.

d. The Spark Gap

The laser incorporates a free running (non-triggerable) two electrode spark gap. The electrodes are made from 3/8" thick copper plates out of which are cut two rectangles measuring 1" x 2". All sharp edges and corners are carefully rounded off and polished. The electrodes are positioned by two aluminum plates to given an overlapping surface area of 0.75" x 2" and a gap of about 0.06" (Fig. 12). Provisions are

also made in the aluminum plates for adequate water cooling. The rest of the spark gap housing is machined from a solid plexiglas block, this is coupled to the electrodes via O-rings. The inside of the housing is again lined with ceramic plates for protection. The combination of heavy copper electrodes and water cooling results in the migration of successive sparks over the entire overlapping area of the electrodes. Also, since the gap spacing is small compared to the transverse dimension of the electrodes, almost all the Cu evaporated during a particular spark is redeposited elsewhere on the electrodes. Thus while the cathode suface becomes slightly convex after a long period of use, the gap spacing would remain the same. The switch is typically pressurized with N_2 to about 22 psi with the gas flowing through the gap to be used again (after filtering and drying) at a reduced pressure in the laser tube.

e. The Power Supply

Two electrodes spark gaps are somewhat notorious in their erratic performance. The exact voltage at which breakdown occurs can vary from shot to shot over a significant range. This would result in intolerable fluctuations in the laser output stability. However, such an undesirable feature can be virtually eleiminated if the proper power supply is used to drive the spark gap. The essential features of such a power supply and its mode of operation are shown respectively in Fig. 13 and Fig. 14. The crucial trick is to be able to tune the power supply to the line frequency in the sense that the inductance located on the primary side of the high voltage transformer should be selected to give $L = (1/\omega^2)$,

where C is the laser energy storage capacitor (C_1) transformed to the primary circuit, and ω is the line frequency at 60 Hz. The operation of the supply depends upon the transient response of the non-linear circuit to the first half and then to the second half of a complete cycle of the applied line voltage. The capacitor is charged to its maximum value in about 1/120 seconds. With the proper inductance in the primary, the peak capacitor charge voltage will be reached just as the applied line voltage passes through zero. Thus if the spark gap pressure is adjusted so that the gap fires at the maximum charge voltage, then the transformer can no longer deliver any significant current to the system after the gap becomes a short circuit. This reduces the current carried by the switch to be only the amount needed to discharge the capacitor, and it also insures that the gap will open again just as soon as the capacitor is discharged. Also, since the time rate of change of the charge voltage is zero at the end of the cyle, the gap will always fire at the same voltage. Under proper conditions the laser output exhibits fluctuations of only about 7% in intensity. Finally, the inductance L can be varied to meet the desired matching condition by the elegant use of a box of #12 gauge wire.

f. Energy Storage Capacitor

Both C_1 and C_2 in Fig. 7 are constructed out of 1/8" thick aluminum plates. A cross-sectional view of how C_1 and C_2 are stacked together in the actual assembly is given in Fig. 15. We see that the laser is nearly symmetrical (except for the spark gap) with respect to the centerline marked X. We have labeled the top stacks of aluminum plates A, B, C and

D respectively for our discussion. C_1 then consists of the sum capacitors formed by B-A and B-C, while C_2 is just the combination C-D. When the spark gap fires, all the energy stored in C_1 is transferred through the gap to C_2. The latter, as clearly shown in Fig. 14, is just parallel to the discharge channel. The bottom stack of plates obviously function in the same manner.

The dimension of the plates A, B, C and D are respectively, 22" x 19.75", 21" x 20", 22" x 19.75", 26.75" x 25.375". All the plates are meticulously polished to ensure that their surfaces are totally devoid of any sharp points. The edges of the inner plates (A, B, C) are rounded off first by means of a 1/8" spherical milling tool, and then polished again. Problems due to corona discharge are most severe at the edges. We have used 5 mil thick Mylar sheets between plates A and B, as well as B and C, but only two between plates C and D. All the mylar sheets are first oiled with filtered transformer oil, and the desired thickness is then built up with care to exclude air between the various layers Each stack of Mylar sheets is sandwiched by wax paper (2 mil thick) whose function is twofold: to distribute the oil evenly over the entire surface of the aluminum plate, and, more importantly, to shield the Mylar from attack by the inevitable ozone that is generated in corona discharges. The capacitor plates are firmly and rigidly held together in order to maintain a uniform spacing and to prevent mechanical flexing of the plates during the charging and discharging of the capacitors. In their eight months of operation (over 60 hours of use), none of the capacitors has required any kind of servicing.

Finally, the actual capacitance with which we need to determine the value of the charging choke, can be well estimated by the formula

$$C = 1.11 \times \frac{2\epsilon}{4\pi} \times \frac{L \times \ell}{s} \quad (pF) \qquad (17)$$

where $L \times \ell$ is the overlapping area defining the capacitor (in cm^2), s is the thickness of the dielectric in mm, ϵ is the dielectric constant of the dielectric which for Mylar is 3.8. C_1 and C_2 are therefore determined to be 25 nF and 15 nF respectively.

g. Performance Characteristics

At 60 Hz repetition rate, the N_2 laser as described above provides an average power of 250 mW with peak powers reaching 570 kW. The pulse width (FWHM) is about 7 nsec. The average power is measured with a calibrated Scientech thermopile, and the peak power is obtained by dividing the average power by the repetition rate times the duration of the pulse. The overall efficiency as determined by dividing the average optical power by the electrical input (all the way back to the wall socket) is about 0.04%. Fig. 16 gives the peak power as a function of the repetition rate. The operating pressure of N_2 for these measurements is 55 torrs.

H. The Dye Laser Module

This is of a conventional design with a 1180 grooves/mm grating blazed at 5000 A to provide wavelength selected feedback. The dye-cell, the grating, the output coupler as well as the 2" diameter cylindrical lense which is used to focus the N_2 beam onto the dye-cell are all accurately defined on a thick aluminum slab serving as the base mounting plate. Alignment of the dye cavity is therefore made almost foolproof, and generally takes no longer than a few minutes. The grating is mounted on a rotatable drive which can be manually or electrically controlled. The dye cell itself is somewhat novel in that all the required seals are made via O-rings. This feature is in part motivated by the frustrations one encountered when working with the alternatives such as epoxy, RTV, glass powder, etc., which all reacted in due course with the various solvents one must use to make up optimum dye solutions. Silicon O-rings, by comparison, are infinitely inert. The dye solution is circuited with the help of a small pump, and its flow rate is adjusted to give a maximum power as well as best optical beam quality by means of a pyrex flow meter. Typical conversion efficiency of the dye laser with respect to the N_2 laser is in the range of 11-15%.

I. A Flashlamp-Pumped Dye Laser

We were motivated to construct a flashlamp dye laser system because of the high energy per pulse it can deliver. The pumping cavity for the dye cell is of the standard elliptical shape with the major and minor axis measuring 2.274" and 2.140" respectively; its length is 3.5". The

dye cell of length 3.2" is then placed along one of the foci-axis, and the flashlamp at the other. Dye circulation is again provided by a small liquid pump. In this case, the heating effects due to the discharge are quite noticeable, and the dye must have a flow-rate greater than 12 GPH for optimum operation.

Two types of flashlamps have been experimented with. One is a water-cooled Argon discharge lamp made up of a quartz capillary tube (of inside bore 3/32") and 1/16" tungsten rods serving as the electrodes. A few torrs of continuously flowing argon is maintained by means of a throttled pump. The major difficulty with this lamp is that the discharge products tend very often to clog up the bore of the capillary tube, thus stopping the argon flow. While this problem can be solved by using capillary tubes with larger bore, however the light output from the lamp goes down rather fast as the bore is increased. We then tried the commercial non-water-cooled sealed xenon lamps from ILC (model # L-1832). This produces a very clean discharge, and is on the whole much more reliable and quieter than our home-made version. Cooling for this lamp is accomplished by forcing air through the pumping cavity.

The discharge circuit, as shown in Fig. 17, uses a parallel combination of 4 LBL-salvaged 0.03 μF capacitors for energy storage, and a home made triggerable spark gap to control breakdown voltage and pulse repetition rate. The gap is triggered by feeding a 20 kV pulse to an automotive spark plug which is inserted into one of the electrodes. Care is taken to make the discharge path as short as possible so as to minimize the overall inductance of the circuit, and hence the rise time of the discharge

pulse. The capacitors are typically allowed to charge up to 10 kV (controlled by the pressure in the gap) before the spark gap is triggered. The rise time of the optical pulse from the flashlamp is found to be 500 nsec. To increase the reliability of operation, especially at high repetition rate, and also to eliminate the problem of missing pulses, we have incorporated a dc preionization circuit into the main discharge circuit. This provides a simmer current of about 5 mA through the lamp once it is started.

With 10 joules energy input to the lamp, the dye laser output with Rhodamine 6 G in methanol is about 12 mJ lasing broadband. We did not change dye concentration, dye flow-rate, etc. to optimize the conversion efficiency. As is, this dye laser provides enough power for most optical excitation purposes, and its long cavity permits the implementation of intra-cavity absorption type experiments relatively easily.

REFERENCES - CHAPTER V

1. G. W. Robinson, R. P. Frosch, J. Chem. Phys. 138, 1187 (1963).
2. (a) G. Porter, M. W. Windsor, Proc. Roy. Soc. A. 245, 238 (1958).
   (b) H. Labhart, Helv. Chim. Acta 47, 2279 (1964).
   (c) V. Zanker and E. Miethke, Z. Natuforsch, 12a, 385 (1957).
3. M. Bass, T. F. Deutsch, and M. T. Weber, in Lasers edited by A. Levine and A. J. DeMaria, New York (1971).
4. D. C. Cartwright, Phys Rev. A. 2, 1331 (1970).
5. L. E. Kline and J. G. Siambis, Phys. Rev. A5, 794 (1972).
6. A. von Engel, Ionized Lasers (Oxford Press 1965), p. 123.
7. See Harold S. Johnston, Chemical Reaction Kinetics.
8. K. H. Wagner, Z. Phys. 178, 64 (1964).
9. A. E. D. Hayler, Nature 183, 1545 (1959).
10. W. A. Litzsimmons, L. W. Anderson, C. E. Ried Lausen and J. M. Vrtilek. IEEE J. Quan. Elect. QE 12, 264 (1976).
11. Essam Nosser. Fundamentals of Gaseous Ionization and Plasma Electrons (Wiley Interscience, 1971)., p. 213.
12. ibid, p. 193

FIGURE CAPTIONS - CHAPTER V

Fig. 1 Schematic energy level diagram for a typical laser dye.

Fig. 2 Absorption and fluorescence spectra for a typical laser dye.

Fig. 3 Cartoon showing the time-evolution of a dye laser pulse.

Fig. 4 Pertinent lasing energy levels in molecular nitrogen.

Fig. 5 Excitation cross section for various electronic states of N_2 as a function of the incident electron energy.

Fig. 6 The formative time for a conduction channel as a function of overvolting.

Fig. 7 Typical I-V curve for a gaseous discharge tube.

Fig. 8 Schematic of capacitor transfer circuit used for laser discharge.

Fig. 9 Time development of the N_2 laser pulse relative to the main discharge pulse.

Fig. 10 Cross section of laser discharge tube.

Fig. 11 Gas flow scheme for N_2 laser.

Fig. 12 Cross section of spark gap used in N_2 laser.

Fig. 13a Schematic of high voltage power supply for N_2 laser.

Fig. 13b Schematic showing BNC outputs from laser circuit.

Fig. 14 Operation of the LC charging circuit.

Fig. 15 Cross-sectional view of plate capacitors.

Fig. 16 Peak power of N_2 laser as a function of the repetition rate.

Fig. 17 Discharge circuit for flashlamp dye laser.

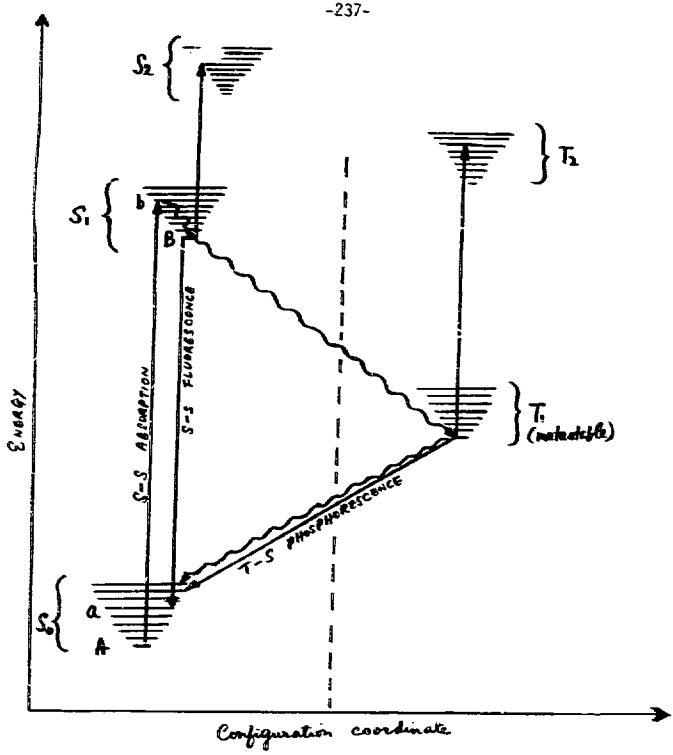

XBL 7710-6778

Fig. 1

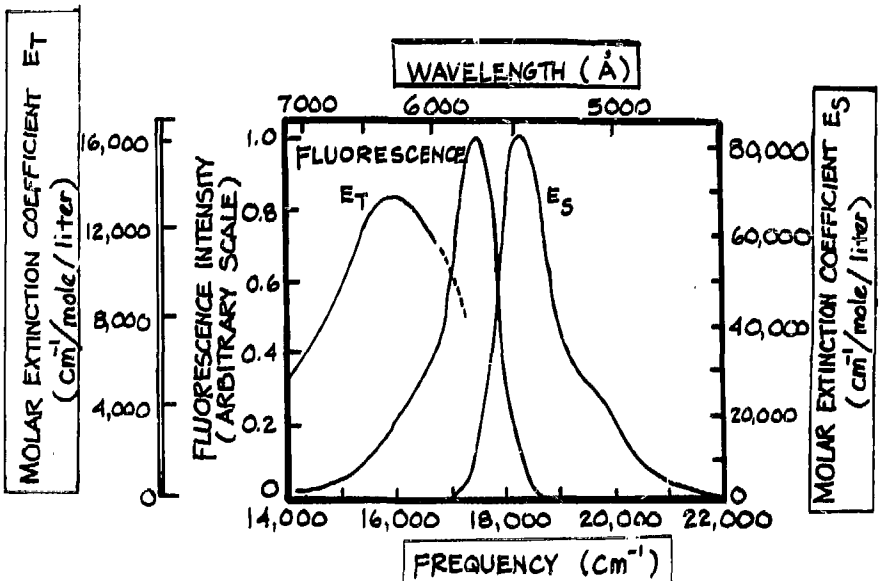

Fig. 2

XBL 7710-6760

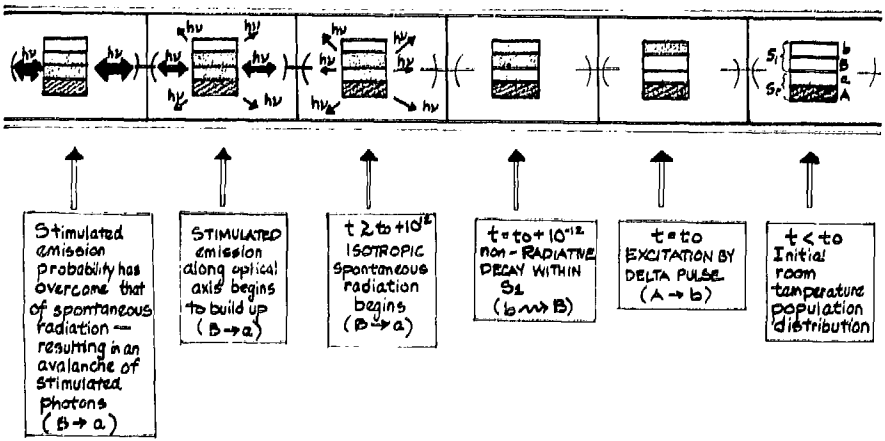

XBL 7710-6764

Fig. 3

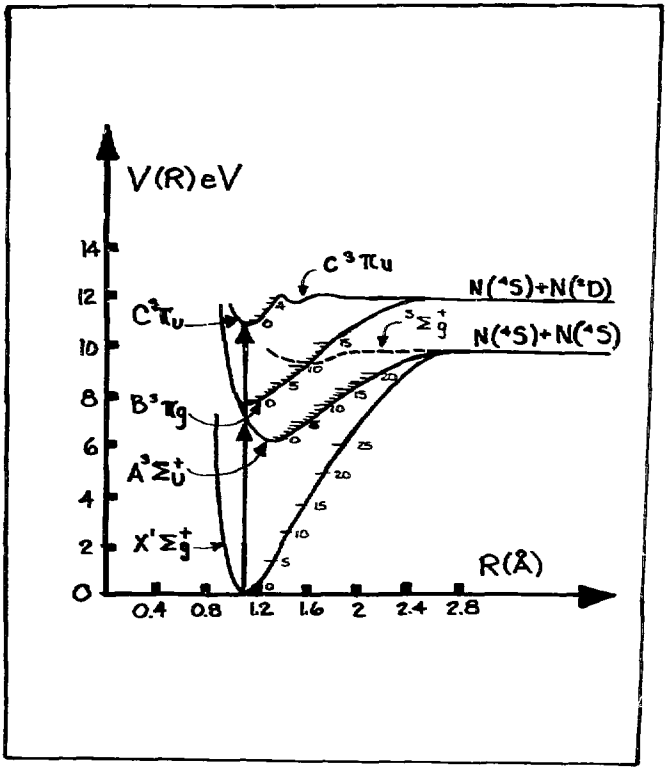

XBL 7710-6756

Fig. 4

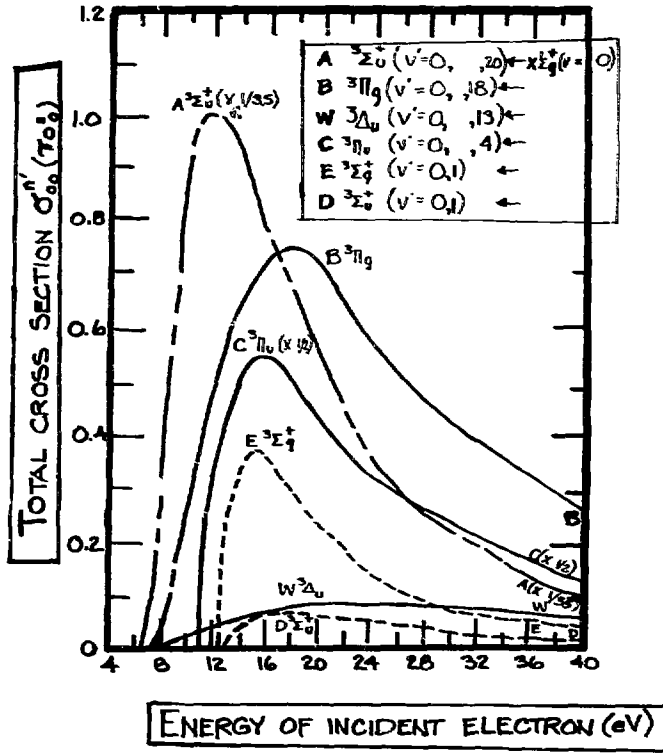

XBL 7710-6766

Fig. 5

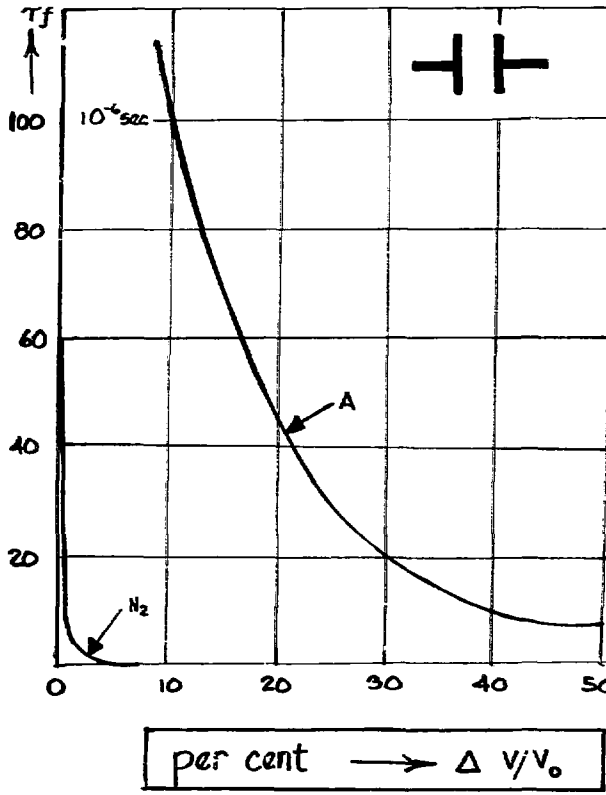

XBL 7710-6765

Fig. 6

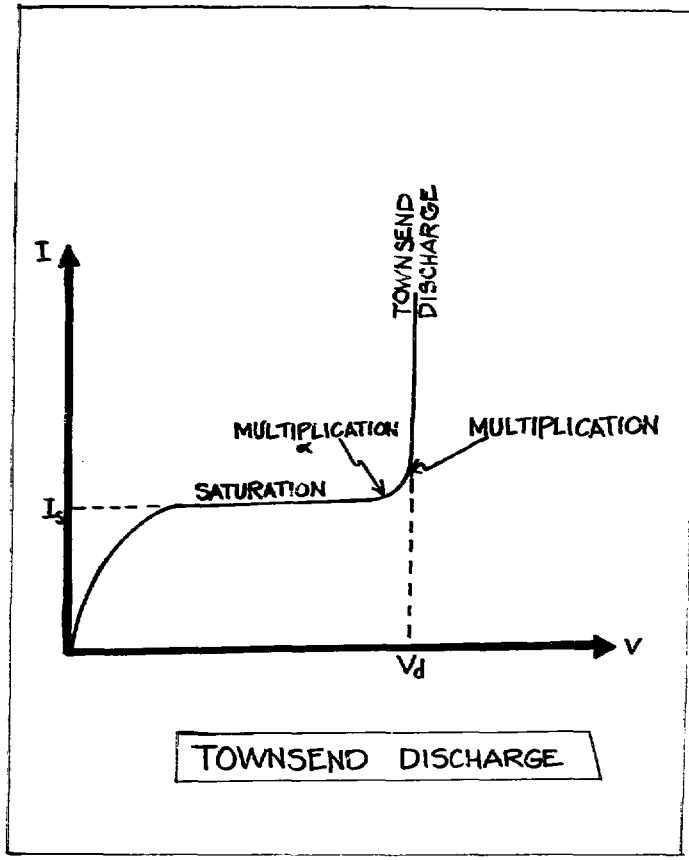

XBL 7710-6763

Fig. 7

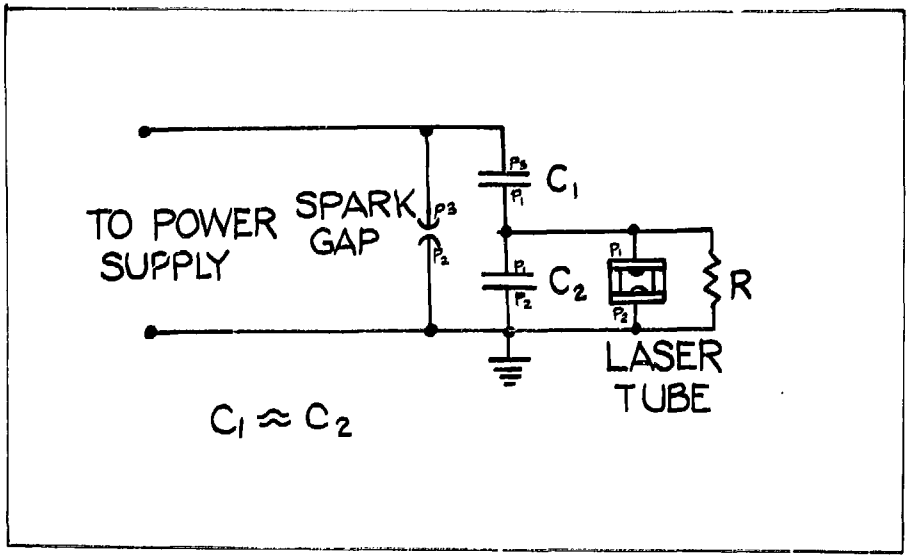

XBL 7710-6767

Fig. 8

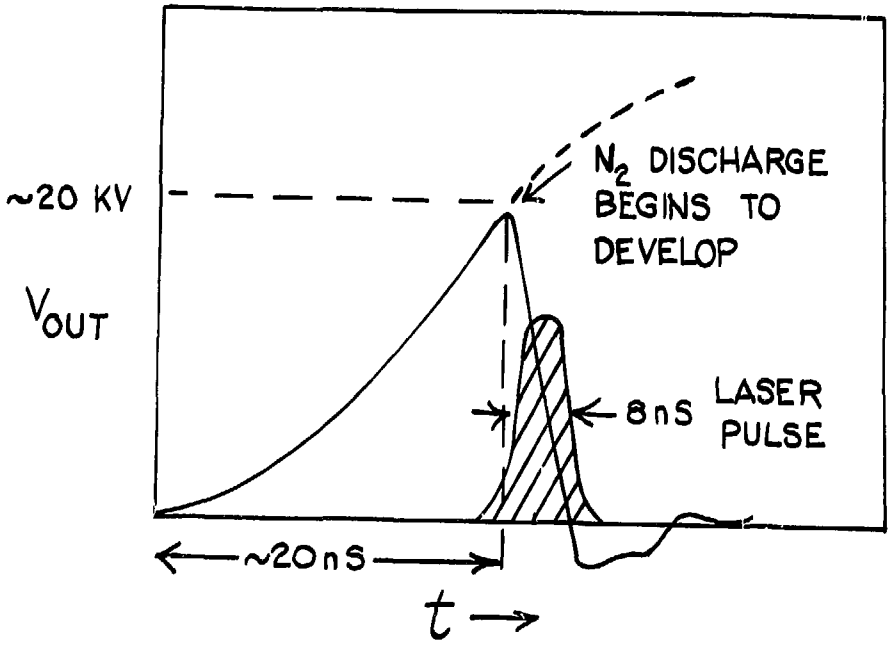

Fig. 9

XBL 7710-6758

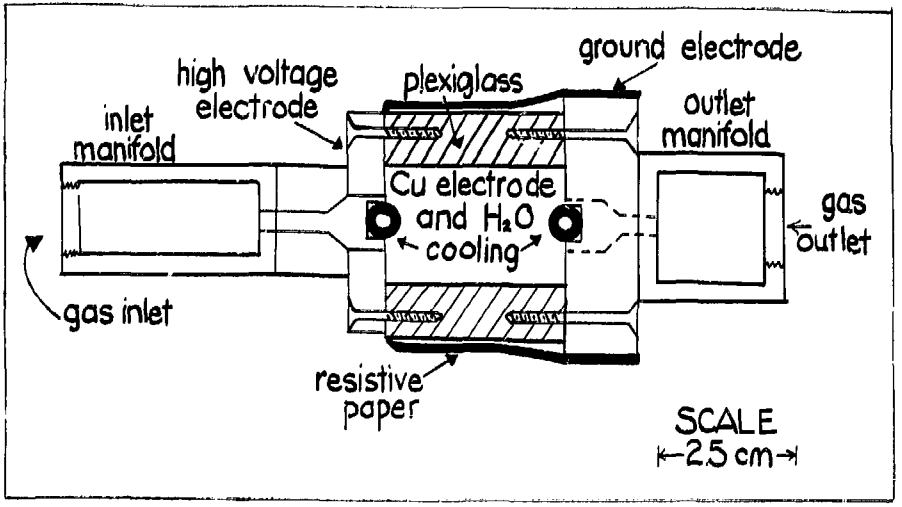

XBL 7710-6769

Fig. 10

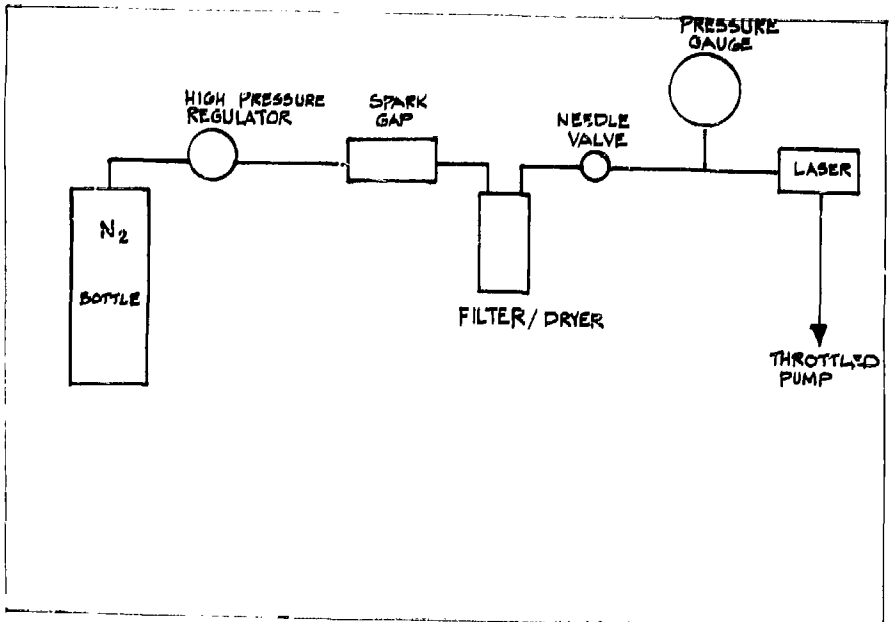

Fig. 11

XBL 7710-6768

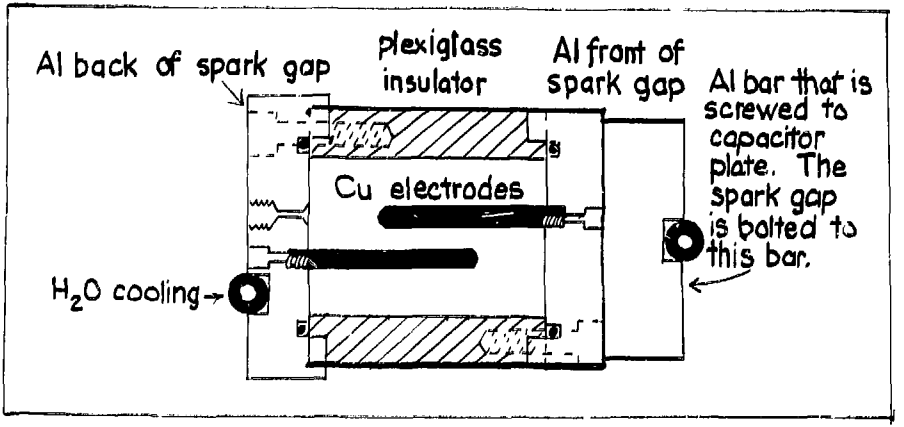

Fig. 12

XBL 7710-6770

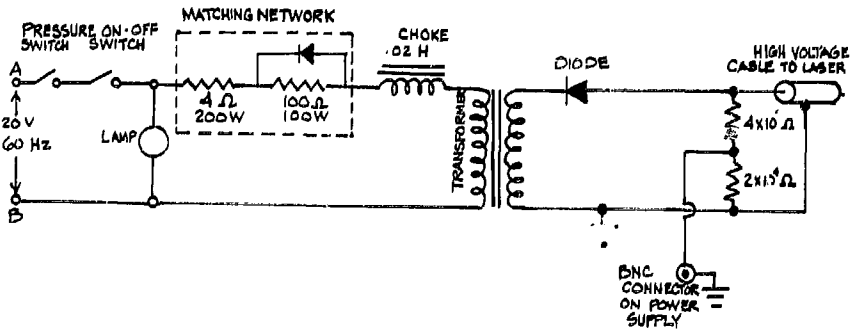

XBL 7710-6762

Fig. 13a

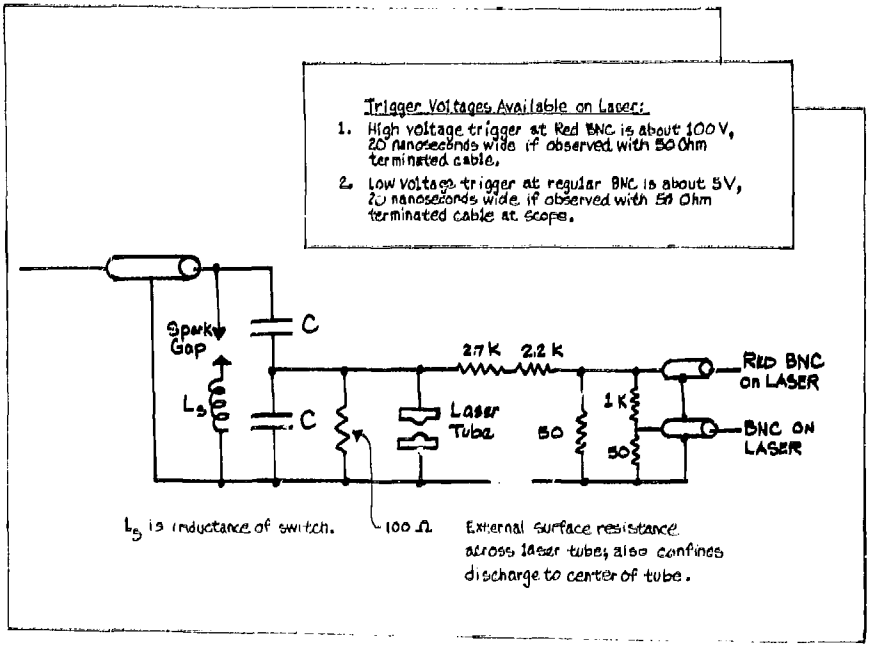

XBL 7710-6757

Fig. 13b

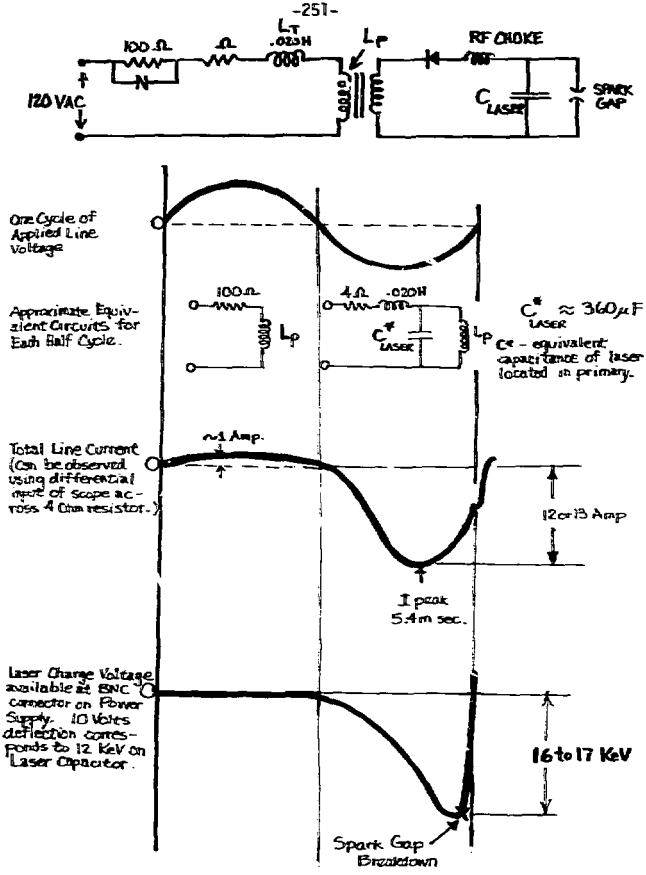

KBL 7710-6761

Fig. 14

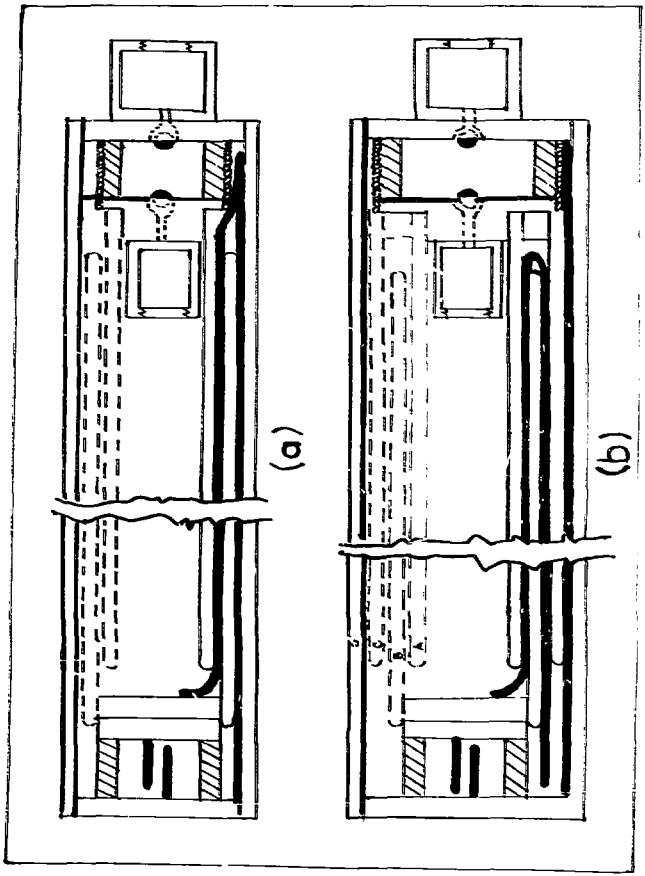

XBL 7710-6754

Fig. 15

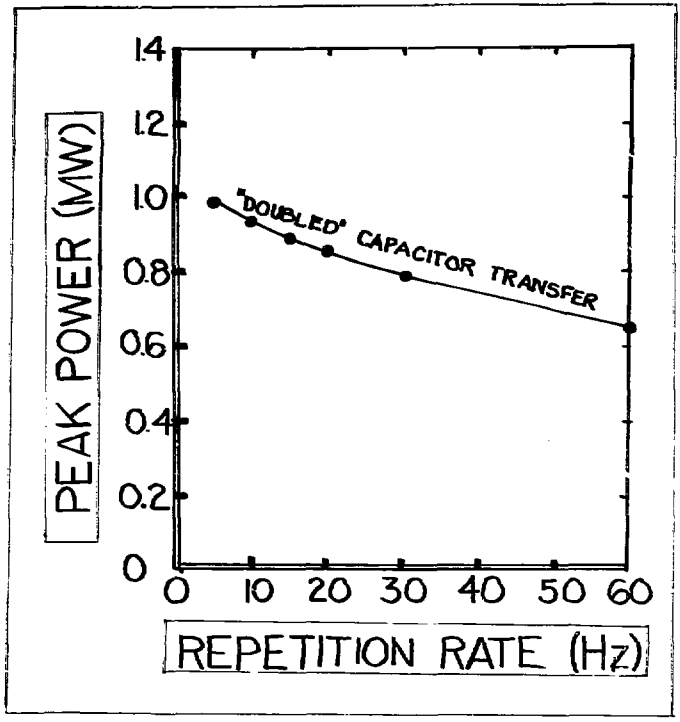
PEAK POWER (MW)
1.4
1.2
1.0
0.8
0.6
0.4
0.2
0
"DOUBLED" CAPACITOR TRANSFER
0
10
20
30
40
50
60
REPETITION RATE (Hz)

Fig. 16

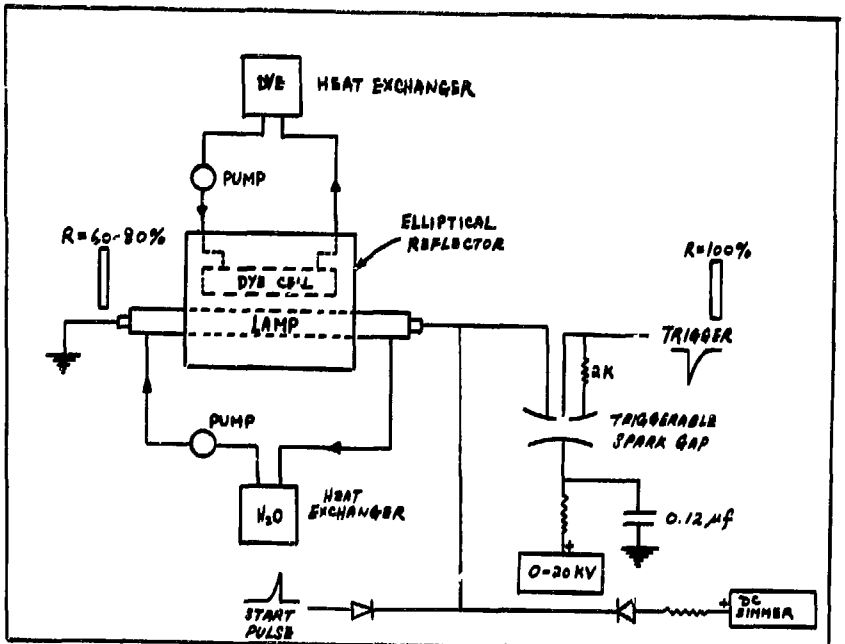

XBL 7710-6776

Fig. 17